The Rough Wall High Reynolds Number Turbulent Boundary Layer Surface Pressure Spectrum

Timothy Wade Meyers

Thesis submitted to the faculty of the Virginia Polytechnic Institute and State University in partial fulfillment of the requirements for the degree of

Master of Science
in
Aerospace Engineering

William J. Devenport

Roger L. Simpson

William N. Alexander

2/6/2014
Blacksburg, Virginia

Keywords: Rough Wall, High Reynolds Number, Turbulent Boundary Layer, Surface Pressure Fluctuations

The Rough Wall High Reynolds Number Turbulent Boundary Layer Surface Pressure Spectrum

Timothy Wade Meyers

ABSTRACT

There have been very few studies investigating the rough wall pressure spectra under fully rough flows, which are relevant to many common engineering applications operating within this regime. This investigation uses the Virginia Tech Stability Wind Tunnel to perform experiments on a series of high Reynolds number zero pressure gradient turbulent boundary layers formed over rough walls in an effort to better understand and characterize the behavior of the rough wall pressure spectrum. The boundary layers were fully rough, and the boundary layer thickness remained sufficiently larger than the height of the roughness elements. Two rough surfaces were tested. One consisted of an array of 1-mm ordered hemispherical elements spaced 5.5-mm apart, and the other contained 3-mm hemispherical elements randomly spaced, but with the same element density as 1/3 of the 1-mm ordered roughness. The wall pressure spectrum and its scaling were then studied in detail, and it was found that the rough wall turbulent pressure spectrum at vehicle relevant conditions is defined by three scaling regions. One of which is a newly discovered high frequency scaling defined by viscosity, but controlled by the friction velocity adjusted to exclude the pressure drag on the roughness elements. Based on these three scaling regions an empirical model describing the wall pressure spectra for hydraulically smooth, traditionally rough, and fully rough flows was explored. Two point wall pressure fluctuations were also analyzed for each surface condition, and it was found that the roughness inhibits the convective velocities within the inner portions of the boundary layer.

Acknowledgements

I would like to thank my family for always being there to support me even through the more stressful times of my education. I could not have done it without them. I would also like to give a special thanks to my advisor Dr. William Devenport. I cannot express how lucky I was to have him as an advisor. He fostered a supportive environment and believed in me when I didn't quite believe in myself. His guidance and knowledge was invaluable, and he showed me how to succeed. I would not have the research capabilities I have today without him.

I would also like to thank my committee members Dr. Roger Simpson and Dr. Nathan Alexander for their guidance and insight on my research. Dr. Alexander played a huge role in making sure that I had everything prepared for my wind tunnel entry as well as helping me out with the data acquisition. I don't think it would have gone as smoothly without his help.

I would like to thank Jonathan Forest for mentoring me as an undergraduate student. He gave me a huge head start by teaching me everything he knew about rough wall surfaces, and showing me how to avoid the same mistakes he made. Without him I would not have been able to come this far in my research. I would also like to thank Mike Morton for teaching me how to set up and operate the quad hotwires, and for staying late and helping me finish collecting data for my wind tunnel entry. I would like to thank Dr. Aurelien Borgotlz for helping me debug equipment in the wind tunnel, and for teaching me how to efficiently document and take data.

I would also like to thank the good people of lab 7, specifically Manuj Awasthi, Liselle Joseph, Ken Brown, and Ian Clark. They provided a fun work environment, and were always ready to lend a helping hand.

I would like to thank Chip Jackson for his help in aligning and installing the rough walls in the wind tunnel test section, and for his detailed measurements of the modified contraction as an undergraduate research assistant.

I would like Bill Oetjens for his help setting up and running the wind tunnel for my experiment. I would also like to thank the AOE machine shop. Specifically I would like to give a big thanks to Cameron Hollandsworth for his help with the fabrication of the rough wall surfaces, Scott Patrick for his help with 3-D printing the microphone mounts, and James Lambert for his help manufacturing the aluminum plates used to mount the roughness fetches.

Finally I would like to thank the National Science Foundation for their financial support under grant CBET-0853674 that allowed this research to be conducted.

Thank you everyone for all of your help and support.
Sincerely,
Tim Meyers

TABLE OF CONTENTS

CHAPTER 1: INTRODUCTION..... 1

1.1 Motivation..... 1
1.2 Literature Review..... 2
1.2.1 Overview of flow types and roughness classification 2
1.2.2 Scope of this Investigation 3
1.2.3 Selected experimental study overview..... 3
1.2.4 Smooth wall flows..... 4
1.2.5 Rough wall flows..... 6
1.3 Objectives..... 9

CHAPTER 2: APPARATUS AND INSTRUMENTATION..... 10

2.1 Virginia Tech Stability Wind Tunnel..... 10
2.2 False Wall..... 11
2.3 Rough Surfaces..... 11
2.4 Boundary Layer instrumentation..... 12
2.5 Surface Pressure Instrumentation..... 14
2.5.1 Mean Wall Pressure..... 14
2.5.2 Surface Pressure Fluctuations..... 15

CHAPTER 3: ANALYSIS AND DISCUSSION..... 18

3.1 Measurement overview..... 18
3.2 Mean wall pressure gradient..... 19
3.3 Boundary layer wall flow..... 19
3.3.1Boundary layer classification overview..... 19
3.3.2 Measurement consistency..... 19
3.3.3 Boundary layer two-dimensionality..... 20
3.3.4 Boundary layer turbulence structure..... 20
3.3.5 Boundary layer parameter determination..... 21
3.3.5.1 Determining friction velocity..... 21
3.3.5.2 Boundary layer parameter results..... 23
3.3.6 Boundary layer scaling parameters..... 24
3.4 Surface pressure fluctuations..... 26
3.4.1 Surface pressure spectrum..... 26
3.4.2 Scaling of the surface pressure spectrum..... 27
3.4.3 A new scaling for the highest frequency pressure fluctuations..... 31
3.4.4 Physical interpretation of the viscous friction velocity..... 33
3.4.5 Triple scaling hypothesis..... 35
3.4.6 Empirical spectral model of the surface pressure fluctuations..... 36
3.5 Two point Pressure Fluctuation Measurements
3.5.1 Coherence..... 39
3.5.2 Correlation..... 41
3.5.3 Phase and Phase Convection Velocity..... 43

CHAPTER 4: CONCLUSIONS..... 45

REFERENCES..... 47

APPENDIX A: ROUGHNESS MANUFACTURING PROCEEDURE..... 108

Nomenclature

Roman

A_p	Projected roughness surface area onto a plane normal to the flow direction
A_s	Wetted surface area of roughness as seen by the flow
c	Speed of sound
C_f	Skin friction coefficient
d	Pinhole diameter
d^+	Dimensionless pinhole diameter ($d^+=du_\tau/\nu$)
d_e	Mean distance between roughness elements
f	Frequency (Hz)
H	Boundary layer shape factor ($H=\delta^*/\theta$)
k	Wavenumber in the streamwise direction, ($k=\omega/U_c$)
k_g	Roughness height
k_g^+	Roughness height Reynolds number ($k_g^+=k_g u_\tau/\nu$)
k_s	Equivalent sand grain roughness height
k_s^+	Equivalent sand grain roughness height Reynolds number ($k_s^+=k_s u_\tau/\nu$)
p	Wall pressure
q	Dynamic pressure ($q = \frac{1}{2}\rho U_e^2$)
R_{pp}	Space-time correlation
s	Separation distance
TKE	Turbulent kinetic energy ($TKE = \frac{1}{2}u'^2 + \frac{1}{2}v'^2 + \frac{1}{2}w'^2$)
T_L	Lagrangian timescale of space-time correlation decay
u	Local mean velocity, x-direction
u'	Local RMS fluctuating velocity, x-direction
u^+	Normalized local mean velocity for the law of the wall, x-direction
U_{cp}	Phase convection velocity
U_c	Convection velocity
u_τ	Friction velocity
U_e	Edge velocity
u_v	Viscous friction velocity
v	Local mean velocity, y-direction
v'	Local RMS fluctuating velocity, y-direction
w	Local mean velocity, z-direction
w'	Local RMS fluctuating velocity, z-direction
x	Streamwise position, measured downstream of primary trip
y	Vertical position, measured down from tunnel centerline
z^+	Normalized distance away from the wall for the law of the wall
z	Horizontal position, measured away from false wall

Greek

α	Phase angle
δ	Boundary layer thickness
δ^*	Boundary layer displacement thickness
η	Spanwise separation
Γ	Coherence
κ	Von Kármán constant ($\kappa = 0.40$)
λ	Sparseness Ratio
ν	Kinematic viscosity
ω	Angular frequency (radians)
Φ	Wall pressure spectral density
ϕ_{pp}	Wall pressure spectrum
ρ	Density
τ	Time delay
τ_w	Wall shear
θ	Boundary layer momentum thickness
ξ	Streamwise separation

List of Tables

Table 1: Quad-hotwire average absolute uncertainties……..……. 14
Table 2: Locations of mean wall pressure measurements……..... 15
Table 3: Microphone locations used in surface pressure measurements…… 16
Table 4: Surface pressure spectrum uncertainty by frequency ……..... 17
Table 5: Summary of measurements made for each surface condition……..... 18
Table 6: The zero wall pressure gradient flow final boundary layer parameters using the double 19-mm trip; Forest's (2012) data is given and italicized for comparison…….. 24
Table 7: Boundary layer parameters from current and previous studies used in the surface pressure spectra scaling……..... 25
Table 8: List of viscous friction velocities used to scale data from Blake (1970), Aupperle and Lambert (1970), Varano (2010), Forest (2012) and the present study……..……..... 33

List of Figures

Figure 1: Classical outer scaling applied to smooth wall data from Blake (1970), Farabee and Casserella (1991), and Forest (2012)…….. 50
Figure 2: Mixed outer scaling applied to smooth wall data from Blake (1970), Farabee and Casserella (1991), and Forest (2012)……..... 50
Figure 3: Viscous scaling applied to smooth wall data from Blake (1970), and Forest (2012)……... 51
Figure 4: The Virginia Tech Stability Wind Tunnel (figure courtesy of AOE Department) shown with the full anechoic configuration, and its modification to the hemi-anechoic test section used for this investigation. (Modified figure used with permission of Dr. William J. Devenport and Jonathan B. Forest)…….. 52
Figure 5: Framed Lexan panel and mounting system…… 53
Figure 6: Modified contraction, primary trips and testing surface…… 54
Figure 7: General test section configuration and coordinate system where the *x*, *y*, and *z* coordinates correspond to the streamwise, spanwise, and wall normal coordinate. The origin of which is located at the primary trip at the centerline and flush with the testing surface. (Modified figure used with permission of Jonathan B. Forest)…… 55
Figure 8: Forward and primary 19 mm angled aluminum trips…… 55
Figure 9: Ordered distribution of 1-mm hemispherical roughness (a) and random distribution of 3-mm hemispherical roughness (b)……..….. 56
Figure 10: 3-mm random roughness distribution shown with microphone locations…… 57
Figure 11: (a) quad-hotwire positioning with respect to 1-mm ordered roughness elements, and (b) quad-hotwire positioning with respect to 3-mm random roughness elements…….. 58
Figure 12: Traverse system used to position the hotwire probes……... 59
Figure 13: Traverse probe mount configuration…… 60
Figure 14: Example lens calibration photo…… 61
Figure 15: Undistorted measured yaw angles of the 1-mm ordered (a) and 3-mm random (b) rough surfaces…… 62
Figure 16: Example of ½ mm pressure tap locations……..……... 63

Figure 17: B&K 4138-A-015 1/8th inch microphones fitted with ½ mm pinhole cap (a) and standard microphone cap (b)…… 64
Figure 18: Microphone calibration setup…… 64
Figure 19: Optimized calibrations (black) plotted with raw calibration (green) for amplitude (a) and phase (b)…….. 65
Figure 20: Microphone holders (a) and an example of the position of the holders with respect to the1-mm ordered (b) and 3-mm random (c) roughness elements… 66
Figure 21: Microphone measurement locations with respect to the Lexan Panel…….. 67
Figure 22: Mean streamwise pressure coefficient distribution as a function of surface type. Data from Forest (2012) included for comparison. ……. 68
Figure 23: Boundary layer thickness determination from the quad hotwire for the 1-mm ordered roughness at 30 m/s…….. 68
Figure 24: Boundary layer profile comparison of single and quad hot-wire results for (a) the 1-mm roughness and (b) the 3-mm random roughness ……. 69
Figure 25: Comparison of single hotwire (SHW) and quad hotwire (QHW) u'^2/U_{ref}^2 profiles for the 1-mm ordered (a) and 3-mm random (b) rough surface conditions……... 70
Figure 26: Boundary layer non-dimensionalized smooth surface profiles at 6.98 m for the present study's data at varying heights along the wall compared to data from Forest (2012)……... 71
Figure 27: Rough surface turbulence intensity profiles where $\sqrt{\overline{v'^2}}/U_\tau$ is offset by +0.5 and $\sqrt{\overline{u'^2}}/U_\tau$ is offset by +1 as shown in figure. Data form Blake (1970) and Forest (2012) is also included…… 71
Figure 28: Turbulent kinetic energy profiles (TKE) plotted as z/δ *vs.* TKE/u_τ^2. Data from Forest (2012) included for comparison……..... 72
Figure 29: Momentum thickness estimation for the 1-mm ordered roughness at 30 m/s…….. 72
Figure 30: Inner scaling of rough surface Reynolds shear stress used to obtain u_τ…… 73
Figure 31: Experimental data compared to the theoretical results obtained from Equation 3.6 for the 1-mm ordered roughness at 30 m/s…… 73
Figure 32: Mean velocity profiles plotted in terms of inner variables……74
Figure 33: Boundary layer roughness effects comparison for 30 m/s (a) and 60 m/s (b)…….. 75
Figure 34: Homogeneity of the smooth wall pressure fluctuations at each test speed for the streamwise a) and spanwise b) locations……... 76
Figure 35: The smooth wall pressure spectra at each test speed compared to Forest's (2012) smooth wall pressure spectra at slightly different test speeds for the streamwise a) and spanwise b) locations…… 76
Figure 36: 1-mm roughness auto spectra at each speed for the (*a*) streamwise and (*b*) spanwise microphone rows…….. 77
Figure 37: Random 3-mm roughness auto spectra at each speed for the (*a*) streamwise and (*b*) spanwise microphone rows……77
Figure 38: Comparison surface pressure spectra for the 3-mm random roughness with Forest's (2012) results for the 3-mm ordered roughness…….. 78
Figure 39: Effects of the surface condition on the pressure spectrum for two test speeds……. 78
Figure 40: Legend for rough wall studies analyzed in Figures 41 through 53 where A&L refers to Aupperle and Lambert (1970)…… 79

Figure 41: Classical outer scaling applied to (a) smooth and rough wall data from Forest (2012), and the present study, and (b) the data of Blake (1970), Forest (2010), Varano (2010) and the present study…… 80
Figure 42: Outer scaling based on U_e, δ, and τ_w applied to (a) smooth and rough wall data from Forest (2012), and the present study, and (b) the data of Blake (1970), Forest (2010), Varano (2010) and the present study……. 80
Figure 43: Mixed outer scaling applied to (a) smooth and Rough Wall data from Forest (2012), and the present study, and (b) the data of Blake (1970), Forest (2010), Varano (2010) and the present study…… 81
Figure 44: Outer scaling based on U_e, δ, and q_e applied to (a) smooth and rough wall data from Forest (2012), and the present study, and (b) the data of Blake (1970), Forest (2010), Varano (2010) and the present study…….. 81
Figure 45: Blake's roughness scaling applied to data from (a) Forest (2012), and the present study, and (b) Blake (1970), Aupperle and Lambert (1970), Varano (2010), Forest (2012), and the present study…… 82
Figure 46: Blake's modified roughness scaling on k_s applied to data from (a) Forest (2012) and the present study, and (b) Blake (1970), Aupperle and Lambert (1970), Varano (2010), Forest (2012), and the present study…… 82
Figure 47: Aupperle and Lambert's (1970) scaling applied to data from (a) Forest(2012), and the present study, and (b) Blake (1970), Varano (2010), Forest (2012), and the present study…… 83
Figure 48: Varano's roughness scaling applied to data from (a) Forest(2012), and the present study, and (b) Blake (1970), Varano (2010), Forest (2012), and the present study……..... 83
Figure 49: Forest's (2012) roughness scaling on k_g for data from (a) Forest (2012), and the present study, and (b) Blake (1970), Aupperle and Lambert (1970), Forest (2012), Varano (2010) and the present study……. 84
Figure 50: Forest's (2012) modified roughness scaling on *ks* for data from (a) Forest (2012), and the present study, and (b) Blake (1970), Aupperle and Lambert (1970), Varano (2010) Forest (2012), and the present study……. 84
Figure 51: Rough wall pressure spectra scaled on smooth wall inner variables for (a) Forest (2012) and the present study's data, and (b) Blake (1970), Aupperle and Lambert (1970), Forest (2012), and the present study……... 85
Figure 52: The unified high frequency viscous scaling applied to data from (a) Forest (2012) and the present study, (b) Varano (2010), and (c) Blake (1970) and Aupperle and Lambert (1971). …….. 86
Figure 53: The unified high frequency viscous scaling applied to data from Blake (1970) and Aupperle and Lambert (1970), Varano (2010), Forest (2012) and the present study…… 87
Figure 54: Ratio of friction velocities determined from pressure spectra from the present flows (λ=0.052) compared with Aupperle and Lambert's (1971), λ=0.0467, and Blake (1970) and Varano's (2010) varying sparseness ratios…… 88
Figure 55: Ratio of friction velocities estimated using Equation 14 compared to the ratio of friction velocities determined from the pressure spectra for the present study and that of Forest's (2012)…….. 88

Figure 56: Spectral predictions using Equation 13 of Forest's (2012) smooth wall (a), the 1-mm ordered (b), Forest's (2012) 3-mm ordered (c) and the 3-mm random (d) rough surface conditions for each test speed overlaid on a darkened figure of the spectral measurements…… 89
Figure 57: Spectral predictions using Equation 17 of Blakes's (1971) rough wall pressure spectra for the D-L, S-S, and D-S surface conditions at 38 and 50 m/s overlaid on a darkened figure of the spectral measurements……..... 90
Figure 58: Spectral predictions using Equation 17 of Varano's (2010) rough wall pressure spectra for Fetch 1 (a), Fetch 2 (b), Fetch 3 (c), and Fetch 4 (d) at 20.5 and 27.5 m/s overlaid on a darkened figure of the spectral measurements…….. 91
Figure 59: Mapped streamwise coherence for Forest's (2012) smooth wall (a) at 33.6 m/s, the ordered 1-mm roughness (b), the random 3-mm roughness (c), and Forest's (2012) ordered 3-mm roughness (d) at 30 m/s…… 92
Figure 60: Mapped streamwise coherence for Forest's (2012) smooth wall (a) at 67.2 m/s, the ordered 1-mm roughness (b), the random 3-mm roughness (c), and Forest's (2012) ordered 3-mm roughness (d) at 60 m/s…… 93
Figure 61: Mapped spanwise coherence for Forest's (2012) smooth wall (a) at 33.6 m/s, the ordered 1-mm roughness (b), the random 3-mm roughness (c), and Forest's (2012) ordered 3-mm roughness (d) at 30 m/s…… 94
Figure 62: Mapped spanwise coherence for Forest's (2012) smooth wall (a) at 67.2 m/s, the ordered 1-mm roughness (b), the random 3-mm roughness (c), and Forest's (2012) ordered 3-mm roughness (d) at 60 m/s…… 95
Figure 63: Mapped streamwise correlation for Forest's (2012) smooth wall (a) at 33.6 m/s, the ordered 1-mm roughness (b), the random 3-mm roughness (c), and Forest's (2012) ordered 3-mm roughness (d) at 30 m/s…… 96
Figure 64: Mapped streamwise correlation for Forest's (2012) smooth wall (a) at 67.2 m/s, the ordered 1-mm roughness (b), the random 3-mm roughness (c), and Forest's (2012) ordered 3-mm roughness (d) at 60 m/s…… 97
Figure 65: Mapped spanwise coherence for Forest's (2012) smooth wall (a) at 33.6 m/s, the ordered 1-mm roughness (b), the random 3-mm roughness (c), and Forest's (2012) ordered 3-mm roughness (d) at 30 m/s…… 98
Figure 66: Mapped spanwise coherence for Forest's (2012) smooth wall (a) at 67.2 m/s, the ordered 1-mm roughness (b), the random 3-mm roughness (c), and Forest's (2012) ordered 3-mm roughness (d) at 60 m/s…… 99
Figure 67: Rough wall pressure fluctuation streamwise correlation decay for the ordered 1-mm rough surface condition at 30 and 60 m/s...…….. 100
Figure 68: Rough wall pressure fluctuation streamwise correlation decay for the random 3-mm rough surface condition at 30 and 60 m/s……. 100
Figure 69: Forest's (2012) smooth wall surface pressure fluctuation streamwise correlation decay at 22.4, 33.6, 44.8, 56.0, 67.2 m/s for various separations.. 101
Figure 70: Forest's (2012) 3-mm ordered rough roughness wall pressure fluctuation streamwise correlation decay envelope at each test speed for the various separations a) and a comparison of the correlation decay envelopes for each surface condition b)……. 101

Figure 71: Streamwise phase angle for Forest's (2012) smooth wall (a) at 33.6 m/s, the ordered 1-mm roughness (b), the random 3-mm roughness (c), and Forest's (2012) ordered 3-mm roughness (d) at 30 m/s…….. 102
Figure 72: Streamwise phase angle for Forest's (2012) smooth wall (a) at 67.2 m/s, the ordered 1-mm roughness (b), the random 3-mm roughness (c), and Forest's (2012) ordered 3-mm roughness (d) at 60 m/s…….. 103
Figure 73: Spanwise phase angle for Forest's (2012) smooth wall (a) at 33.6 m/s, the ordered 1-mm roughness (b), the random 3-mm roughness (c), and Forest's (2012) ordered 3-mm roughness (d) at 30 m/s…….. 104
Figure 74: Spanwise phase angle for Forest's (2012) smooth wall (a) at 67.2 m/s, the ordered 1-mm roughness (b), the random 3-mm roughness (c), and Forest's (2012) ordered 3-mm roughness (d) at 60 m/s…….. 105
Figure 75: Phase convection velocities for Forest's (2012) smooth wall (a) at 33.6 m/s, the ordered 1-mm roughness (b), the random 3-mm roughness (c), and Forest's (2012) ordered 3-mm roughness (d) at 30 m/s……... 106
Figure 76: Phase convection velocities for Forest's (2012) smooth wall (a) at 67.2 m/s, the ordered 1-mm roughness (b), the random 3-mm roughness (c), and Forest's (2012) ordered 3-mm roughness (d) at 60 m/s…….. 107
Figure A1: An example of a HDPE mold containing the negative of a 2x1 ft. 1-mm ordered hemispherical roughness fetch, where the elements are spaced 5.5 mm apart…… 108
Figure A2: Sizing of fiberglass weave (a) and sketch paper (b)…… 109
Figure A3: Applying the Mann Ease Release 200 to the HDPE mold……. 109
Figure A4: 3:1 ratio of epoxy resin to epoxy hardener……. 110
Figure A5: Pouring mixture (a) and spreading it over the mold (b)…….. 110
Figure A6: Placing the sketch paper over the mold……... 111
Figure A7: Placing the fiberglass weave over the mold…… 112
Figure A8: Placing nylon over the fiber glass (a) and cotton (paper towels shown here) (b) over the nylon…… 112
Figure A9: Heavy metal plate placed over the mold layers…….. 113

CHAPTER 1. INTRODUCTION

1.1.Motivation

Despite its importance, remarkably little is known about the wall pressure fluctuations generated by rough surface conditions under high Reynolds number turbulent flows that are scalable to many common engineering applications. These applications include ships, aircraft, wind turbines, and buildings. Now ideally these surfaces would be hydraulically smooth and the problem would already be fairly well understood from previous studies (Bradshaw, 1967, Bull, 1967, Farabee & Casarella, 1991, Horne, 1990, and Morrison, 2007, for example). However, surface roughness is almost always encountered on these large scale engineering applications, and is the result of both environmental (ship fouling or aircraft icing) and manufacturing (surface imperfections or rivets) processes usually unique to each surface. The addition of surface roughness to a hydraulically smooth wall flow alters the characteristics of that flow in a largely unknown way. However by measuring the surface pressure fluctuations we can start to gain insight into the physical structure of the rough wall turbulent boundary layer.

Once we understand the physical structures and the mechanisms responsible for them, we can begin to address issues such as vibrational, aerodynamic and hydrodynamic noise. Surface pressure fluctuations can induce panel vibration when the boundary layer progresses over a relatively thin flexible structure, such as a ship hull or aircraft fuselage, and ultimately leads to additional noise within the structure (Maury *et al.* 2002). As the boundary layer leaves the trailing edge of a lifting surface e.g. wings, turbine blades or propellers, the surface pressure fluctuations are scattered into sound and have found to be the dominant source of wind turbine noise (Moriarty *et al.* 2005, Oerlemans *et al.* 2007). Liu and Dowling (2007) have also shown that surface roughness can not only increase trailing edge noise, but the 'scrubbing' noise generated solely from the roughness elements can, at high frequencies, exceed the trailing edge noise. Glegg and Devenport (2009) and Alexander *et al.* (2012) were able to rigorously show, starting from Lighthill's analogy, that this far-field noise spectrum is a predictable function of the surface geometry and the wall pressure spectrum. Therefore, modeling and predicting surface pressure fluctuations becomes invaluable when concerned with far-field acoustics.

However, very few studies exist exploring the wall pressure spectrum of rough wall high Reynolds number turbulent flows free of transition effects as outlined by Jimenez (2004), where similarity laws can be observed. Therefore, the focus of the present study is to extend the previous experimental work and attain a comprehensive model that captures the effect of the roughness on the boundary layer, which will ultimately allow for direct estimates of the boundary layer properties via CFD and far-field noise predictions of known surface geometries without direct experimental measurements.

1.2.Literature Review

1.2.1 Overview of Flow Types and Roughness Classification

No wall bounded flow is ever completely free of roughness and thus the extent of which the roughness has an effect on the given flow must first be classified. Through his work, Nikuradse (1933) uncovered three types of rough flow regimes: hydraulically smooth (effectively no roughness), transitionally rough, and fully rough. Jimenez (2004) reviewed these regimes and their classifications based off of the effective sand grain roughness Reynolds number k_s^+. The sand grain roughness k_s, is commonly viewed as a general aerodynamic measurement, which describes how any addition of roughness shifts the inner scaled mean velocity away from the law of the wall for hydraulically smooth wall surfaces. This parameter is a function of the roughness height and spacing, and can be scaled on the friction velocity u_τ, and kinematic viscosity ν, which yields the effective sand grain roughness Reynolds number $k_s^+=k_s\ u_\tau/\nu$, providing a good indication of the interference a particular flow is subjected to by the roughness elements.

In the hydraulically smooth regime, $k_s^+ < 5$, the viscous drag is dominant, since any roughness is sufficiently small compared to the sub-layer height. As the size of the roughness element is increased, the element's height enters the same order of magnitude as the sub-layer height, and the viscous and form drag both contribute to the total surface drag. This regime is known as transitionally rough, and it is generally accepted that it has a k_s^+ value between 5 and 70. Finally for the fully rough regime $k_s^+ > 70$, the form drag on the roughness elements becomes dominant when the roughness elements are sufficiently large compared to the sub-layer height.

Jimenez's review went on to further identify one other rough flow regime based solely on height, where the roughness extended well into the boundary layer and essentially modified the flow so that it started to behave much like the flow around surface mounted obstacles. For this regime, the roughness significantly effects large portions of the boundary layer's logarithmic region, and is usually defined by a blockage ratio, δ/k_g of less than 40. Therefore if all else essentially remains constant for a sufficiently high Reynolds number flow, as the presence of the roughness elements is increased, the flow progresses from hydraulically smooth to transitionally rough to the fully rough regime, which will eventually lead to a flow around surface mounted obstacles.

Within these regimes though, there exist several different classifications of roughness elements. One classification specifies the roughness elements as 2-D or 3-D, which are commonly found on engineering structures. 2-D roughness elements are usually associated with riblets or grooves, whereas 3-D roughness contains standalone elements such as the idealized hemispheres, cubes or cones. According to Brandyopadhyay and Watson (1988), the main distinction between the two is the direction of the near-wall transport of shear stress, which is normal to the wall for flow over 2-D roughness elements. This investigation, however, will focus solely on describing the characteristics of 3-D roughness elements.

Perry *et al.* (1969) further classified 3-D roughness into two different types: k-type and d-type. D-type roughness has a roughness defect proportional to the largest length scale in the flow such as the diameter d, for fully developed pipe flows or the boundary layer thickness, δ. K-type roughness on the other hand, has a roughness deficit proportional to the roughness height, k. It is generally accepted that these roughness types are defined by a range of sparseness ratios λ, which is a measure of the spacing between roughness elements and is determined by taking the relation of the element frontal area to the plan form area of a surface. The sparseness ratios of $\lambda \leq 1/7$ will define sparsely spaced roughness and the sparseness ratios of $\lambda > 1/7$ will be considered densely spaced roughness. As the sparseness ratio increases the drag on the surface

increases as well, reaching a maximum around $\lambda=1/7$. Any increase in the sparseness ratio beyond this point leads to roughness elements shielding one another in the flow and thus the drag coefficient is reduced.

1.2.2 Scope of this Investigation

The various types of roughness defined above yield fundamentally different phenomena within the boundary layer. Therefore, this study will limit its investigation to an important niche of significant interest within the flow regimes and surface types. Specifically, this study will focus on a two dimensional, zero pressure gradient flow for 3-D, k-type roughness within the fully rough regime of $k_s^+ > 80$, and with a sufficiently large blockage ratio of $\delta/k_g > 50$ as suggested by Jimenez to obtain a flow free of transitional effects. This specific type of flow allows for the problem to be simplified enough for the fundamental physics to be understood, while still being applicable to the common large scale engineering structures as described in the motivation section, which contain 3-D, k-type roughness. The fairly well-understood hydraulically smooth wall condition for a high Reynolds number turbulent flow will also be considered in the analysis with the hopes of determining a more universal perception of the high Reynolds number turbulent boundary layer structure and surface pressure fluctuation behavior over a wide range of surface conditions. More specifically this study will try and analyze the evolution of the characteristics of the turbulent boundary layer of a specific flow as the surface roughness presence is increased by varying the size, spacing and shape.

A comprehensive literature review searching for the proposed criteria above was completed. As mentioned previously, there have been many studies that have examined the surface pressure fluctuations for smooth wall flows under a zero pressure gradient: Bradshaw (1967), Bull (1967), Blake (1970), Panton and Linebarger (1974), Farabee and Caserella (1991), Horne (1990), Morrison (2007), and Forest (2012) to name a few. However far less exist for the flow and rough surface conditions outlined above such as: Aupperle and Lambert (1970), Blake (1971), Jimenez (2004), Smith (2008), Alexander (2009), Varano (2010), and Forest (2012). Well defined experimental studies with sufficient information from their investigations were selected for both the smooth and rough wall surface conditions, which allowed for data manipulations and direct comparisons of the surface pressure fluctuations to the data collected and analyzed in this study. Although most of the selected rough wall studies did not achieve Reynolds numbers high enough to formally be considered within the fully rough regime, they still provided valuable data, as each study was chosen for their primary focus of one or more aspects of the defined scope of this investigation. From the studies reviewed, the following smooth wall studies: Blake (1970), Farabee and Caserella (1991), and Forest (2012), and the following rough wall studies: Aupperle and Lambert (1970), Blake (1971), Varano (2010), and Forest (2012) were selected for data comparison.

1.2.3 Selected Experimental Study Overview

Farabee and Casarella's (1991) study was a hydraulically smooth wall investigation, which analyzed the surface pressure auto and cross spectrum. Data was taken at The Catholic University of America's wind tunnel at speeds of 15.5, 21.3, and 28.3 m/s. From their investigation they were able to firmly establish the spectral features of the wall pressure fluctuation, and their findings will be explored further in the following section.

Blake's (1970) study was an important investigation encompassing both hydraulically smooth and rough wall flows. Blake's (1970) rough wall investigation was chosen because it

focused on the effects of varying both roughness separation as well as height on the wall pressure spectrum. Although he did so at a scale not predicted by Jimenez to be completely free of transitional effects. Blake (1970) tested three types of rough surfaces, which he designated as densely packed large (D-L), sparsely packed small (S-S), and densely packed small (D-S) at flow speeds of 38 and 50 m/s in the subsonic low turbulence acoustic wind tunnel in the Acoustics Vibration Laboratory at the Massachusetts Institute of Technology. These rough surfaces had corresponding equivalent sand grain roughness Reynolds numbers between k_s^+=172 and k_s^+=412, and blockage ratios between δ/k_g = 26 and δ/k_g = 42.

Aupperle and Lambert's (1970) study was another of the first comprehensive experimental studies of the surface pressure spectrum for rough wall flows. One of their primary interests and the reason the study was chosen was because it focused on investigating the effects of varying the roughness size on the surface pressure spectrum. The study explored commercial grade 36, 12, and 4, grit roughness elements. Each fetch was tested at 50 m/s in the Propagation Research Laboratory's continuous-flow subsonic wind tunnel at the University of Minnesota, and consisted of sparsely populated, uniformly distributed sand particles. This translated to equivalent sand grain roughness Reynolds numbers between k_g^+= 80 and k_g^+= 858, and blockage ratios between δ/k_g = 56 and δ/k_g = 10. Thus only one of the roughness configurations met the conditions set forth by Jimenez. For the case with the greatest surface roughness, the location of the pressure transducer was also varied in order to determine and explore any local effects created by the roughness elements on the surface pressure spectrum.

Varano's (2010) study was selected since it focused on accurately determining the boundary layer parameters for rough wall flows, while also examining the rough wall fluctuating pressure field. Varano (2010) used the Virginia Tech Small Boundary Layer Wind Tunnel to test the effects of various element separations of an ordered 1-mm radius hemisphere square array at 20 and 27 m/s. The hemispheres were spaced at a distance of 4, 5.5, 8, and 11 mm apart.

Finally, Forest's (2012) study was the first comprehensive study meeting the full criteria of this investigation. Forest (2012) investigated the smooth wall, as described previously and rough wall surface pressure spectra. For the rough wall surface pressure spectra, Forest (2012) studied a 3-mm hemispherical square array spaced 16.5 mm apart. The investigation was conducted in Virginia Tech's Stability Wind Tunnel and rough wall data was taken at 20, 30, 40, 50 and 60 m/s. This yielded equivalent sand grain roughness Reynolds numbers ranging from k_g^+= 200 to k_g^+= 507, and blockage ratios between δ/k_g = 72 to δ/k_g = 76. This is well within Jimenez criteria for a fully rough flow. Note that Forest's study and the current investigation were conducted under the same grant and are therefore closely related. This investigation expanded upon Forest's findings in order to gain a better understanding of rough wall flows by testing a pseudo-random distribution and a 1/3 scaled version of Forest's 3-mm ordered rough surface, which will be discussed further in Section 2.

1.2.4 Smooth Wall Flows

The previous findings pertaining to hydraulically smooth and fully rough turbulent boundary layers will now be reviewed and applied to the selected aforementioned studies. Fortunately understanding of the hydraulically smooth wall flow $k_s^+ < 5$, is fairly well-established, and so this study will begin here. Bull's (1967) study was particularly useful in that he reviews and summarizes most of the general findings pertaining to the zero pressure gradient smooth-wall fluctuating pressure fields. From Bull's review, several studies have shown that the pressure fluctuations are influenced by the integrated velocity field over the entire range of the smooth

wall boundary layer. These studies then go on to suggest that the wall pressure spectra can be divided into four distinct sections: high, mid, low and very low frequencies. Each of these sections has been found to correlate well with a specific region of the turbulent boundary layer and can be modeled via scaling laws based on parameters unique to the flow conditions. These parameters are intended to collapse the surface pressure spectra, and when a complete collapse between them is achieved, it is implied that these parameters are the mechanisms responsible for determining that portion of the surface pressure spectra.

Farabee and Casarella's (1991) study was able to identify and establish the scaling laws for low to mid and high frequency regions of the smooth wall pressure spectrum, revealing the existence of two distinct wave number groups at both high and low frequencies. It was shown that the high frequencies of the wall pressure spectrum were largely associated with the turbulent eddies located within the inner most portions of the turbulent boundary layer, whereas the mid-frequencies were linked to the logarithmic region. The low and very low frequencies were then found to be caused by the large turbulent structures produced in the outer portions of the turbulent boundary layer.

As a result from findings like these, two types of smooth wall scaling currently exist, the inner and outer scaling, and in conjunction effectively collapse the surface pressure fluctuations over the entire measured spectrum. The smooth wall outer scaling exists in two forms, the classical outer scaling and the mixed outer scaling. Goody's (1999) study showed that the classical outer scaling takes the spectral density $\Phi(\omega)$ and frequency ω or f and normalizes it on the wall shear stress τ_w, boundary layer thickness δ and edge velocity U_e as $\Phi(\omega)u_\tau/(\tau_w^2\delta)\ vs.\ \omega\delta/u_\tau$ collapsing the low frequency end of pressure spectra. As an example, Forest (2012) depicted this collapse on classical outer scaling variables for low frequencies using data from Blake (1970), Farabee and Caserella (1991), and Forest (2012). He was able to show that the smooth wall pressure spectrum successfully collapses to a single curve for low frequencies across studies within the measurement uncertainty as seen in Figure 1.

The mixed outer scaling as discussed by Bull (1996) and Goody (2004) uses the same form as above, except instead of scaling on the boundary layer thickness δ and the friction velocity u_t, the displacement thickness δ^* and the edge velocity U_e are used to scale the low frequency pressure spectra through $\Phi(\omega)U_e/(\tau_w^2\delta^*)\ vs.\ \omega\delta^*/U_e$. Forest (2012) again showed data from Blake (1970), Farabee and Caserella (1991), and Forest (2012) collapsing to a single curve across studies for the low frequencies within the measurement uncertainty as seen in Figure 2. Therefore, both outer scaling methods are recognized methods of scaling the low frequency smooth wall pressure spectra.

In order to scale the high frequencies for smooth walls though, it is generally accepted that the viscous scaling, $\Phi(\omega)u_\tau^2/(\tau_w^2\nu)\ vs.\ \omega\nu/u_\tau^2$ will collapse the pressure fluctuations generated from small turbulent eddies within the inner portions of the boundary layer. Farabee and Casarella (1991), Goody (2004), Gravante *et al.* (1998), and Forest (2012) among others were able to show a clear collapse at high frequencies by applying this viscous scaling to smooth wall data. As another example from Forest (2012), Figure 3 shows a collapse of Farabee and Caserella (1991) and Forest's (2012) data using this scaling. Forest (2012) stated that Blake's (1970) data could not be included, however since the viscosity of each test case was not included in his presented findings.

Interestingly though, the scaling for both the inner and outer regions of the smooth wall pressure spectra also collapses the mid frequencies as seen in Figures 1, 2, and 3, which initially suggests the existence of an overlap region, where both inner and outer variables are thought to

apply. The overlap region is conventionally defined as the linear region on the semi-log scale existing in the mid frequencies. This region has been found to have a frequency width dependent on Reynolds number as stated by Goody (2004). Panton and Linebarger (1974) made the argument using a variation of Lighthill's equation that an inner and outer smooth wall scaling should independently collapse the overlap region in the same manner, and that the slope of this region should show a ω^{-1} dependence.

However, this has yet to be seen experimentally, since most smooth wall pressure spectra such as (Blake 1970, Farabee and Casarella 1991, Goody 2004, McGrath, Simpson 1987, and Forest 2012) yield a slope between $\omega^{-0.7}$ and a $\omega^{-0.83}$. Hence previous studies have reasoned that their results do not match this ω^{-1} dependency because they were not able to achieve high enough Reynolds numbers. Forest (2012) argued that an inability to reach high Reynolds numbers may not be the true explanation behind the failure to achieve the ω^{-1} dependency, since Forest (2012) study's high Reynolds number results match those of the given investigations above. Furthermore the rough wall pressure spectra scalings analyzed in Section 3 do not appear to collapse either the high or low frequencies in conjunction with the mid-frequencies. This would tend to suggest that the observed linear mid-frequency region in the surface pressure spectrum may be more complex than previously thought, especially for fully rough flows, and further investigation is needed.

1.2.5 Rough Wall Flows

This study will now shift its attention to the previous rough wall findings. Any addition of the presence of roughness to the hydraulically smooth wall begins to impart significant changes within the turbulent boundary layer. Unlike the smooth wall scaling though, the rough wall inner scaling has largely been ignored, and the outer scaling has yet to be definitively resolved. Thus in this section each rough wall study reviewed will be explored for their attempts to capture the necessary scaling parameters of the rough wall pressure spectra. Figures depicting each of the scalings discussed below can be found in Chapter 3 along with an in depth analysis.

Blake's (1970) study was able to show that the low frequency pressure spectrum for both smooth and rough wall flows scaled on mixed outer variables, which suggested that the surface conditions shared similar sources for the low frequency pressure fluctuations. However, the exact nature of the turbulence production was not explored. Blake also found that when scaled on classical outer variables, the high-frequency portion of the rough wall pressure spectra was offset from that of the smooth wall only by the Strouhal number $\omega k_g/u_\tau$. From this result, Blake attempted to resolve the high frequency pressure spectrum using the scaling $\Phi(\omega)u_\tau/(\tau_w^2 k_g)\ vs.\ \omega k_g/u_\tau$, and saw an improved, but not complete mid and high frequency collapse. Blake attributed the minor variations seen in the scaling between the surface roughness configurations to the element spacing ratios and concluded that the high frequency pressure spectrum was primarily due to wake-like shedding off of the top of roughness elements along with a slight dependence on roughness separation.

Aupperle and Lambert's (1970) study attempted to determine a generic normalization that correlated the measured pressure spectra of their three roughness configurations. They saw from their results that the local flow effects can be ignored if the roughness elements remain relatively small, and that the spectra density appeared to be strongly dependent on roughness size. These results were reflected in their scaling $\Phi(\omega)/(\tau_w^2\ C_f)$ vs. $\omega k_s/u_\tau$, where a notable collapse of the rough wall pressure spectra could be achieved for the low to mid frequencies. However,

Aupperle and Lambert (1970) were unable to obtain a complete collapse of the rough wall high frequency pressure spectra, and so the search continued.

Blake (1971) later went on to review his previous findings by applying his scaling to data from Aupperle and Lambert (1970). When their data was plotted in conjunction with Blake's, some collapse was observed in the mid and high frequencies across studies. However, variations in the high frequency collapse were apparent in Blake (1970) and Aupperle and Lambert's (1970) data. It is interesting to note that for both data sets these variations were much less pronounced in the mid-frequency regions, which suggests Blake's scaling captures at least part of the fundamental phenomenon at work.

Varano (2010) began with Blake's (1970) scaling, and found that it provided a fair collapse of his high frequency pressure spectra. Varano (2010) then went on to argue that the friction velocity u_τ, should be proportional to the edge velocity U_e in the fully rough regime. Under this assumption, Varano (2010) modified Blake's scaling and used k_g/U_e vs. $1/\rho^2 U_e^4$ to collapse the high frequency pressure spectra. The result was a scaling that showed a comparable collapse to that of Blake's (1970) scaling, and Varano (2010) concluded that the element spacing was not an important factor when concerned with scaling the high frequency surface pressure spectra.

Finally, Forest's (2012) results showed that for the low frequency pressure spectra, his data collapsed well with Blake's (1970) when both classical and mixed outer scaling were applied. However, only the mixed outer scaling provided some measure of collapse between the smooth and rough wall flows under similar conditions. Forest (2012) also explored Blake (1970) and Varano's (2010) scaling and found that it failed to collapse his high frequency pressure spectra. Thus in an attempt to include some viscous scaling at the highest frequencies, Forest (2012) postulated that a meshing of timescales was needed in order to scale the high frequency pressure spectra. The scaling ν/u_τ^2 is based in the viscous timescale for the wall bounded flow, whereas Blake's scaling k_g/u_τ reflects the time scale for the roughness elements. Forest (2012) argued that even for fully rough flows, both timescales may still influence the near wall turbulent structures. This led him to take the geometric average of both time scales yielding a spectral scaling of the form $\Phi(\omega)u_\tau^2/[\tau_w^2\nu(k_g)^{0.5}]\ vs.\ \omega\nu(k_g)^{0.5}/u_\tau^2$, and since there is no *a priori* reason to choose the geometric roughness size k_g over the effective sand grain roughness k_s in this formulation, Forest (2012) also considered the form $\Phi(\omega)u_\tau^2/[\tau_w^2\nu(k_s)^{0.5}]\ vs.\ \omega\nu(k_s)^{0.5}/u_\tau^2$. Forest (2012) found that this proposed scaling provided an improved though not perfect collapse of the mid and high frequency portions of the spectra across studies, and surface configurations.

The investigations selected also analyzed the cross-spectra data for the hydraulically smooth and fully rough turbulent flows. Bull (1967) gives an overview of the smooth wall findings for the space-time correlations of the pressure spectra progression. Several studies in his review as well as Aupperle and Lambert (1970), Blake (1970) and Forest (2012) show that over short distances the high frequency turbulent structures found in the inner portions of the boundary layer were the dominant contributors to the coherence. As the separation is increased however, the higher frequencies rapidly lost coherence leading to a low frequency dominance. These results can also be seen in fully rough turbulent flows, along with the following conclusions drawn from the reviewed investigations.

Aupperle and Lambert (1970) explored the space time correlations and coherence functions to describe the progression of the pressure field for two roughness configurations: the 4 and 12 roughness grits. Aupperle and Lambert observed only a minor dependence on roughness configuration; however they did find that the space-time correlations had a significant link to the

differences in convection velocities. They also found that the only difference between smooth and rough walls at low frequencies was a more rapid decay in correlation due to the roughness, and at higher frequencies the coherence was largely destroyed.

Blake (1970) was another study that analyzed the space-time correlations for both smooth and rough wall configurations, and found that the convection velocity of the rough walls was smaller than that of the smooth wall for all cases. The coherence for the smooth and rough surface conditions remained largely the same for the outer region turbulent structures, however, Blake did observed a minor dependence on roughness spacing. The coherence of the small turbulent structures was significantly influenced by surface roughness, and decayed much more rapidly than that of the smooth wall matching the findings of Aupperle and Lambert (1970). Blake (1970) reasoned that this was due to the differences in roughness height, which led to changes in the turbulence production near the wall.

Finally Forest (2012) examined the two point pressure fluctuation measurements for both the smooth and rough wall surface conditions, and he found that the decay mechanism present in the smooth wall flow is not significantly disrupted, other than an increase in its rate, by the 3-mm roughness elements. This again matches the results found by Aupperle and Lambert and Blake (1970). The convective ridge of the 3-mm roughness was also observed to broaden for the space time correlations as compared to the smooth wall. Forest (2012) attributed this to the interference the roughness elements had on the convective velocities within the inner portions of the boundary layer, which he determined to be strongly influenced by the blockage ratio δ/k_g.

1.3. Objectives

The aim of this study is to investigate the pressure fluctuations of a two dimensional, zero pressure gradient flow for 3-D, k-type roughness within the fully rough regime of $k_s^+ > 80$, and with a sufficiently large blockage ratio of $\delta/k_g > 50$ to avoid disrupting large portions of the boundary layer. The fairly well-understood hydraulically smooth wall condition for a high Reynolds number turbulent flow will also be considered in the analysis with the hopes of determining a more universal perception of the high Reynolds number turbulent boundary layer structure and surface pressure fluctuation behavior over a wide range of surface conditions. More specifically this study will try and analyze the evolution of the pressure spectra of the turbulent boundary layer of a specific flow as the surface roughness presence is increased by varying the size, spacing and shape.

The Virginia Tech Stability Wind Tunnel was utilized to measure the streamwise and spanwise surface pressure spectrum of a smooth wall, 1-mm hemisphere square array with an element separation of 5.5 mm and a 3-mm hemisphere randomized array with the same number of elements as Forest's (2012) 3-mm hemisphere ordered square array with an element spacing of 16.5mm. Each roughness array continuously spanned the 1.76 x 7.32 m test surface. These surface conditions were then tested at 20, 30, 40, 50, and 60 m/s. The objectives of this investigation include to:

- Examine the scaling on outer variables of the surface pressure spectra for both smooth and rough wall high Reynolds number flows
- Investigate the high frequency turbulence structures impact on the rough wall pressure field for both smooth and rough wall high Reynolds number flows, and determine the inner variables necessary to scale this region
- Develop a comprehensive scaling that unifies both smooth and rough wall high Reynolds number flows, and determine its implications.
- Explore potential scaling methods for the mid-frequency region of the rough wall pressure spectra at high Reynolds numbers
- Develop and explore an empirical model which could be used to describe the essential features of the wall pressure spectra
- Examine the two point pressure fluctuation measurements of the 1-mm ordered and 3-mm random rough wall surface conditions.

CHAPTER 2. APPARATUS AND INSTRUMENTATION

2.1. Virginia Tech Stability Wind Tunnel

This investigation was conducted in the Virginia Tech Stability Wind Tunnel, which was first acquired back in 1959 from NASA Langley. The wind tunnel, shown in Figure 4, consists of a continuous single return design capable of producing speeds in excess of 80 m/s and Reynolds numbers reaching 5,000,000 per meter in an unobstructed test section. This is due in part to the 0.45 MW variable DC motor connected directly to the 4.27m diameter fan consisting of 8 Clark Y airfoil sectioned blades, which is capable of spinning at a max rpm of just over 600. In order to mitigate any cyclic unsteadiness, the motor is controlled by a custom designed Emerson VIP ES-6600SCR drive.

Once the flow leaves the fan, it enters the air-exchange tower, where the temperature is able to stabilize with that of the atmospheric temperature. From here turning vanes redirect the flow into a 5.5 x 5.5 m settling chamber housing 7 turbulence reducing screens with a 60% open air ratio. The flow then continues on through a 9:1 contraction nozzle before reaching the test section with a turbulence level of 0.03% at this study's maximum testing speed of 60 m/s (Remillieux *et al*. 2008). After leaving the test section, the flow encounters 8 evenly spaced vortex generators along the entrance of the three degree tunnel diffuser before reaching two more sets of turning vanes on its way back to the fan.

Recent upgrades as described by Smith *et al*. (2005), Crede (2008), and Remillieux *et al.* (2008) were made to the Stability Wind Tunnel allowing for the facility to run in an acoustically quiet configuration, while still maintaining its favorable aerodynamics (Remillieux *et al.* 2008 and Devenport *et al.* 2010). A foam fan liner was added and shown to reduce tip gap and tip noise by almost 6-dB across all frequencies (Remillieux *et al.* 2008). The turning vanes nearest the exchange tower were also treated with melamine foam in order to act as an acoustic baffle for the fan and motor. The rest of the facility and downstream of the test section was covered with 50-mm thick Urethane foam liner in order to help eliminate any high frequency acoustic reflections.

The facility also maintains removable aerodynamic and anechoic test sections that are each 7.3 m long with square cross sections of 1.83 x 1.83 m. The anechoic test section (Devenport *et al.* 2013), shown in Figure 4, was employed for this study and has port and starboard walls made of stretched Kevlar fabric that are able to direct the flow while still remaining acoustically transparent. Acoustically treated chambers are attached to both sides of the test section, and eliminate reflections above 190 Hz (Remillieux 2008). The floor and ceiling of the test section are also acoustically treated. However, in order to maintain structural rigidity, the Kevlar here is stretched over perforated aluminum plates backed by foam wedges. Therefore, this facility provides sufficient aerodynamic and acoustically quiet platform in which to conduct boundary layer and surface pressure fluctuation measurements.

2.2. False Wall

In order to grow large high Reynolds number turbulent boundary layer flows within the anechoic test section, the starboard Kevlar window was replaced with a hard-wall consisting of six modular 1.22 x 1.78 m framed Lexan panels. This modification detailed in Forest (2012) resulted in a hemi-anechoic type configuration as seen in Figure 4. Each of the Lexan panels was bonded to an 80/20 aluminum frame shown in Figure 5, and designed to slide along a set of 80/20 slotted rails via 8 right angle brackets. This allowed for movement in both the streamwise and lateral (into the flow) directions. Spacers were added to prevent any outflow of air from the test section, and were mounted along with the rails on 24 aluminum panels, which replaced their perforated Kevlar counterparts in order to obtain a greater structural rigidity. The Lexan panels were positioned within 5 mm in the streamwise direction and 0.25 mm in the lateral direction of each other, and the gaps between panels were covered with packing tape with a maximum thickness of 0.076 mm. The end result was panels that could be maneuvered to form a continuous, hydraulically smooth 1.78 x 7.32 m test surface with a zero pressure gradient as seen in Figure 6.

The coordinate system can be found in Figure 7, where the x, y, and z coordinates correspond to the streamwise, spanwise, and wall normal coordinates with velocity components u, v, and w respectively. The origin of which is located at the primary trip at the centerline and flush with the testing surface.

The false wall nominally sits 0.1m inside of the standard test section. Therefore, in order to create a smooth transition for the flow and bridge the step between the tunnel contraction and the false wall, a 2.4 x 2.4 m curved fairing made of wood ribbing and an ABS plastic skin was attached to the leading edge of the false wall as seen in Figure 6. This fairing also has two built-in mounting locations for full length trips that can be attached at hard points 1.2 m (primary trip) and 2.1 m (forward trip) upstream of the test surface shown in Figure 6. Both trips placed at these positions were made of aluminum angle with a height of 19 mm as seen in Figure 8. This configuration produced a boundary layer thickness in excess of 0.24 m at 60 m/s for the rough surface pressure fluctuation measurement locations 6.98 m downstream of the primary trip.

2.3. Rough Surfaces

Two roughness fetches were manufactured for this investigation, and the full manufacturing procedure can be found in Appendix A. The roughness fetches were made using a fiberglass-paper composite with a 3:1 ratio epoxy resin coating. Hemispherical roughness elements were formed by pouring the epoxy resin into a 1.8 x 1.2 m HDPE mold and overlaying the fiberglass-paper composite as a backing. The roughness fetches were then attached to the false wall by using silicon sealant and super glue to bond them to 3-mm thick 1.8 x 1.2 m aluminum plates, which were bolted onto the test surface. The fetches and panels were adjusted in order to ensure that no gaps, dislocations or seams were apparent to the flow, and that the zero pressure gradient was still maintained. This method allowed for a removable, continuous deterministic rough surface spanning the entire testing surface which is 1.78 x 7.52 m.

A 0.12m gap existed between the end of the contraction and the start of the testing surface. This gap was bridged using 0.001 m thick brass shim. The testing surface began

1.19m downstream of the primary trip as seen in Figure 8, which marks the leading edge of the test section. Both roughness fetches were positioned so that they began precisely at this point.

The first roughness fetch consisted of 1-mm radius hemispheres spaced in a 5.5 mm square array shown in Figure 9 (a), which is 1/3 the scale of the 3-mm ordered array tested by Forest (2012). The purpose of this surface was to explicitly examine roughness Reynolds number, and roughness size to boundary layer thickness ratio effects, relative to the 3-mm ordered surface studied by Forest (2012). The second fetch, shown schematically in Figure 9 (b), consisted of 3-mm radius hemispheres spaced in a random, but known configuration having the same element density as that of Forest's 3-mm ordered array. This surface was designed explicitly to test the dependence of the boundary layer, and in particular, the wall pressure fluctuation field, on the distribution of roughness elements.

The random spacing of the 3-mm array tested in this investigation was obtained using a pseudo-random algorithm developed in Matlab. Since the mold would produce six identical surfaces, the statistical probability of the locations of the roughness elements across panels had to remain the same. This was achieved by populating the surface of a cylinder matching the height and circumference of the final roughness fetch, with 3-mm hemispherical roughness elements. The cylinder was then analyzed to determine the ideal location to make a vertical cut disrupting the amount of hemispheres, and was flattened and overlaid on the instrumentation locations. If any roughness elements came within 4-mm of this instrumentation, the process was repeated until an acceptable fetch was produced. No other restrictions were placed on the element locations. The final roughness element spacing and instrumentation locations (shown in red) can be seen in Figure 10.

2.4. Boundary Layer Instrumentation

Detailed boundary layer velocity fluctuation measurements were made for flows over the 1-mm ordered and 3-mm random rough surfaces, as well as control measurements of the smooth wall flow. These measurements were taken using both single and four sensor hotwire anemometer probes to reduce uncertainty. The four sensor hotwire type AVOP-4-100 model made by the Auspex Corporation consisted of 2 perpendicular pairs of 45 degree etched tungsten x-wires with a 5 μm diameter. This yielded a 0.75 mm^3 measurement volume and allowed for measurements of the three components of flow velocity.

A Dantec Dynamics Streamline Constant Temperature Anemometry (CTA) system was used to operate both single and 4-component sensors. The reference transducer hotwire anemometer signals were recorded using a 64 channel 16-bit Agilent E1432 digitizer and signal analyzer, with outputs being adjusted for ambient temperature fluctuations. A flat frequency response below 18 kHz was observed for both probes.

The three dimensional flow calibrations for the quad-wire system were performed in an isolated jet of known velocity. The probe was placed parallel to the flow and the velocity was varied allowing for the output voltage and flow velocity measurements to be related via King's law. The quad-wires were then pitched and yawed by up to +/- 45 degrees to obtain the probe angle calibration, which was applied to the boundary layer profile measurements made in the wind tunnel by using the look-up table method of Wittmer *et al*.

(1998). Velocity calibrations were also made for each probe type in the wind tunnel free stream between data sets.

Three component boundary layer profiles were taken using the quad-wire system 6.98 m downstream of the primary trip centered between a group of roughness elements as seen in Figure 11 (a) for the 1-mm ordered roughness and Figure 11 (b) for the 3-mm random roughness. These profiles were taken from 1.75 boundary layer thicknesses away from the wall, well within the free stream, down to 3-mm away from the wall. Wittmer *et al.* (1998) showed measurements in a similarly scaled turbulent pipe flow to be free of gradient errors down to 3-mm from the wall. Single wire profiles were also taken 6.98 m downstream of the primary trip to within 0.5 mm of the wall.

The hotwire probes were mounted to a 3-axis traverse system capable of movements down to 0.025 mm within the test section as seen in Figure 12. When fully installed the traverse creates an 11% blockage ratio within the test section requiring a higher fan speed for the same velocity. The traverse system consists of 2 floor and 2 ceiling rails allowing for movement in the *x*-direction, 2 vertical rails facilitating movement in the *y*-direction, and one horizontal rail responsible for movement in the *z*-direction. Two 1.0 m stings were then mounted 0.15 m apart to the horizontal section of the traverse system, which provided active vertical vibrational dampening at higher speeds to a 0.46 m rod extending in the wall normal direction as seen in Figure 13. A two axis probe mount was attached to the end of the rod allowing for the probe to be pitched and yawed.

The single and quad-wire probes were positioned at a 0 degree pitch angle and a slight yaw angle for all cases in order to achieve the correct placement in relation to the wall. The pitch was set using an inclinometer capable of measuring angles down to 0.1 degrees. The yaw was then determined by taking a photo using a camera measured to be directly overhead of the probe with a reference line in the background verified to be parallel to the flow, and finding the angle created between them.

The photos were reprocessed to account for lens distortion. A transformation matrix was obtained using 15 calibration photos of a black and white grid of 1.2 x 1.2 inch squares taken at various angles. An example calibration photo can be seen in Figure 14. The angle at which the calibration photos were taken was determined from the apparent length of the squares within the grid. These angles and the amount of adjustment necessary to force the lines within the grid to become parallel were interpolated to find the correction matrix for the lens distortion at any angle. This lens correction is then applied to measurement photo undistorting the image. The result is an accurate way of determining the angle of the probe to the flow within 0.2 degrees. Figure 15 (a) and (b) shows the undistorted measured yaw angles of 4.5 and 9.3 degrees for the quad-wire used in the measurements of the 1-mm ordered and 3-mm random rough surface conditions respectively.

Small yaw angles of the quad-wire probes are easily accounted for in the post processing analysis rotation using the angle calibration file. However, Borgoltz (2007), Morton (2012), and Forest (2012) found that larger angles greater than 8 degrees began to show reduced Reynolds stress tensors as compared to data taken simultaneously with probes at smaller angles. Borgoltz (2007) and Forest (2012) reasoned that the differences in Reynolds stress profiles were caused by errors in the local shape of the calibration surface for high angle probes, since the mean velocities were constant across different probe angles as was seen between the comparison of the small and large angle probe data. They therefore assumed the data from the smaller angle probes to be correct and

developed a transformation method to adjust the higher angle probe data. This transformation matrix was determined by minimizing the differences between the low and high angled probes as detailed in Borgoltz (2007). The present study did not have a low angle probe for comparison, but instead used similar data following Forest (2012) from Borgoltz (2007) and Morton (2012) to develop the transformation matrix. This resulted in only minor adjustments to the Reynolds stress tensors for the 1-mm ordered and 3-mm random rough surfaces, which was to be expected, since the yaw angles for each condition were close to 8 degrees.

An uncertainty analysis was completed using Jitter analysis for quad-wire measurements of the 1-mm ordered and 3-mm random surface conditions at 30 and 60 m/s, the results of which can be found in Table 1. The uncertainty analysis took into account, but was not limited to the uncertainty in determining distance, angles, calibrations, and flow properties. All of the uncertainties were found to be well within reason for the types of measurements being made in this study.

Table 1: Quad-hotwire average absolute uncertainties

Type: Speed	u/Uref	v/Uref	w/Uref	$u'^2/Uref^2$	$v'^2/Uref^2$	$w'^2/Uref^2$	$u'v'/Uref^2$	$v'w'/Uref^2$	$u'w'/Uref^2$
1-mm: 30 m/s	0.008	0.016	0.027	0.0002	0.0013	0.0021	0.0006	0.0002	0.0001
1-mm: 60 m/s	0.007	0.015	0.026	0.0002	0.0011	0.0018	0.0005	0.0002	0.0001
3-mm Rand: 30 m/s	0.008	0.016	0.027	0.0002	0.0014	0.0024	0.0006	0.0002	0.0001
3-mm Rand: 60 m/s	0.007	0.015	0.026	0.0002	0.0012	0.0020	0.0005	0.0002	0.0001

2.5.Surface Pressure Instrumentation

2.5.1 Mean Wall Pressure

Mean wall pressure measurements were made using twenty-four ½ mm pressure taps located along the floor and ceiling of the test section bounding the test surface. The pressure taps are positioned in a row parallel to the flow between 0.25 and 0.36 m away from the test wall and spaced every 0.61m. The variation in spacing allows for boundary layer growth along the testing surface. The locations of the pressure taps can be found in Table 2, and Figure 16 shows the placement of some of the pressure taps within the test section. Data from the pressure taps was collected using an Esterline Netscanner Model 98 RK pressure scanner. The assumption was made that the mean static pressure was constant throughout the boundary layer, and thus the pressure gradient of the wall could be established through this measurement. The testing surface was then adjusted to ensure a zero pressure gradient for both the smooth and rough surface conditions.

Table 2: Locations of mean wall pressure measurements

X (m)	1.6	2.15	2.76	3.37	3.98	4.58	5.19	5.8	6.41	7.02	7.62	8.13
Y (m)	+/-0.92	+/-0.92	+/-0.92	+/-0.92	+/-0.92	+/-0.92	+/-0.92	+/-0.92	+/-0.92	+/-0.92	+/-0.92	+/-0.92
Z (m)	0.18	0.18	0.18	0.18	0.18	0.18	0.18	0.18	0.19	0.19	0.19	0.19

2.5.2 Surface Pressure Fluctuations

Surface pressure fluctuations were measured using five Brüel and Kjaer (B&K) type 4138-A-015 1/8th inch microphones fitted with ½ mm pinhole caps shown in Figure 17 and data was collected through a B&K type 3050-A-060 Pulse Analyzer sampling at 65536 Hz for 32 seconds. Devenport *et al.* (2010) was able to show that under a wall jet boundary layer the pressure fluctuations could be resolved up to 20 kHz using Sennheiser KE 4-211-2 electret condenser microphones fitted with a ½ mm pinhole cap.

The amplitude and phase response of the five B&K type 4138 microphones fitted with pinholes were calibrated in an anechoic chamber using the unaltered model 4138 microphone as a reference. The Agilent VXI system was used to generate white noise through a University Sound ID 60 C8 speaker. It is important to note that the limitations of the speaker did not allow for white noise below 250 Hz to be produced; however, the effects of the pinhole were found to be negligible below 1000 Hz for all frequencies. The calibration system received power from a Monster Automatic Voltage Stabilizer type 2000, which helped to reduce the signal to noise ratio of the stereo analog components.

The microphone calibrations were obtained using the same technique as described in Alexander *et al*. (2009) and Forest (2012). The reference microphone was initially positioned within a thin microphone stand so that it was level with and oriented directly at the speaker 2.6 m away as seen in Figure 18. The white noise was then recorded for the reference microphone and subsequent pinhole microphones. Great care was taken to make sure that each microphone was placed in the same exact position +/- 0.02mm as the reference microphone.

The microphone calibrations were then found as the response of the microphone pinhole system divided by the response of the reference microphone. The complex frequency response was fitted and modeled by the ratio of two polynomials shown in Equation 1.

$$R(\omega) = \frac{b_1\omega^n + b_2\omega^{n-1} + \cdots + b_{n+1}}{a_1\omega^2 + a_2\omega + a_3} \qquad \text{Equation 1}$$

Forest (2012) found that a second order fit worked best for the pinhole microphones, and an example raw calibration with an optimized fit can be seen in Figure 19 (a) for the amplitude and Figure 19 (b) for the phase.

Forest (2012) also showed that the damping effect of the pinhole on the microphone calibration is Reynolds number dependent. As the Reynolds number increases the relative magnitude of the viscous effects on the system decreases and lowers the effective dampening due to the pinhole. Therefore during post processing of the data, the microphone calibrations were optimized to account for these variations. Optimization was achieved by finding a combination of system dampening (a2) and resonant frequency (a1) multipliers, which would yield a minimum RMS level of deviations in the high frequency

portion of the spectrum of the derivative of the spectral level with frequency. Care was taken to ensure that this process only identified with features of the spectrum that could clearly be ascribed to the altered high frequency response of the microphone. Forest (2012) found and this study confirmed, that the resonant frequency typically shifted by less than 4%. The dampening of the pinhole system however, was reduced by up to a maximum of 40% at 60 m/s with corrections becoming negligible at 20 m/s.

The microphones were positioned in streamwise and spanwise arrays enabling space time correlation. The streamwise array allowed for the determination of the convection velocities of the turbulent structures, and the spanwise array identified the size of the turbulent structures, and also provided some insight into the two dimensionality of the flow. In order to place these arrays, instrumentation holes were cut in the false wall to accommodate microphone holders, seen in Figure 20 (a), made from an Objet Alaris 30 3D printer. Figure 20 (b) and (c) show the mounted microphone holders in relation to the 1-mm ordered and 3-mm random roughness elements respectively. Any unused holes during testing were filled with plugs. These microphone holders were designed by Forest (2012) to keep microphones flush to within +/- 0.02 mm, and when placed in the false wall were made flush to within +/- 0.2mm of the top of the substrate of the roughness. No corruption of the surface pressure spectra was found to be present with step heights below 0.5 mm. The final microphone positions for both smooth and rough wall can be found in Table 3.

Table 3: Microphone locations used in surface pressure measurements

x (m)	y (m)	z (m)
6.275	0.340	0
6.555	0.340	0
6.770	0.340	0
6.935	0.340	0
6.941	0.340	0
6.968	0.340	0
6.984	0.340	0
7.067	0.340	0
6.984	0.269	0
6.984	0.262	0
6.984	0.236	0
6.984	0.219	0
6.984	0.137	0
6.984	-0.028	0
6.984	-0.193	0
(Ref) 6.984	-0.36	0

Figure 21 shows the microphone positioning in relation to the primary trip on the 5th Lexan panel which begins approximately 6.1 m downstream of the primary trip. The five microphones were positioned at 8 distinct streamwise separations and 7 distinct spanwise locations. Since there were only five microphones, data was taken at each location multiple times as the microphones were rotated through positions.

A sixth unaltered B&K type 4138 microphone with a flat (+/- 1 dB) frequency response up to 25.6 kHz was also used to measure the low frequency acoustic background of the

wind tunnel. It was positioned 6.98m from the primary trip and -0.36m from the testing surface centerline such that the turbulence pressure spectrum was found to be completely uncorrelated with the other microphones. This meant that the background noise could be removed from the raw surface pressure measurements of the other five microphones during post possessing through acoustic cancellation.

Horne (1990) first showed that the wall pressure spectrum could be broken down into the contribution from turbulence and the contribution from the background noise. This led Forest (2012) to expand upon Horne's work and position the reference microphone such that the only correlation between it and a specific measurement position would be the contribution from the background noise. Once the background noise was identified, it could then be subtracted out of the measured raw surface pressure spectrum of interest, since the sum of the background and turbulence pressure spectra make up the total wall pressure spectrum. Forest (2012) improved upon Horne's (1990) method by eliminating any possible microphone location bias through the use of a cancellation scheme that that subtracts the average of the background acoustic signal in the cross spectra taken between all microphone locations and the reference position. It is important to note that significant background noise was only observed in the auto-spectra below 100 Hz with a broadband contamination not exceeding 3-dB for frequencies above 12 Hz. A common spike found at 34.75 Hz in all pressure spectra was also significantly reduced through this cancellation method, and any low signal to noise ratios were also removed.

To reduce uncertainty, duplicate auto and cross spectra data sets from the microphone rotations (4 in total) were combined as an arithmetic mean by frequency. Matching locations produced nearly identical results for all frequencies above 100 Hz. The uncertainties due to equipment, calibrations, and the effects of the pinhole dampening were taken into account, and the final estimated uncertainties for the measured wall pressure spectra can be found in Table 4. These estimated uncertainties closely matched those of Forest (2012) for the high frequencies, but were slightly greater in the low frequencies.

Table 4: Surface Pressure Spectrum Uncertainty by Frequency

Frequency Range	Uncertainty (dB)
< 25 Hz	+/- 3.7
25 Hz to 100 Hz	+/- 3.3
100 Hz to 15 kHz	+/- 1.9
>15 kHz	+/- 3.8

For frequencies above 15 kHz, a majority of the uncertainty stems from Forest's (2012) analysis of the dimensionless pinhole diameter, and how it pertains to sensor attenuation. The dimensionless pinhole diameter $d^+=du_\tau/\nu$, according to Gravente *et al*. (1998), has to be less than 18 to ensure that no sensor attenuation occurs for frequencies up to $\omega\nu/u_\tau^2 = 1$. Forest (2012) went on to show that the sensor requirement may not need to be as stringent as Gravente suggests, since the Nyquist frequency was limited to 26 kHz by the instrumentation. Therefore, microphone attenuation should only be of concern for the very highest frequencies.

CHAPTER 3. ANALYSIS AND DISCUSSION

3.1. Measurement Overview

The main focus of this investigation is to use wall pressure spectra measured as part of the present and previous studies to determine a comprehensive scaling method for high Reynolds number turbulent boundary layer flows free of any transitional effects. Two point space time correlations will also be explored in order to understand the convective properties and allow for some insight into the size of the turbulent eddies. In the present work, mean wall pressure, boundary layer, and surface pressure fluctuations were measured for three different surface conditions: the smooth wall surface condition, the 1-mm ordered hemispherical roughness condition and the 3-mm random surface condition and compared to similar investigations. Table 5 shows a summary of the measurements made for the surface conditions investigated.

Table 5: Summary of measurements made for each surface condition

Measurement	Wall Condition	Locations	U_∞
Mean Wall Pressure	Smooth Wall	See Table 2	20,30,40,50,60 m/s
	1-mm Ordered	See Table 2	20,30,40,50,60 m/s
	3-mm Random	See Table 2	20,30,40,50,60 m/s
Single Hotwire	Smooth Wall	x= 6.98 m y=-1.52, 1.52 m z=0.001 to 0.4m	30, 60 m/s
	1-mm Ordered	x= 6.98 m y= 0 m z=0.001 to 0.4m	30, 60 m/s
	3-mm Random	x= 6.98 m y= 0 m z=0.001 to 0.4m	30, 60 m/s
Quad Hotwire	1-mm Ordered	x= 6.98 m y= 0 m z=0.003 to 0.4m	30, 60 m/s
	3-mm Random	x= 7 m y= 0 m z=0.003 to 0.4m	30, 60 m/s
Surface Pressure Fluctuations	Smooth Wall	See Table 3	20,30,40,50,60 m/s
	1-mm Ordered	See Table 3	20,30,40,50,60 m/s
	3-mm Random	See Table 3	20,30,40,50,60 m/s

The mean wall pressure and surface pressure fluctuations were measured at 20, 30, 40, 50 and 60 m/s, and the boundary layer parameters were measured at 30 and 60 m/s. Surface pressure fluctuation data was collected separately from the quad and single hotwire profiles, and was taken using multiple configurations of the microphone array. Time averaged autospectrum comparisons are made for the processed data based on location, measurement speed, and study. The surface pressure spectra are then scaled and compared to other investigations using the boundary layer parameters determined from the hotwire measurements. From these results a new

roughness inner scaling is proposed and applied to all applicable studies for high Reynolds number, rough wall turbulent boundary layer flows free of any transitional effects. The coherence, phase, and correlations are also explored for the two point measurements.

3.2. Mean Wall Pressure Gradient

An essential condition of this study was to maintain a zero pressure gradient along the testing surface for each test configuration. Therefore, the average mean wall pressure was measured at the 24 locations given in Table 2. The locations were evenly spaced along the test surface on the floor and ceiling, which allowed for an unobstructed measurement independent of surface configuration. Initially, the pressure gradient along the test surface was measured in the smooth wall configuration, and the results of these measurements were used to adjust the false wall until a near-zero wall pressure gradient was obtained. The mean wall pressure gradient was then taken at every test speed for the smooth, 1-mm ordered and random 3-mm roughness configurations, yielding a maximum deviation of +/- 0.023 in C_p. This small deviation was found to be almost constant for all conditions, which meant that the false wall's initial adjustment was left as its final position throughout the investigation. The final results of the mean streamwise pressure coefficient distribution as a function of surface type for 30 and 60 m/s can be seen in Figure 22. These results are also presented with Forest's (2012) near-zero wall pressure gradients and fall within Forest's maximum tolerance of +/- 0.03 *Cp*. It is important to note that the slight pressure gradient over the downstream half of the test section for both sets of results is attributed to the physical restrictions of the wind tunnel, since the false wall could not be adjusted any further to account for the boundary layer growth on the Kevlar wall opposite that of the test surface. Forest (2012) has a marginally larger deviation in the pressure coefficient downstream because after Forest's entry the false wall underwent a minor modification, which allowed for a slightly larger adjustment range of the last panel for the present study.

3.3. Boundary Layer Wall Flow

3.3.1 Boundary Layer Classification Overview

Both single and quad component hot-wire anemometry was utilized to measure the mean velocity and turbulence profiles of the fully developed, turbulent boundary layer generated by each surface condition and flow speed. The locations and test speeds for these measurements can be found in Table 5. The boundary layer profiles taken by the single and quad hotwires are then compared to show consistency. The quad-hotwire profiles are also used to confirm boundary layer 2-dimensionality, and determine the unknown boundary layer parameters.

3.3.2 Measurement Consistency

In order to compare single and quad hotwire profiles between testing speeds, surface configurations, and studies, the profiles were scaled on the edge velocity and absolute boundary layer thickness δ. The absolute boundary layer thickness was defined as the distance from the wall where the local velocity was 99% of the free stream velocity, and was found by interpolating points through the mean velocity profile obtained by the quad-hotwire 6.98 m downstream of the primary trip. Figure 23 uses the quad-hotwire data to show an example of the boundary layer thickness determination process for the 1-mm ordered roughness condition at 30 m/s. The absolute boundary layer thickness for each measurement and surface condition can be found in Table 6, and remained relatively constant for each surface condition and test speed. The

absolute boundary layer thickness also remained roughly constant across the different surface conditions, varying from 0.21 m for the 1-mm roughness to 0.22 m for the 3-mm random roughness. These results were also confirmed by the single hotwire.

To reduce uncertainty, measurement consistency was explored for the data collected using single and four-sensor hotwire anemometry. A comparison of the non-dimensionalized z/δ vs. u/U_e boundary layer mean velocity profiles measured at 30 and 60 m/s using the two probes was made at the locations given in Table 5 for the 1-mm ordered and 3-mm random rough surface conditions. Figures 24 (a) and (b) exhibit a clear consistency between the single and quad hotwires at each test speed for the 1-mm ordered and 3-mm random surface configurations within the uncertainty limits, which provides a confirmation of the distancing techniques used to initially position the probes as explained in Section 2. It is important to note though that the quad hotwire measurements could only be made down to 0.003 m from the wall for the 3-mm random surface condition due to an increase in vertical probe vibration. The vibration was observed to be parallel to the wall with a maximum amplitude of 5 mm at 60 m/s for the 3-mm random rough surface condition. This amplitude was determined by measuring the marks left from the probe scraping against the roughness elements as it was moved to within 3-mm from the wall. Any measurements made with the probe contacting the wall were disregarded. No visual horizontal probe vibration was observed at any point throughout the measurement.

The turbulence u'^2/U_e^2 profiles obtained from the single and quad hotwire probes were also compared in Figures 25 (a) and (b) at 30 and 60 m/s for the 1-mm and 3-mm random rough surface conditions respectively. The trends for both the single and quad hotwires are almost identical for each surface condition at their respective test speed, however the single hotwire results tend to have a slightly extended curve close to the wall. This is attributed to the loss of resolution around 3-mm away from the wall as was found by Wittmere *et al.* (1998), and is due to the 0.0074 m^2 measurement area of the quad-hotwire. Although it is worth noting that the data from the quad-hotwire for the 1-mm roughness at 30 m/s deviates slightly more than expected. Barring the previous observation, the variation is small enough to conclude that the quad-hotwire measurements are valid for each surface condition and test speed down to 0.003 m away from the wall.

3.3.3 Boundary Layer Two-dimensionality

Boundary layer two-dimensionality was an essential requirement for the analysis and comparison of the results of this investigation. Figure 26 shows the non-dimensionalized smooth surface boundary layer shape profiles taken at 30 and 60 m/s for the smooth wall condition at x = 6.98 m, y = -0.152 and 0.152 m and z= 0.001 to 0.4 m for the present study and that of Forest (2012). The profiles at each location and test speed for the present study are graphically identical; however Forest's data sits slightly below that of the current studies. This difference is considered to be within the measurement uncertainty. Therefore for the purposes of this study, boundary layer two-dimensionality is assumed for each roughness configuration, since the zero pressure gradient measurements remained unchanged throughout testing.

3.3.4 Boundary Layer Turbulence Structure

Quad hot-wire anemometry was also used to measure turbulent velocity fluctuations throughout the boundary layer for the 1-mm and 3-mm roughness surface conditions. The quad-hotwire profiles of the 3 turbulence intensity components u', v', and w' are normalized on the friction velocity u_τ, and are compared in Figure 27 with data from Blake (1970) and Forest

(2012). The *w'* component has been shifted by + 0.5, and the *u'* component has been shifted by + 1 along the *x*-axis for clarity. Each of the components was found to be very similar amongst all of the roughness configurations, and is consistent with the findings of Blake (1970) and Forest (2012) though Blake's data measured at much lower Reynolds numbers tends to show higher turbulence in the outer region of the boundary layer. The turbulence intensity also appears to decease near the surface due to the roughness elements. As is expected the *u'* component dominates over most of the boundary layer. Closer inspection of Figure 27 shows that the roughness configurations with the larger $R_{e\theta}$ and δ/k_g generally have a more rapid decrease in each turbulence intensity component as they approach the wall. Forest (2012) attributed this to the larger relative size of the boundary layer to the roughness height decreasing the roughness's effects throughout the upper portions of the boundary layer.

The boundary layer turbulent kinetic energy (TKE) profiles for each roughness configuration were also explored. Figure 28 shows the TKE profiles plotted as z/δ *vs.* TKE/u_τ^2 where u_τ is the friction velocity. These TKE profiles are also compared with Forest's smooth and 3-mm rough wall results in Figure 28. The TKE for the 3-mm random roughness resembles that of Forest's 3-mm ordered roughness at 30 and 60 m/s. It is interesting to note that the TKE of the 1-mm roughness falls between the smooth wall and the 3-mm rough wall data, but more closely exhibits the 3-mm rough wall data trends. Forest (2012) also observed that the turbulent kinetic energy is roughly 20% weaker in the rough wall boundary layers than that of the smooth when measured relative to the friction velocity. This result coincides with the current findings.

3.3.5 Boundary Layer Parameter Determination

The displacement thickness δ^* and the momentum thickness θ are determined from their integral definitions given in Equation 2 and Equation 3 respectively.

$$\delta^* = \int_0^\delta (1 - \frac{u}{U_e})\, dy \qquad \text{Equation 2}$$

$$\theta = \int_0^\delta (1 - \frac{u}{U_e})\, \frac{u}{U_e}\, dy \qquad \text{Equation 3}$$

It is important to note that since the quad-hotwire could only collect data down to 0.003 m away from the wall, the near wall mean velocity had to be estimated from the wall up to this point. This was done by implementing the no slip condition at the wall and meshing the derivative of the curve created by the mean velocity profile with the derivative of a polynomial curve used to extrapolate the experimental data to zero. The result was a continuous profile, which was integrated to obtain the momentum thickness. Figure 29 shows a sample profile for the 1-mm ordered roughness condition at 30 m/s used to determine the momentum thickness. The same approach was then utilized to find the displacement thickness. From these results the various length based Reynolds numbers were then found.

3.3.5.1 Determining the Friction Velocity

The friction velocity u_τ was determined from the method outlined by Varano (2010) analyzing the Reynolds shear stress profile. This method was then compared to Schlichting's (1979) curve fit method. Varano (2010) demonstrated that the friction velocity could be determined by analyzing the turbulent boundary layer Reynolds shear stress profile. The Reynolds shear stress method utilizes the portion of the Reynolds shear stress close to the wall that essentially remains constant, since it is not as sensitive to the exact position relative to the wall. From this method, the wall-shear τ_w can be related to the Reynolds shear stress

component $\overline{u'w'}$ through Equation 4, which is then substituted into Equation 5 in order to relate the Reynolds shear stress to the friction velocity.

$$\tau_w = \rho\overline{u'w'} \quad \text{Equation 4}$$

$$u_\tau = \sqrt{\frac{\tau_w}{\rho}} \quad \text{Equation 5}$$

The relation of the Reynolds shear stress to friction velocity on the parameters zu_τ/ν vs. $\overline{u'w'}/u_\tau^2$ will produce a maximum peak value equal to one. Figure 30 shows the Reynolds shear stress scaled on the parameters zu_τ/ν *vs.* $\overline{u'w'}/u_\tau^2$ for the 1-mm ordered and 3-mm random roughness conditions at 30 and 60 m/s. 3-mm ordered roughness data from Forest (2012) is also included, and closely matches that of the 3-mm random roughness. It is interesting to note that the Reynolds stress peak in this figure varies with the boundary layer momentum thickness Reynolds number Re_θ. Fernholz and Finley (1996) concluded that the Reynolds stress peak increased in its vertical distance from the wall with increasing Re_θ, which is consistent with the results from the present study and the findings of Forest (2012).

Once the friction velocity was determined for each test speed and surface condition, the skin friction coefficient C_f, could then be found via Equation 6, where U_e is the edge velocity of the boundary layer.

$$u_\tau = \sqrt{\frac{1}{2}C_f U_e^2} \quad \text{Equation 6}$$

The results can be seen in Table 6 below.

In order to remain consistent with the previous investigations, Schlichting's (1979) method, entailing a two parameter optimization of the friction velocity and the equivalent sand grain roughness height k_s, was also utilized to determine the friction velocity, and thus the skin friction coefficient. Following this method, the near-wall behavior of the rough wall flow was assumed to be a function of position z as described by the law of the wall given in Equation 7 from Schetz (1997), where ν is the kinematic viscosity.

$$\frac{u}{u_\tau} = f\left(\frac{zu_\tau}{\nu}\right) \quad \text{Equation 7}$$

$$\frac{\Delta u}{u_\tau} = -\frac{1}{\kappa} ln\left(\frac{k_s u_\tau}{\nu}\right) - B + C \quad \text{Equation 8}$$

The log-law region of the boundary layer for the rough wall flows was defined according to the relation given in Schlichting (1979) as seen in Equation 8, where B=5.1 and the Von Kármán term $\kappa = 0.40$. The roughness function C and equivalent sand grain roughness height k_s are at this point still unknown.

The roughness function C can be regarded as a function of the equivalent sand grain roughness height Reynolds number k_s^+, which is a function of k_s. Therefore, using Equation 3.8 found in Dirling (1973), an initial estimate for k_s can be obtained from the mean roughness height k_g. It is important to note that this is an initial approximation of k_s only and is used to show that the rough surface conditions being analyzed can be considered in the fully rough regime as outlined by Jimenez (2004), since the initial approximation will under estimate the true value of the equivalent sand grain roughness height. In Equation 9, d_e is defined as the mean distance between roughness elements, A_s is the wetted surface area of the roughness as seen by the flow, and A_p is the projected roughness surface area onto a plane normal to the flow direction.

$$\Lambda = \frac{d_e}{k_g}\left(\frac{A_s}{A_p}\right)^{\frac{4}{3}}$$

Equation 9

$$k_s \approx \frac{k_g}{\vartheta}, \qquad \vartheta = \begin{cases} 60.95\Lambda^{-3.78} & if\ \Lambda < 4.915 \\ 0.0072\Lambda^{1.9} & if\ \Lambda > 4.915 \end{cases}$$

From this method, the initial approximate values of k_s were found to equal 0.00094 m for the 1-mm roughness and 0.00282 m for the random 3-mm roughness, yielding an initial approximate value of k_s^+ equal to 82.02 and 261.04 for the 1-mm and random 3-mm roughness respectively at 30 m/s. According to Schlichting (1979), this result is within the fully rough regime of $k_s^+ > 70$, thus the roughness function C in Equation 7 and 10 can be taken as a constant equal 8.5, since it does not vary for fully rough flows.

The von Kármán term $\kappa = 0.40$, and the determined constant roughness function C were then applied using the simplified log-law relation given in Equation 10, from Schlichting (1979), for rough wall flows in order to obtain the theoretical trend for each test condition.

$$\frac{u}{u_\tau} = \frac{1}{\kappa} ln\left(\frac{z}{k_s}\right) + C$$

Equation 10

The friction velocity and equivalent sand grain roughness height are optimized in Equation 10 so that the theoretical trend matched the experimental results. An example of this can be seen in Figure 31 for the 30 m/s 1-mm ordered roughness condition.

The results obtained from Schlichting's (1971) method for the friction velocity came within 3.5 percent of the results obtained from the Reynolds shear stress method. The greatest percent difference between the two methods came at the highest test speed of 60 m/s for both surface conditions, and decreased with decreasing test speed. It is important to note at this point that determining the friction velocity, and thus the skin friction coefficient, is more accurate with the Reynolds shear stress method as shown by Varano (2010). Therefore the values obtained from the Reynolds shear stress method will be used for the remainder of the analysis of this investigation, and can be found in Table 6. Schlichting's (1971) method was used however to obtain the equivalent sand grain roughness height k_s using the friction velocity obtained from the Reynolds shear stress, which can also be found in Table 6.

3.3.5.2 Boundary Layer Parameter Results

The measured velocity profiles were normalized using the inner variables given in Equation 11, and are show in Figure 32.

$$z^+ \equiv \frac{zu_\tau}{\nu} \qquad\qquad u^+ \equiv \frac{u}{u_\tau}$$

Equation 11

Figure 32 depicts the mean velocity profiles at 6.98 m downstream of the primary trip at 30 and 60 m/s for the 1-mm and random 3-mm roughness as compared to Forest's (2012) smooth wall and ordered 3-mm roughness. These profiles are plotted in terms of the inner variables given in Equation 11. This region also tends to have the same form as that of Forest's (2012) smooth wall data; however, due to the laminar sub-layer being destroyed by the roughness elements, the log-law region is shifted down by a measure of $\Delta u/u_\tau$ from that of the smooth wall. Figure 32 also depicts a clear semi-logarithmic region for both studies rough-wall profiles, like that seen for Forest's (2012) smooth wall, and upon closer inspection shows that the results from the random 3-mm roughness and Forest's ordered 3-mm roughness are almost identical at both speeds.

Further examination of the non-dimensionalized boundary layer shapes can also be seen in Figures 33 (a) and (b), where the roughness effects are explored at 30 and 60 m/s respectively for each configuration. As is expected, the increased wall shear due to the roughness creates a velocity defect in the boundary layer. Note that the velocity defect for the ordered 1-mm is almost as strong as that for the random 3-mm, which coincides with the skin friction coefficient results shown in Table 6.

The final calculated boundary layer parameters inferred from the profiles measured 6.98 m downstream of the double 19-mm trip at 30 and 60 m/s for the 1-mm and random 3-mm roughness configurations are presented in Table 6. Forest's (2012) smooth and 3-mm rough wall data is also included italicized for comparison.

Table 6: The zero wall pressure gradient flow final boundary layer parameters using the double 19-mm trip; Forest's (2012) data is given and italicized for comparison

U_e (m/s)	X (m)	δ (m)	C_f	u_τ/U_e	δ^* (m)	Θ (m)	Re_δ	Re_θ	H	Configuration
30	*7.0*	*0.231*	*0.0023*	*0.034*	*0.0246*	*0.0198*	*419,000*	*35,700*	*1.25*	*Smooth*
30	7.0	0.212	0.0049	0.049	0.0296	0.0223	376,000	39,600	1.33	1-mm ordered
30	*7.0*	*0.219*	*0.0050*	*0.050*	*0.0321*	*0.0231*	*412,000*	*43,500*	*1.39*	*3-mm ordered*
30	7.0	0.222	0.0051	0.050	0.0336	0.0247	408,000	45,200	1.36	3-mm random
60	*7.0*	*0.231*	*0.0021*	*0.032*	*0.0249*	*0.0200*	*793,000*	*68,700*	*1.24*	*Smooth*
60	7.0	0.210	0.0045	0.047	0.0272	0.0207	731,000	72,100	1.32	1-mm ordered
60	*7.0*	*0.228*	*0.0047*	*0.048*	*0.0319*	*0.0230*	*796,000*	*80,200*	*1.39*	*3-mm ordered*
60	7.0	0.220	0.0047	0.048	0.0310	0.0231	784,000	82,700	1.35	3-mm random

Table 6, Figure 27 and Figure 32 all show that the boundary layer produced by Forest's (2012) 3-mm ordered roughness is almost identical to that generated by the 3-mm random roughness surface at 30 and 60 m/s. This would imply that roughness distribution only weakly affects the global boundary layer parameters. Table 6 also depicts a broad range of roughness Reynolds numbers from the very bottom of the conventionally accepted fully rough regime at k_g^+ = 62 for the 1mm roughness at 20m/s to over k_g^+ = 500 for the 3mm roughness at 60 m/s. In all cases the roughness is less than 1.4% of the boundary layer thickness, easily exceeding Jimenez' (2004) criterion.

3.3.6 Boundary Layer Scaling Parameters

The final boundary layer parameters will become essential in Section 3.4 for scaling the surface pressure fluctuation spectra. At this point, it is important to note that due to testing limitations, the boundary layer measurements could not be taken simultaneously with the surface pressure fluctuations; however, the flow measurements essentially remained constant between runs. Therefore, the results presented in Table 6 will be the assumed flow parameters for the surface pressure fluctuation spectra at 30 and 60 m/s. These flow parameters then had to be interpolated and extrapolated for the present study and Forest's (2012) data to fully describe all of the necessary test conditions for the surface pressure fluctuation spectra measured over a more detailed range of speeds as seen in Table 7.

Table 7 includes further boundary layer parameters for the present study as well as parameters for comparable investigations of flows over a zero-pressure gradient rough wall. The

boundary layer parameters listed in this table will be the parameters used to scale the surface pressure fluctuations discussed in the following sections. It is important to note that besides the present study and that of Forest (2012) only one other case investigated by Aupperle and Lambert (1970) met the criteria of a flow free of transitional effects as outlined by Jiménez (2004). As previously stated, these requirements are a roughness height Reynolds number of $k_g^+ > 80$, and a blockage ratio of $\delta/k_g > 50$.

Table 7: Boundary layer parameters from current and previous studies used in the surface pressure spectra scaling

	Speed (m/s)	Surface	δ^* (m)	k_g (mm)	k_s (mm)	k_g^+	k_s^+	δ/k_g	λ	u_τ/U_e
Present	20	1-mm	*0.0304*	1	*1.11*	*62*	*68*	*213*	0.052	*0.050*
	30	1-mm	0.0296	1	1.12	91	102	212	0.052	0.049
	40	1-mm	*0.0288*	1	*1.12*	*120*	*134*	*212*	0.052	*0.049*
	50	1-mm	*0.0280*	1	*1.12*	*146*	*164*	*212*	0.052	*0.048*
	60	1-mm	0.0272	1	1.13	172	195	210	0.052	0.047
	20	3-mm	*0.0345*	3	*3.32*	*177*	*196*	*74*	0.052	*0.051*
	30	3-mm	0.0336	3	3.33	260	289	74	0.052	0.050
	40	3-mm	*0.0328*	3	*3.33*	*342*	*379*	*74*	0.052	*0.050*
	50	3-mm	*0.0319*	3	*3.33*	*420*	*466*	*73*	0.052	*0.049*
	60	3-mm	0.0310	3	3.34	492	548	73	0.052	0.048
Forest	22.4	Smooth	0.0245	-	-	-	-	-	-	0.035
	33.6	Smooth	0.0246	-	-	-	-	-	-	0.034
	44.8	Smooth	0.0247	-	-	-	-	-	-	0.033
	58	Smooth	0.0248	-	-	-	-	-	-	0.033
	67.2	Smooth	0.0249	-	-	-	-	-	-	0.032
	20	3-mm	*0.0322*	3	*3.33*	*200*	*222*	*72*	0.052	*0.051*
	30	3-mm	0.0321	3	3.33	283	315	73	0.052	0.050
	40	3-mm	*0.0320*	3	*3.34*	*362*	*403*	*74*	0.052	*0.050*
	50	3-mm	*0.0319*	3	*3.34*	*436*	*486*	*75*	0.052	*0.049*
	60	3-mm	0.0319	3	3.35	507	566	76	0.052	0.048
Blake 1970	38	S-S	0.0139	1.43	2.69	177	333	41.9	-	0.052
	50	S-S	0.0146	1.43	2.69	233	440	41.9	-	0.052
	38	D-L	0.0151	2.34	4.88	311	648	26.3	-	0.057
	50	D-L	0.0151	2.34	4.88	412	861	26.3	-	0.057
	38	D-S	0.0133	1.43	1.87	172	224	40.9	-	0.050
	50	D-S	0.0133	1.43	1.87	227	296	40.9	-	0.050
Aupperle & Lambert	50	Grade 36	0.0036	0.5	2.5	81	405	56	0.0467	0.074
	50	Grade 12	0.0045	1.7	6.1	318	114	20	0.0467	0.086
	50	Grade 4	0.0051	3.8	11.9	858	268	10	0.0467	0.102
Varano	27.4	Fetch 1	0.0014	1	1.42	69	100	63.4	0.098	0.041
	20.5	Fetch 1	0.0013	1	1.42	52	72	64	0.098	0.042
	27.1	Fetch 2	0.0009	1	1.22	73	87	44.4	0.052	0.045
	19.6	Fetch 2	0.0008	1	1.22	52	62	44.5	0.052	0.044
	27.5	Fetch 3	0.0005	1	0.43	74	33	30.4	0.025	0.044
	20.2	Fetch 3	0.0007	1	0.43	52	22	48.6	0.025	0.043
	27.2	Fetch 4	0.0009	1	0.39	65	26	59.7	0.013	0.039
	20.4	Fetch 4	0.0007	1	0.39	50	20	53.2	0.013	0.040

3.4 Surface Pressure Fluctuations

3.4.1 Surface Pressure Spectrum

The raw time averaged surface pressure fluctuation spectra were measured using six B&K type 4138 microphones connected to a B&K pulse system DAQ sampling at 65536 Hz. The spanwise and streamwise positioning of the microphones can be seen again in Figure 21 and Table 3, with the spanwise portion of the array centered 6.98 meters downstream of the primary trip. Due to a limited number of microphones, wall positions were systematically rearranged for each test speed in order to obtain a larger variation of microphone separations, and the data was then averaged at each microphone location to reduce the uncertainty as described in Section 2.5.2. Comparisons of the post processed data were then made based on location, measurement speed, and study, an overview of which can be seen in Table 5.

Smooth wall pressure fluctuation data was taken using the streamwise microphone array for each test speed. The smooth wall autospectra are plotted as 1Hz bandwidth SPL relative to 20 microPascals and can be seen in Figure 34 a) and b) for the streamwise and spanwise locations respectively. Figure 34 depicts, at each test speed, a broad low frequency maximum, where boundary layer scales are expected to dominate, a rapid high frequency roll off, determined by the smallest scales in the flow, and a roughly linear mid-region in between where the inner and outer scales are both expected to apply. It can also be seen that as the test speed is increased from 20 to 60 m/s the main features of the pressure spectra remain the same, but are shifted up and to the right. The pressure field exhibits very little deviation between the different microphone locations for a fixed Reynolds number; therefore it can be considered homogeneous, and the average of the pressure fluctuations taken at each location will be used for further analysis.

The smooth wall pressure fluctuation data was compared to that of Forest's (2012) in order to explore consistency between studies. It is important to note that Forest's (2012) smooth wall pressure spectra was taken at slightly different test speeds than the current study. Forest's (2012) data was taken at 22.4, 33.6, 44.8, 56, and 67.2 m/s. Figure 35 a) and b) shows the comparison of the smooth wall autospectra between the two investigations. The current study's spectra are consistently slightly lower than that of Forest's (2012) due to the lower testing speeds; however the pressure field trends are almost identical, suggesting consistent results. Thus the smooth wall data from Forest (2012) will be used in the following analysis, since the boundary layer parameters are known for his smooth wall pressure fluctuation measurements.

The rough wall pressure spectra for the 1-mm ordered and 3-mm random rough surface conditions at all locations are shown in Figures 36 and 37. Inspection of these figures shows relatively minor deviations of the pressure field along the streamwise and spanwise rows of microphones for a fixed surface condition and Reynolds number. Therefore, in combination with boundary layer two-dimensionality and limited boundary layer growth in this region, the wall pressure spectral densities here after will be presented as averages over the microphone locations for each of the fixed flow conditions as was the case with the smooth wall pressure fluctuations.

The 3-mm random rough wall boundary layer autospectra are compared to Forest's (2012) 3-mm ordered roughness results in Figure 38. Unlike the smooth wall, these measurements were made at identical free-stream conditions. These two sets of spectra are almost the same. The only difference is that Forest's ordered 3-mm spectra rest marginally higher than those of the present random 3-mm. The shape of the wall pressure

spectrum at each speed however, remains essentially the same. This combined with the flow characteristics analyzed in Section 2 would imply that varying the roughness distribution had little effect on the resulting pressure spectrum, with the number of roughness elements remaining constant. Therefore, the random 3-mm roughness and Forest's (2012) ordered 3-mm roughness essentially produce identical results.

The effects of the surface condition on the pressure spectrum were also explored for 30 and 60 m/s. Figure 39 compares smooth wall, 1-mm ordered and 3-mm random rough surface wall pressure spectra. It is interesting to note that the rough wall spectra exhibit much the same trends as the smooth wall spectra with a broad low frequency maximum, where boundary layer scales are expected to dominate, a rapid high frequency roll off region, presumably determined by the smallest scales in the flow, and a roughly linear mid-region in between. Forest (2012) is thought to be the first to definitively observe this clearly defined linear mid-frequency region in laboratory settings for rough wall flows.

Figure 39 also shows that the smooth wall and 1-mm rough surface condition share similar high frequency behavior at each test speed, whereas the 1-mm and 3-mm rough wall surface condition share similar low frequency maxima with the 3-mm spectra resting slightly above the 1-mm spectra. Thus the mid-frequency slope increases as the surface roughness and Reynolds number are increased beginning with -0.8 for the smooth wall and ending at -4/3 for the 3-mm rough wall.

3.4.2 Scaling of the Surface Pressure Spectrum

The various scalings of the surface pressure spectrum proposed by previous researchers are examined in this section. These include scalings based on outer and inner variables and for both smooth and rough walls. Only k-type roughness, or sparsely distributed roughness, will be considered when scaling the surface pressure spectra from previous studies. The present measurements, along with data from the studies of Aupperle and Lambert (1970), Blake (1970), Farabee and Casserella (1991), Varano (2010), and Forest (2012) will be plotted together to examine the effectiveness of each scaling. The plots of Figures 41 through 53 will refer to the common legend shown in Figure 40. Aupperle and Lambert's (1970) data could not be shown for every scaling due to the inability to calculate the parameters needed for certain scalings. To provide a clear scaling-to-scaling comparison, additional plots showing only data from the present study and that of Forest (2012) will also be shown in each case.

Blake (1971) and Varano (2010) not only analyzed different roughness heights, but they also varied the sparseness ratio as well, which can be seen in Table 7. The sparseness ratio λ is a measure of the spacing between roughness elements and is determined by taking the ratio the of element frontal area to the plan form area of the surface. The sparseness ratio for the present 1-mm and 3-mm random roughness is 0.052, and Varano (2010) explored sparseness ratios varying from 0.013 to 0.09. Blake (1970) however did not present a formal sparseness ratio, but instead a change in the element spacing and size was denoted by Dense and Large D-L, Sparse and Small, S-S, and Dense and Small D-S. The effects of varying the sparseness ratio will be explored for some of the analyzed scalings.

It is very important to note that for this analysis Blake's unscaled pressure spectra was obtained from Figure 12 in Blake (1971) (or its duplicate appearing as Figure 14 in Blake (1970), which is scaled on Blake's scaling. This is significant since the these plots appear inconsistent with Figures 5 in Blake (1970) and 12 in Blake (1971) that are intended to

show the same spectra normalized on mixed outer variables. Specifically, they are off by a factor of 2 in angular frequency. This means that the unscaled pressure spectra obtained from Figure 12 in Blake (1971) would need to have ω divided by 2 in order to match the unscaled pressure spectra that is attained from Figure 5 in Blake (1970). Therefore, the figures presented here for Blake's (1970) data may be subject to change by a factor of 2 in angular frequency, once this discrepancy can be resolved.

Returning to the analysis with this in mind, there are several variations of the smooth wall outer scaling, and the most prevalent of which are discussed by Goody (1999). These outer scalings are based on the timescales δ/u_τ, δ^*/u_τ, δ/U_e, and δ^*/U_e, and provide decent measures of collapse of the low frequency smooth wall pressure spectra as long as $\tau_w$is used as the pressure scale. $q_e = ½\rho U_e^2$ was also explored as a pressure scale; although, Goody (1999) found that it provided a poor collapse of the smooth wall pressure spectra. Each of these time scales was implemented for the current rough wall measured pressure spectra on both τ_w, and q_e; however only the timescales that were either the most prevalent in literature or provided the most complete collapse will be reviewed further. Aupperle and Lambert's data will not be included in the outer scaling analysis because their data does not contain a low frequency maximum.

Two of the most common outer scalings, which attempt to collapse the low frequency pressure spectra, are the classical outer scaling and the mixed outer scaling. The classical outer scaling takes the spectral density $\Phi(\omega)$ and frequency ω and normalizes it on the wall shear stress τ_w, boundary layer thickness δ and friction velocity u_τ as $\Phi(\omega)u_\tau/(\tau_w^2\delta)\ vs.\ \omega\delta/u_\tau$. This scaling was applied to Forest's (2012) smooth and 3-mm rough wall data sets as well as the present study's data as seen in Figure 41 (a), and the pressure spectra collapses to a single curve for frequencies up to about $\omega\delta/u_\tau = 250$ with a deviation of ±1.3dB for all cases. Figure 41 (b) shows the same data, but with Blake (1970) and Varano's (2010) rough wall results added. Figure 41 (b) does not appear to produce a good collapse of the pressure spectra, due to the scatter produced by Varano's data, which sits above all other data sets. However, this result was to be expected, since Varano (2010) states that he was not able to achieve a complete collapse of his pressure spectra when analyzing any outer scalings. Varano (2010) attributed this to the possibility of merging boundary layers from the tunnel floor and ceiling. Blake (1970) also notes a significant tunnel disturbance in his low frequencies, and cites a +/- 13% statistical error at 100 Hz for his low frequency pressure levels, which may affect the low frequency scaling for his data. Also facility dependence of the studies is likely reflected in the collapse of the low frequency pressure spectra due to such large scales.

A variation of the classical outer scaling takes the form $\Phi(\omega)U_e/(\tau_w^2\delta)\ vs.\ \omega\delta/U_e$ and is applied to the data in Figure 42. Figure 42 (a) presents Forest's (2012) smooth wall and 3-mm rough wall data sets as well as the present study's data. The wall pressure spectrum collapses to a single curve for frequencies up to about $\omega\delta/U_e = 25$ with a deviation of ±1.3dB for all cases. Figure 42 (b) adds Blake (1970) and Varano's (2010) rough wall results, and this scaling, like the classical outer scaling, does not appear to produce a good collapse of the pressure spectra due to the scatter of Varano's data. It is important to note though that the collapse in Figure 42 looks almost graphically identical to the results depicted for the classical outer scaling shown in Figure 41.

The mixed outer scaling was then analyzed, and this scaling uses the displacement thickness δ^* and the edge velocity U_e to scale the low frequency pressure spectrum as $\Phi(\omega)U_e/(\tau_w^2\delta^*)\ vs.\ \omega\delta^*/U_e$. This scaling was applied to Forest's (2012) smooth wall and 3-mm rough wall data sets and that of the present study seen in Figure 43 (a). Figure 43 (a) shows that the pressure spectra for all cases collapse to a single curve with a deviation of ±1.5dB for frequencies up to about $\omega\delta^*/U_e = 3$. Figure 43 (b), shows the same data, but with Blake (1971) and Varano's (2010) rough wall results added. Note that Blake's pressure spectra matches the data obtained from Figure 5 in Blake (1970) for this scaling only, and does not match the rest of Blake's data presented in this analysis as described previously at the beginning of this section. This is because Figure 5 was used to obtain Blake's pressure spectra for this case only to insure an exact match of figures. With this in mind, the mixed outer scaling produces a slightly worse correlation of the low frequency pressure spectra for all data sets as compared to the classical outer scaling due to Blake (1970) and Varano's (2010) data, which may contain some low frequency contamination.

A better collapse of the rough wall data only can be seen in Figure 44 using the scaling $\phi(\omega)U_e/q_e^2\delta$ vs. $\omega\delta/U_e$ where $q_e = ½\rho U_e^2$. Figure 44 (a) shows the same level of collapse as the classical outer scaling for the rough wall cases of Forest (2012) and the present study, but Forest's smooth wall data sits about 8dB below that of the rough wall data. When Varano (2010) and Blake's (1970) data is added in Figure 44 (b), a fairly decent correlation of all rough wall data sets including Varano's is seen for the low frequency pressure spectra to within ±5dB. However, this investigation would argue that it would seem that the true low-frequency pressure spectra scaling should unify both smooth and rough walls, and that Varano's (2010) data may have in fact been impacted, as Varano claims, by the merging boundary layers of the tunnel floor and ceiling.

At this point though if we exclude Varano's (2010) data, all we can conclude is that the classical outer scaling and the outer scaling based on δ, U_e, and τ_w are likely viable methods for scaling the low frequency range of the wall pressure spectra for both smooth and rough wall turbulent boundary layers. Although it seems that the outer region scaling should likely be controlled by global boundary layer parameters such as the edge velocity U_e and boundary layer thickness δ. This is because as Goody (2004) argues, the largest coherent structures are of the order δ and not δ^*, and the ratio of $\delta^*/\ \delta$ approaches zero as the Reynolds number approaches infinity, meaning that δ and δ^* are not equivalent outer length scales. Varano (2010) also cites that Bradshaw (1967) describes the behavior of the fluctuating pressure at a given frequency as $U_c/2*\pi y$ where y is the distance from the wall to the location of the turbulence structure and U_c is the wave speed. Varano (2010) then reasons that this should mean that at low frequencies the spectral density should not depend on the motions happening near the wall, but instead on the global boundary layer parameters U_e and δ.

The so-called 'inner scaling' for the rough wall data will now be examined. Blake (1970) first argued that the pressure fluctuations generated from the inner portion of the boundary layer should scale as $\Phi(\omega)u_\tau/(\tau_w^2 k_g)\ vs.\ \omega k_g/u_\tau$ at high frequency, where u_τ is the friction velocity and k_g is the geometric roughness size. It is interesting to note that the frequency scale $\omega k_g/u_\tau$ is essentially the roughness Strouhal number. Aupperle and Lambert (1970) then considered a similar scaling of the form $\Phi(\omega)/(\tau_w{}^2 k_s\ C_f\ )$ vs. $\omega k_s/u_\tau$, to not only account for the roughness height, but also the roughness sparseness as well. At

this point though, it can be argued that Blake and Aupperle and Lambert's scalings should perhaps be more appropriately referred to as mid-frequency scalings, since neither contains any reference to viscosity, which even in a rough wall flow must ultimately control the smallest turbulent scales and thus the highest frequency pressure fluctuations.

Figure 45 (a) depicts Blake's scaling using data from Forest (2012) and the present study. Blake's scaling clearly does not collapse the highest frequency portions of the pressure spectra as can be seen from the variations across test speeds and configurations. However, a definitive collapse can be found in the mid frequencies $4 < \frac{\omega k_g}{u_\tau} < 20$ that has a constant slope of about -4/3. Figure 45 (b) goes on to show the same trend with the added studies of Blake (1970), Aupperle and Lambert (1970) and Varano (2010), although the collapse of the data is not as complete, and Varano's (2010) data contributes to most of the scatter. It is important to note at this point that only Grade 36 of Aupperle and Lambert's (1971) data, and the data from Forest (2012) and the present study meet Jimenez's criterion to be considered within the fully rough regimes, which may contribute to the effectiveness of these scalings as will be discussed in Section 3.4.5.

Similar results can also be seen with the modification of Blake's scaling using k_s instead of k_g, applied to data from Forest (2012) and the present study in Figure 46 (a); however, when this scaling is applied to all the data sets in Figure 46 (b) a less convincing collapse is achieved. Aupperle and Lambert's scaling is then shown in Figure 47 (a) and depicts a comparable mid-frequency correlation for data from Forest (2012) and the present study, but when the studies of Blake (1970), Aupperle and Lambert (1970) and Varano (2010) are included in Figure 47 (b) it becomes apparent that this scaling is the least effective in collapsing the mid-frequencies. Focusing on just the present data and that of Forest (2012), which combines the largest roughness Reynolds numbers, and largest boundary layer thickness to roughness size ratios, the collapse is particularly good, and to within about ±1.5dB for all three scalings (Figures 46,47, and 48) within the mid-frequency range defined above.

Recently Varano (2010) proposed another so-called inner variable scaling. Starting with Blake's scaling, Varano explained that for fully rough flows the friction velocity should be proportional to the edge velocity. If replaced, the scaling $\Phi(\omega)/(\rho^2 U_e^3 k_g)\ vs.\ \omega k_g/U_e$ is obtained. Varano's scaling is applied to the pressure spectra of Forest (2012) and the present study in Figure 48 (a), and Blake's (1970) and Varano's (2010) data are added in Figure 48 (b). The results shown in Figure 48 (b) appear to be an improvement upon Blake's original scaling. Like Blake's scaling Varano's scaling fails at the highest frequencies, but does tend to correlate the mid-frequency pressure fluctuations quite well. Comparing Blake's scaling shown in Figure 45 with Varano's scaling shown in Figure 48, it can be seen that Varano's scaling produces a tighter collapse of Varano's (2010) data only. The spread of the data from Blake (1970), Forest (2012), and the present study essentially remains the same between the two scaling methods with a deviation of about ±2.5dB.

In an attempt to include some viscous scaling at the highest frequencies, Forest (2012) postulated that a meshing of timescales was needed in order to scale the high frequency pressure spectra. The scaling ν/u_τ^2 is based in the viscous timescale for the wall bounded flow, whereas Blake's scaling k_g/u_τ reflects the time scale for the roughness elements. Forest (2012) argued that even for fully rough flows, both timescales may still influence the near wall turbulent structures. This led him to take the geometric average of both time

scales yielding a spectral scaling of the form $\Phi(\omega)u_\tau^2/[\tau_w^2\nu(k_g)^{0.5}]\ vs.\ \omega\nu(k_g)^{0.5}/u_\tau^2$, and since there is no *a priori* reason to choose the geometric roughness size k_g over the effective sand grain roughness k_s in this formulation, Forest (2012) also considered the form $\Phi(\omega)u_\tau^2/[\tau_w^2\nu(k_s)^{0.5}]\ vs.\ \omega\nu(k_s)^{0.5}/u_\tau^2$.

Figures 50 (a) and 51 (a), show Forest's (2012) proposed scaling using the above relations based on roughness height k_g and the effective sand grain height k_s respectively, applied to the data of Forest (2012) and the present study. Both figures look graphically identical and provide an improved high frequency collapse, at the highest frequencies. However, there still exists a discrepancy between the 1-mm and 3-mm roughness cases with spectra for the 1-mm case lying above the spectra for the 3-mm case at mid frequencies and below at high frequencies. Figures 50 (b) and 51 (b) again show the same plots but with data from the studies of Blake (1970) and Aupperle and Lambert (1970), and Varano (2010) added. These figures also show an improved collapse at high frequencies when compared to the scaling's of Blake (1970), Aupperle and Lambert (1991), or Varano (2010) in Figures 46, 47, 48, and 49. It is clear that both forms do fairly well in correlating across the different investigations except in the case of Varano's (2010) study. Varano's (2010) data fans out slightly when scaled on k_s as seen in Figure 50 (b), but when scaled with the roughness height k_g a much tighter collapse is produced. Even though the scaling is close using k_g, it is not perfect. Thus although Forest (2012) presents a compelling argument for inner roughness scaling and provides a tighter collapse of the high frequency pressure spectra, a more fundamental approach is pursued.

3.4.3 *A new scaling for the highest frequency pressure fluctuations*

From the above comparisons it is clear that none of the previously proposed scalings for rough wall boundary layers adequately describe the highest frequency portions of the rough wall pressure spectrum. Revisiting the mixed outer scaling normalized as $\omega\delta^*/\mathrm{U_e}$ in Figure 43, a progressive roll off of the rough wall high frequency spectra can be seen with varying Reynolds number, which qualitatively resembles the viscous behavior seen in the smooth wall data. Thus in an attempt to determine a truly universal high-frequency scaling, it becomes prudent to revisit the smooth wall viscous scaling $\Phi(\omega)u_\tau^2/(\tau_w^2\nu)\ vs.\ \omega\nu/u_\tau^2$ which is applied to the present rough wall data, and that of Forest (2012) in Figure 51 (a). Figure 51 (a) shows the high frequency pressure spectra rolling off at different points and levels in each case, with the 60 m/s data rolling off first for all configurations. Figure 51(b) further includes data from Blake (1970), Aupperle and Lambert (1971) and Varano (2010) and depicts the same type of trend. From this figure, it is clear that the smooth wall viscous scaling in its unmodified form does not come close to collapsing the highest frequency portion of the rough wall pressure spectrum. However it is important to note that the scaled data still exhibits some viscous-like behavior, which means that viscosity should ultimately play a role in the collapse of the high frequencies. This would suggest that a different form of the viscous inner scaling might be applicable on an adjusted friction velocity.

This hypothesis was explored further by attempting to find a modified viscous scaling velocity that would collapse all of the high frequency portions of the present and previously published surface pressure spectra. A scaling of the form $\Phi(\omega)u_\nu^2/(\tau_\nu^2\,\nu)\ vs.\ \omega\nu/u_\nu^2$ was suggested, where u_ν is a modified friction velocity and $\tau_\nu = u_\nu^2\ \rho$ is the corresponding wall

shear stress. Now for a smooth wall, the modified friction velocity u_ν is equal to the conventionally defined friction velocity. However, for a rough wall the value of u_ν was chosen so that the high-frequency portion of the normalized spectrum collapsed as close as possible to the smooth wall. This collapse is not guaranteed though, since the positioning of the scaled spectrum has two degrees of freedom, and there is only one adjustment parameter (the value of u_ν).

Nevertheless, it was found that the values of u_ν could be chosen to accurately collapse the high frequency portions of all the current rough wall pressure spectra and those of Forest (2012) on top of Forest's smooth wall spectra. Figure 52 (a) shows a high-frequency collapse of both the smooth and rough wall data to within a narrow band. Using the same method, values of u_ν were then determined for Varano's (2010) high frequency rough wall pressure spectra using Forest's smooth wall spectra as a reference. Figure 52 (b) also shows the data collapsing to a narrow band, which is about the same width as the collapse seen in Figure 52 (a). This scaling method was also investigated for the spectra of Blake (1971) and Aupperle and Lambert (1970), which again used Forest's (2012) smooth wall spectra as the reference, and is shown in Figure 52 (c). Figure 52 (c) depicts Blake (1971) and Aupperle and Lambert's (1970) spectra collapsing to Forest's smooth wall data at high-frequencies with only minor variations.

Finally Figure 53 displays all of the high frequency pressure spectra from the investigations plotted using the scaling $\Phi(\omega)u_\nu^2/(\tau_\nu^2\,\nu)\ vs.\ \omega\nu/u_\nu^2$. It is clear that by varying only one parameter, the viscous friction velocity u_ν, the high frequency pressure spectra collapse to a narrow band just a few dB wide with a slope of about -5 across the surface conditions from each study.

Table 8: List of viscous friction velocities used to scale data from Blake (1970), Aupperle and Lambert (1970), Varano (2010), Forest (2012), and the present study

	Speed (m/s)	Surface	k_g (m)	u_τ (m/s)	u_ν (m/s) (from spectral fit)	u_ν / u_τ
Blake 1970	38	D-L	0.0023	2.14	1.12	0.54
	50	D-L	0.0023	2.83	1.47	0.52
	38	S-S	0.0014	1.95	1.37	0.70
	50	S-S	0.0014	2.58	1.75	0.68
	38	D-S	0.0014	1.91	1.15	0.60
	50	D-S	0.0014	2.53	1.47	0.58
A&L 1970	50	Grade 36	0.0038	3.7	1.48	0.40
	50	Grade 12	0.0017	4.32	2.07	0.48
	50	Grade 4	0.0005	5.12	2.56	0.50
Varano 2010	27.4	Case 3	0.001	1.13	0.90	0.80
	20.5	Case 4	0.001	0.86	0.73	0.85
	27.1	Case 5	0.001	1.21	1.00	0.83
	19.6	Case 6	0.001	0.86	0.80	0.93
	27.5	Case 7	0.001	1.22	0.98	0.80
	20.2	Case 8	0.001	0.86	0.79	0.92
	27.2	Case 9	0.001	1.07	1.00	0.93
	20.4	Case 10	0.001	0.82	0.78	0.95
Forest 2012	20	3 mm	0.003	1.01	0.68	0.67
	30	3 mm	0.003	1.5	0.96	0.64
	40	3 mm	0.003	1.98	1.22	0.62
	50	3 mm	0.003	2.45	1.47	0.6
	60	3 mm	0.003	2.9	1.68	0.58
Present Study	20	1 mm	0.001	1	0.75	0.75
	30	1 mm	0.001	1.48	1.07	0.72
	40	1 mm	0.001	1.94	1.36	0.7
	50	1 mm	0.001	2.4	1.63	0.68
	60	1 mm	0.001	2.84	1.88	0.66
	20	3 mm	0.003	1.02	0.67	0.66
	30	3 mm	0.003	1.51	0.97	0.64
	40	3 mm	0.003	1.99	1.23	0.62
	50	3 mm	0.003	2.45	1.47	0.6
	60	3 mm	0.003	2.9	1.68	0.58

The values of u_ν used to collapse the rough wall pressure spectra are listed in Table 8. The ratio of the viscous friction velocity u_ν to the conventional friction velocity u_τ was also explored and plotted against various rough wall parameters in order to determine if any trends existed. The ratio u_ν/u_τ was found to exhibit a consistent trend when plotted against the roughness Reynolds number k_g^+, for all analyzed data sets as seen in Figure 54. From this figure, we see that for all the rough surfaces u_ν / u_τ is less than 1, and this ratio appears to decrease consistently with increasing k_g^+.

3.4.4 *Physical Interpretation of the Viscous Friction Velocity*

One argument for the viscous friction velocity is that viscous scales contributing to the pressure fluctuations at the wall, at locations not influenced by the local effects of the roughness elements, scale like those of a smooth wall boundary layer $\omega\nu/u_\tau^2$ but with a friction velocity calculated without the contribution from the pressure drag on the roughness elements. Following this, Yang and Wang (2009) state that the unsteady drag on a roughness element can be separated into the contribution from the form drag plus the

contribution from the viscous drag. The viscous friction velocity u_ν would then be a fraction of the friction velocity u_τ, this fraction decreases with roughness Reynolds number for each roughness configuration. In the case of the smooth wall, no pressure drag exists due to roughness elements, and thus u_ν equals the friction velocity u_τ. All of the viscous friction velocities listed in Table 8 are less than that of the friction velocity, which holds to this physical interpretation.

Beginning with this interpretation, it is possible to independently estimate the ratio of u_ν/u_τ from the sparseness ratio and the drag coefficient of the roughness elements for a fully rough flow. Ignoring pressure and momentum flux changes in the spanwise direction the overall average wall shear stress τ_w can be broken down into the average drag force on the individual roughness elements D, and the averaged substrate (or 'viscous') wall shear stress τ_ν, which excludes the element drag:

$$\frac{\tau_w}{\rho} = u_\tau^2 = \frac{\tau_\nu}{\rho} + \frac{n\,D}{\rho} \qquad \text{Equation 12}$$

In this equation n is the number of roughness elements per unit planform surface area. It is then assumed that a particular roughness element can be usefully thought of as having a fixed drag coefficient C_D

$$C_D = \frac{\mathrm{D}}{\bar{q}\,A} \qquad \text{Equation 13}$$

Here A is the frontal projected area of the roughness element. Schlichting (1979) argues that a drag coefficient can defined for a single roughness element, regardless of shape, if the sparseness ratio λ is less than or approximately equal to 0.15. Substituting Equation 13 into Equation 12 and substituting in the sparseness ratio $\lambda = n\,A$ and the viscous friction velocity $u_\nu = \sqrt{\tau_\nu/\rho}$ we obtain

$$u_\tau^2 = u_\nu^2 + \lambda\, C_D \left(\frac{\bar{q}}{\rho}\right) \qquad \text{Equation 14}$$

Note that in the case of the smooth wall Equation 14 simplifies to $u_\tau^2 = u_\nu^2$, since there are no roughness effects to account for.

To test this interpretation the dynamic pressure $\bar{q}$ is estimated following Schlichting (1979) by integrating the near-wall form of the mean velocity profile over the roughness height approximated as:

$$\bar{q} = \frac{1}{k_g}\,\frac{1}{2}\,\rho\,U_e^2 \int_0^{k_g} \left(\frac{z}{\delta}\right)^{\frac{2}{7}} dz = \frac{7}{18}\rho U_e^2 \left(\frac{k_g}{\delta}\right)^{2/7} \qquad \text{Equation 15}$$

The viscous friction velocity u_ν was calculated using the estimation given in Equation 14 for the measured data from Forest (2012) and the present study, for which the sparseness ratio λ remained below 0.15, and thus met the criteria for C_D to be taken as a fixed constant. It was then found that a single drag coefficient of $C_D = 0.26$ could be used to represent the hemispherical roughness elements of the 1-mm and both 3-mm rough surface conditions in the approximation of u_ν using Equation 15.

Initially the drag coefficient of $C_D = 0.26$ was chosen because this value produced the best approximation of u_ν, however the accuracy of this value as it pertains to the hemispherical roughness elements of this study still needed to be explored. Bennington (2004) measured the drag coefficients for single roughness elements under a two-dimensional high Reynolds number flow, and among the elements Bennington (2004) explored was a 1.397mm hemispherical roughness element. The total change in drag

ΔD_{E_actual}, caused by the addition of this element to the surface was measured under the following flow parameters: $U_e = 27.5$ m/s, $u_\tau = 0.95$ m/s, and $\delta = 39.3$ mm, and was normalized as $\Delta D_{E\_actual}/(\rho\ u_\tau\ A_f)$ equaling 37.70. This value then had to be converted into Schlichting's (1979) definition of the drag coefficient given in Equation 13 where $\bar{q}$ is defined in Equation 15. The result is a drag coefficient of $C_D = 0.30$, which is not outside the realm of possibility given the uncertainty of the measurements and the fact that the drag coefficient for a fetch of roughness elements should be slightly lower than that of a single roughness element due to the elements of the fetch sheltering one another from the flow.

The estimates for u_v of the present investigation and that of Forest (2012) found using Equation 14 are shown in Figure 55 and are plotted against the values derived from the pressure spectra, which were previously seen in Figure 54. The estimated ratios u_v / u_τ, are within an average of 2.5 percent of the actual ratios used in the viscous inner scaling to collapse the pressure spectra of Forest (2012) and the present study. The accuracy seen in Figure 55 of these estimates compared to the actual values used with such a basic model would appear to support the interpretation of the scaling parameter u_v.

Returning back to Figure 54, the results presented would tend to be expected given the physical interpretation above, since a decrease in the sparseness ratio would tend toward a smooth wall, which means that the ratio of friction velocities should also tend toward that of a smooth wall. It is also interesting to note that as the ratio decreases with increasing roughness Reynolds number the results tend to fall along the same curve for like sparseness ratios. That is to say, if one were to start at the smooth wall case with a ratio equal to one and interpolate through the given data points as the roughness Reynolds number increases all of the data points would sit along a single curve for that specific sparseness ratio.

3.4.5 *Triple Scaling Hypothesis*

After reviewing all of the previous scaling types, it becomes clear that the low frequencies of the wall pressure spectrum for each of the studies reviewed can best be correlated by the classical or mixed outer scaling for both smooth and rough walls as is shown in Figures 43 and 45. This is because the low frequency pressure fluctuations should be determined by the overall scales of the boundary layer. In addition, the high frequencies can also be correlated by the newly proposed viscous inner scaling for each of the studies reviewed, regardless of surface condition, as is seen in Figure 53. This tends to make sense because like the smooth wall, the rough wall high frequency pressure fluctuations must ultimately be constrained by viscosity.

Now it is clear from Figures 42 and 53 that the mid-frequencies still remain uncorrelated. Thus this study proposes a triple scaling hypothesis where a third scaling is needed to completely describe the fully rough wall pressure spectrum. The added scaling would correlate the mid-frequencies based upon the roughness parameters such as is the case with Blake's (1970) scaling and it's variants as seen in Figures 45 through 48. Initially it would appear that each of these scalings provides some measure of collapse of the data, however the argument becomes much more definitive if the data is restricted to the present study's results, which combine the largest roughness Reynolds numbers and largest boundary layer thickness to roughness size ratios. This is because the mid-frequency region develops and becomes more prominent as you move into the fully rough regime. Transitionally rough flows such as Blake (1970) and Varano's (2010) should only

collapse to a small point if at all, whereas the current study and that of Forest (2012) should collapse more of a curve. If the roughness Reynolds number is large enough and the rough surface can be defined by a single lengthscale, then it should be expected that there will be an intermediate region where pressure fluctuations are primarily produced by turbulence shed from the roughness elements and will scale, as Blake predicted, on the roughness element size and the effective flow velocity that the roughness elements experience. It is important to note that at this point it is still unknown as to why the pressure fluctuations collapse to a linear -4/3 slope.

Physically though this means that the rough surfaces analyzed had a sufficiently large separation between length scales i.e. the boundary layer thickness was sufficiently larger than the roughness which was sufficiently larger than the viscous scales. Taking this one step further, it would seem that if the roughness had more than one scale, such as tiny hemispheres covering a hemispherical roughness element, and these scales had sufficient separation with an effective Reynolds number of the miniature roughness elements remaining large, then there would be four scaling regions, with the two central regions defined by the two sets of roughness scales. The implication of this finding is that for many practical rough surfaces, particularly stochastic surface shapes, with a large range of poorly separated scales, the higher frequencies may overlap with the viscous dissipation, and therefore such boundary layers may have no universal surface pressure scaling, regardless of Reynolds number.

3.4.6 *Empirical Spectral Model of Surface Pressure Fluctuations*

An empirical model of the surface pressure fluctuations was developed for both smooth and rough walls based on Goody's (2004) model. Goody's model uses a simple function of the ratio of timescales of the outer to inner boundary layer, and is also able to incorporate the effect of Reynolds number through this timescale ratio. This model was chosen as the basis for the current model due to its functional form, and its ability to describe essential features of the frequency spectrum with limited degrees of freedom as is described by Goody (2004).

Goody (2004) based his model on the Chase and Howe model, and modified it to agree better with experimental data by incorporating a term in the denominator to achieve a spectral decay of ω^{-5} as ω approaches infinity, adding a multiplicative constant, and altering the exponents of the denominator. This resulted in the empirical model shown in Equation 16:

$$\frac{\Phi(\omega)\, U_e}{\tau_w^2 \delta} = \frac{C_2(\omega\delta/U_e)^2}{[(\omega\delta/U_e)^{0.75}+C_1]^{3.7}+[C_3(\omega\delta/U_e)]^7} \qquad \text{Equation 16}$$

where C_1, C_2, and C_3 are determined by several postulates, and the ratio of C_1 to C_3 describes the width of the-mid frequencies. Goody's first postulate states that the pressure spectrum must collapse to a universal curve, independent of Reynolds number, at low frequencies when normalized on τ_w as the pressure scale and δ/U_e as the timescale. Goody uses the boundary layer thickness instead of the displacement thickness because he reasons that the largest coherent structures are of order δ and the ratio of δ^*/δ approaches zero as the Reynolds number approaches infinity, thus the displacement thickness and boundary layer thickness are not equivalent as outer-layer length scales. Goody' second postulate states that the pressure spectra must collapse, independent of Reynolds number, to a universal

curve at high frequencies when normalized on τ_w, as the pressure scale and ν / u_τ as the timescale. Goody's third and final postulate is that the only effect of the Reynolds number on the shape of the pressure spectrum is to increase the size of the overlap range.

From the first postulate, C_1 and C_2 are determined as C_1=0.5 and C_2=3. Using the second postulate Goody developed a ratio to approximate the outer-layer to inner-layer timescale as: $(\delta/U_e)/ (\nu/u_\tau) = u_\tau^2\delta/ (U_e\ \nu) \equiv R_T$. R_T therefore accounts for Reynolds number effects. Goody (2004) then set the model parameters as C_1=0.5, C_2=3 and C_3=1.1$R_T^{-0.57}$. In this form Equation 16 results in an increase of the lowest frequencies as ω^2 with the mid-frequencies decaying as $\omega^{-0.7}$ and the highest frequencies dropping off as ω^{-5}. Goody (2006) found excellent agreement with all of the studies he reviewed.

In order to determine the current empirical spectrum model, we return to Goody's first postulate. As we saw in Figure 41 the pressure spectrum of both smooth and rough walls collapses to a universal curve, independent of Reynolds number, at low frequencies when normalized on τ_w as the pressure scale and δ/U_e as the timescale. This allows us to use the general form of Goody's Model. However, as we saw in Figure 45 (a) the fully rough surface pressure spectrum collapses to a single curve in the mid-frequencies when normalized on τ_w as the pressure scale and k_g/u_τ as the timescale. This leads us to deviate from Goody's model and we will add an extra term in the denominator to account for the mid-frequencies as seen in Equation 17. Note that the length of this region will also be Reynolds number dependent. Finally the high frequencies must collapse to a universal curve based on the viscous inner scaling as shown in Figure 53. The viscous inner scaling uses τ_v, as the pressure scale instead of τ_w and $\nu/u_v^{\ 2}$ as the timescale instead of ν/u_τ, this is slightly different than Goody's model and will have to be accounted for. As with Goody (2004) the only effect of Reynolds number accounted for is to increase the size of the region. Following this we obtain Equation 17:

$$\frac{\Phi(\omega)\, U_e}{\tau_w^2 \delta} = \frac{C_2(\omega\delta/U_e)^2}{[(\omega\delta/U_e)^{0.78}+C_1]^{3.7}+[C_3(\omega\delta/U_e)]^{3.7}+[C_4(\omega\delta/U_e)]^7} \qquad \text{Equation 17}$$

Note that all of the exponents with the exception of one, which changes slightly in order to better fit the current study, remain the same. Also remaining consistent with Goody's first postulate, C_1 and C_2 remain as C_1=0.5 and C_2=3. This means that the lowest frequencies still follow as ω^2 along with the highest frequencies dropping off as ω^{-5}, which is how each of the exponents were determined. The mid-frequency decay however, will vary with Reynolds number. C_3 and C_4 will be derived in much the same way as was discussed by Goody (2006). Following the second postulate a ratio of the outer-layer to mid-layer timescales can be developed: $(\delta/U_e)/ (k_g/u_\tau) = \delta\ u_\tau/ (k_g\ U_e) \equiv R_{T1.}$ The same can be achieved for the mid-layer to inner-layer timescales, but the difference in the pressure scale of τ_w and τ_v will have to be resolved. Therefore leads us to: $((\delta/U_e)/ (\nu /u_v^{\ 2}))*(\tau_v / \tau_w)^{0.5} \equiv R_{T2.}$ The $(\tau_v / \tau_w)^{0.5}$ term accounts for the difference in the two pressure scales. Consequently, C_3 and C_4 will take the same form as in Goody's model with C_3=1.1$R_{T1}^{-0.57}$ and C_4 =1.1$R_{T2}^{-0.57}$. In the case of the smooth wall C_3 drops out since k_g = 0, and we recover Goody's (2004) original empirical model, because $u_v = u_\tau$ and $\tau_v = \tau_w$.

At this point it is important to note that with an empirical model type such as this, low frequency contamination by the facilities becomes of concern when applying measured spectra. As was stated previously, this study and that of Forest (2012) used an acoustically

quiet wind tunnel, and no low contamination is expected in the measured pressure spectra. Also of note, the high frequency data for this study as well as Forest (2012) may contain some microphone attenuation at the very highest frequencies. This attenuation, however, was expected to be minimal based on the sizing of the pinhole caps on the microphone, which were evaluated using Gravente *et al.'s* (1998) guidelines. Although in future work, Corcos's (1963) table will be used to account for any microphone attenuation, and the portion of this studies high frequency model will be adjusted, if needed, accordingly.

The proposed empirical model in Equation 17 was then applied to the present study and that of Forest (2012) using the parameters listed in Tables 8, 9, and 10 as inputs, and can be seen in Figure 56. Figure 56 depicts the empirical predictions (shown in blue) overlaid on top of the measured pressure spectra (shown in black) at each test speed and at each of the microphone locations given in Table 3. After reviewing Figure 56, it quickly becomes apparent that this model captures almost all of the essential features of the pressure spectra for each of the surface conditions at each test speed. However, some discrepancy is observed at the highest frequencies. Further investigation is needed to determine if this is the result of the limitations of the instrumentation or the result of the physical aspects of the measured pressure spectra. Also of note, some slight discrepancy exists between the model and Forest's (2010) 3-mm ordered rough surface pressure spectra at the highest test speeds of 50 and 60 m/s. This is due to an unexplainable rise in the measured pressure spectra between the mid and low frequencies, which is not seen in any of the other measured pressure spectra.

The empirical model in Equation 17 was then extended to include the transitionally rough wall data from Blake(1970) and Varano (2010) respectively. It is important to note that both of these data sets are suspected to contain low frequency contamination as stated previously. Using the parameters listed in Tables 8, 9, and 10 for Blake's (1970) data, the proposed empirical model in Equation 17 produces the results seen in Figure 57 where the empirical predictions (shown in blue) are overlaid on top of the measured pressure spectra (shown in black) for each of Blake's surface conditions and test speeds. Figure 57 does not show good agreement in the low and mid frequencies of the proposed spectral model and Blake's measured pressure spectra. However, it does appear that the spectral model shows the correct low frequency magnitude, but shifted to lower frequencies by about a factor of 2 as compared to Blake's (1970) measured spectra shown here obtained from Figure 12 in Blake (1971). Note that if ω in Blake's measured pressure spectra shown here is divided by 2, it will yield the unscaled pressure spectra obtained from Figure 5 in Blake (1970) as per the previous discussion in Section 3.4.2. This would then provide a fair agreement between the spectra model and measured pressure spectra with slight discrepancies in the low frequencies, which are thought to be due to an over correction of the noise contamination and the +/- 13% statistical error at 100 Hz that Blake (1970) cites for his low frequency pressure levels. Figure 57 shows that the highest frequencies are in good agreement between the proposed spectral model and Blake's measured spectra from Figure 12 in Blake (1971). If we were to use the data obtained from Figure 5 in Blake (1970), the viscous friction velocity values would be smaller and a good agreement would still be achieved between the two models.

Figure 58 shows the proposed empirical model in Equation 17 applied to data from Varano (2010) using the parameters listed in Tables 8, 9, and 10 as inputs. Figure 58 depicts the empirical predictions (shown in blue) overlaid on top of the measured pressure

spectra (shown in black) for each of Varano's cases and test speeds. Figure 58 shows good agreement in the highest frequencies between the empirical model and the actual measured spectra. However the empirical model and Varano's measured data begin to deviate notably as the comparison shifts towards the low frequencies. As we discussed previously, Varano's data may contain some low frequency contamination, which he attributed to the possibility of the merging of the boundary layer of the floor and ceiling. If this is indeed the case the mid-frequencies would also be affected to some extent causing discrepancies between the proposed model and Varano's measured pressure spectra. Varano's (2010) measured data also appears to contain a knee in the transition between the mid and high frequencies of the pressure spectra, which may be physical or may be due to the instrumentation though it is hard to tell.

Overall the proposed empirical model given in Equation 17 describes the essential features of the pressure spectrum of each of the surface conditions and test speeds for the current study and that of Forest (2012). Blake's (1970) data may or may not agree with the proposed spectral model depending on which of his figures provides the correct data set, and Varano's (2010) data deviates in the low and mid frequencies, but matches the empirical model in the highest frequencies. It is acknowledged that this model will require further refinement; however it will most likely resemble something of this form. This is the first time to the author's knowledge that an empirical model has attempted to encompass fully rough, transitionally rough and hydraulically smooth wall flows.

3.5 Two Point Pressure Fluctuation Measurements

This investigation will now turn its attention to the analysis of the two point microphone data, specifically the coherence correlation, phase, and phase convection velocity for the 1-mm ordered and 3-mm random rough surface conditions. These results will then be compared to the results of Forest's (2012) smooth wall and 3-mm ordered rough surface conditions in order to obtain a better understanding of the effects of surface roughness on the turbulent eddies within the boundary layer. Note that Forest's (2012) smooth wall data will be presented at 33.6 m/s and 67.2 m/s, while the rest of this studies data and Forest's (2012) 3-mm ordered rough wall data will be presented at 30 and 60 m/s.

3.5.1 Coherence

The wall pressure spectrum coherence Γ^2, was determined at 30 and 60 m/s for the 1-mm ordered and 3-mm random rough surface conditions using Equation 1, where $\phi_{p_i p_j}$ is the wall pressure cross-spectrum between microphone locations *i* and *j*.

$$\Gamma^2 = \frac{\left|\phi^2_{p_i p_j}\right|}{\left|\phi_{p_i p_i}\right|\left|\phi_{p_j p_j}\right|} \qquad \text{Equation 18}$$

The coherence is mapped against the frequency ω for the streamwise ξ and spanwise η separations, which is normalized as ξ/δ^* *vs.* $\omega\delta^*/U_e$ and η/δ^* *vs.* $\omega\delta^*/U_e$ respectively. The different microphone separations are represented as tick marks on the right-hand side of the figures discussed below and the data between these separations has been interpolated. It is important to note that the subtle disjoints that appear as a thin line across some of the

coherence figures at certain separation locations stem from averaging and interpolating multiple coherence measurements of the same separation location. This was done in order to combine all separations onto one coherence plot, due to the incomplete microphone array as mentioned earlier. These subtle disjoints also yield some indication of the uncertainty of the measurements, since each measurement should essentially yield the same result, and thus when averaged continue to exhibit a smooth transition across separations.

Figure 59 and Figure 60 show the streamwise spectral coherence progression for a) Forest's (2012) smooth wall, b) the ordered 1-mm roughness, c) the random 3-mm roughness, and d) Forest's (2012) ordered 3-mm roughness for 30 and 60 m/s respectively. A quick comparison of these figures shows that the coherence increases as the frequency decreases for all cases. Since the lower frequencies are attributed to the outer portion of the boundary layer, this means that the larger turbulent eddies contained within this region have a greater persistence over larger distances as compared to the lower coherence values of much smaller eddies associated with the higher frequencies that decorrelate a lot quicker over smaller distances. This result matches the findings of Bull (1967).

The ordered 1-mm roughness appears to be slightly less correlated than the random 3-mm rough surface condition for smaller separations between $-4 \leq \xi/\delta^* \leq 4$. This might be due to an increase in mixing effects from the local turbulent shedding of the 1-mm roughness elements, since the elements are located much closer (about 2.75 mm) to the microphones than that of the random 3mm, which was spaced at least 10 mm away. It could also be the result of an increase of mixing just due to the decrease in element separation for the ordered 1-mm surface condition. The random 3-mm roughness was also compared to Forest's (2012) ordered 3-mm roughness, and for the same separation range, Forest's ordered 3-mm roughness exhibited smaller coherence values. It is again thought that this might be due to the local turbulent eddy shedding off of the roughness elements, due to Forest's (2012) ordered 3-mm roughness being spaced 8.25 mm away from the microphones, and the random 3-mm rough surface condition's closest element was at least 10mm away from the microphones.

Shifting to a comparison of the smooth wall versus the rough walls, the coherence between the smooth wall streamwise separations is greater than that of the rough wall surface conditions. This is thought to be due to the roughness elements generating interference and mixing, which in turn leads to a quicker decrease of the coherence between separations at each frequency as was stated by Forest (2012). Forest (2012) compared the smooth wall coherence results to the ordered 3-mm roughness, and found that coherence values of $\Gamma^2 > 0.2$ at $\omega\delta^*/U_e = 0.73$ only exist out to $4.1\delta^*$. Forest (2012) also found that for frequencies below $\omega\delta^*/U_e = 0.19$, the pressure spectra coherence rarely rises above $\Gamma^2 > 0.15$ at large separations of at least $21\delta^*$. These findings were also observed for the current studies ordered 1-mm and random 3-mm rough surface conditions. The similar values of the larger streamwise coherence for each normalized frequency and separation of the rough surface conditions is attributed to the fully rough requirements being met, which means that the roughness should have little effect on the outer regions low frequency eddies. This stands to reason since the rough surface conditions have a very similar low frequency pressure spectra as seen in Figure 39.

Figure 61 and Figure 62 show the spanwise spectral coherence progression for a) Forest's (2012) smooth wall, b) the ordered 1-mm roughness, c) the random 3-mm roughness, and d) Forest's (2012) ordered 3-mm roughness for 30 and 60 m/s respectively. Like the streamwise case, as the frequency decreases, the coherence tends to increase, but this is only true for a smaller range of separations as no significant coherence values exist beyond $4\delta^*$. It is clear that as the spanwise separations increase the coherence tends to rapidly decreases in all cases, which is to be expected, since there is no free stream flow in the spanwise direction to convect the turbulent eddies. This result would tend to confirm that the flow can in fact be considered 2-Dimensional.

3.5.2 Correlation

The wall pressure space-time correlation R_{pp} will now be explored for the 1-mm ordered and 3-mm random rough surface conditions. The results will be compared to Forest's (2012) smooth wall and ordered 3-mm rough wall data. The wall pressure space-time correlation can be seen in Figures 63 and 64 for Forest's (2012) smooth wall (a), the 1-mm ordered roughness (b), the 3-mm random roughness (c), and Forest's (2012) 3-mm ordered roughness at 30 and 60 m/s respectively. In these figures, the streamwise separations ξ are normalized as ξ / δ^*, vs. the time delay τ normalized as $\tau U_e/\delta^*$. Just as with the coherence, the correlation data between the actual microphone separations, shown as tick-marks, has been interpolated. The space-time correlation for these plots was determined using Equation 19, which defines the correlation between the pressure fluctuations at a location x and time t, and the pressure fluctuations at a separation $x+s$ and time $t+\tau$. For streamwise separations $x+s = \xi$ and for spanwise separations $x+s=\eta$.

$$R_{pp}(s,\tau) \equiv \langle p(x,t)p(x+s,t+\tau)\rangle \qquad \text{Equation 19}$$

The space-time correlations were assumed to be independent of x and t, since the boundary layer and associated turbulences were taken to be homogeneous. This assumption was made based on the two-dimensionality and limited boundary layer growth of the flow near the microphone array.

Figures 63 and 64 show that the convective ridge for Forest's (2012) smooth wall (a), the 1-mm ordered (b), the 3-mm random (c), and Forest's (2012) 3-mm ordered roughness at 30 and 60 m/s tend to have greater slopes for larger separations when compared to the smaller separations. In the figures this can be seen as the higher slope of the less correlated larger separations, which are shown in yellow as compared to the lower slope of the higher correlated smaller separations depicted in red. One explanation for this is that the smaller turbulent eddy structures are slower moving and thus dominate the pressure field over shorter distances, which was suggested by Bull (1967). As the turbulent eddies convect downstream they begin to decorrelate, which leads to the faster moving structures in the outer boundary layer to become dominant. It would appear that as the roughness size increases, the width of the coherence ridge for the smaller microphone separations increases as well. This would suggest, as Forest (2012) stated, that a wider range of eddy convections can be found over rough walls, and that only the inner boundary layer convection velocities are becoming mixed due to the presence of roughness, since the outer region maintains a similar ridge width for the largest separations for both smooth and rough walls.

Figure 65 and 66 depict the correlation for the spanwise separations of Forest's (2012) smooth wall (a), the 1-mm ordered (b), 3-mm random (c), and Forest's (2012) 3-mm ordered roughness (d) at 30 and 60 m/s respectively. As is seen in Figures 65 and 66, any spanwise space-time correlation appears to be independent of time, and the correlations that do exist are thought to have been the result of the occasional large eddy passing by as was suggested by Forest (2012). Thus very little correlation exists for the spanwise cases as compared to that of the streamwise. This is to be expected, since the flow is 2-dimensional. Note that the spanwise correlation for Forest's (2012) 3-mm ordered, 30 m/s case seen in Figure 65 (d) does not appear to follow the rest of the cases analyzed, and is probably the result of a malfunctioning microphone.

The correlation decay of the wall pressure space-time correlation was analyzed for Forest's (2012) smooth wall, the 1-mm ordered, 3-mm random, and Forest's (2012) 3-mm ordered roughness at each test speed. Figures 67, 68, 69, 70 show the space time-correlation R_{pp} for fixed streamwise separation distances normalized on the boundary layer thickness ξ/δ^* plotted as R_{pp}/P_{rms} *vs.* $\tau U_e/\delta^*$ where P_{rms} is the root mean square (R.M.S) pressure for the 1-mm ordered and 3-mm random roughness respectively. As with Forest (2012), the boundary layer displacement thickness changed by less than 6% between test speeds, and in order to plot each test speed on the same correlation decay figure, the ξ/δ^* term has been averaged for a given test speed. This value is the one given in the legend.

Figures 67, 68, 69, and 70 also show that the space-time correlation decay is not constant, and as the separation distances increase, the correlation is found to broaden and show a decrease in its peak. This result is consistent with the findings of Forest (2012). Blake (1970) argues that this is due to the decay of the slower moving smaller eddies leading to a predominance of the faster moving larger eddies.

In order to compare correlation decay envelopes the Lagrangian timescale T_L is found by integrating the decay of the pressure spectra with respect to time delay τ over the entire space-timescale. Figure 67 depicts the 1-mm roughness correlation decay, which follows the Lagrangian timescale $T_L = 5.0\delta^*/U_e$. Figure 68 shows the 3-mm random roughness correlation decay, and that decay follows a Lagrangian timescale of about $T_L = 5.3\ \delta^*/U_e$. Forest's (2012) smooth wall correlation decay can be found in Figure 69, and Forest lists the Lagrangian timescale as about $T_L = 5.8\delta^*/U_e$. Figure 70 a) then shows Forest's 3-mm ordered roughness, decaying with a Lagrangian timescale of about $T_L = 4.6\delta^*/U_e$ as calculated by Forest (2012). These decay envelopes are all compared in Figure 70 b), and show that the addition of the presence of roughness causes the decay rate to increase, which would tend to suggest that the decay rate is sped up by the increased turbulent mixing from the roughness elements. The reason the 3-mm random roughness does not share the same decay rate as Forest's 3-mm ordered roughness or show a greater decay rate than the 1-mm ordered roughness is thought to be due to the proximity of the microphones with respect to the roughness elements. That means that since the microphones were spaced farther away from the roughness elements for the 3-mm random roughness than the 1-mm ordered and Forest's 3-mm ordered roughness, the effects of the turbulent mixing on the decay rate are not seen as strongly.

3.5.3 Phase and Phase Convection Velocity

The wall pressure spectra phase angle for the 1-mm ordered and 3-mm random roughness was then determined by taking the cross spectra phase angle between the different microphone locations. The result, shown in radians in the following figures, is depicted as a function of angular frequency ω normalized as $\omega\delta^*/U_e$ for streamwise and spanwise separation phase angles.

Figures 71 and 72 show the phase angle for Forest's (2012) smooth wall (a), the 1-mm ordered (b), 3-mm random (c), and Forest's (2012) 3-mm ordered roughness at 30 and 60 m/s respectively for the different streamwise separations ξ/δ^*. Both figures show an increasing phase with increasing streamwise separation, as well as a phase dependence on frequency along the fixed separation lines. This frequency dependence is due to the segregation of the turbulent eddy structures by size throughout the boundary layer. It was observed in the Figures 59 and 60 that there was a coherence loss across all frequencies for increasing separations, with the high frequencies seeing the most rapid decline. This coupled with the phase angle fixed-separation lines depicting a more rapid increase in phase with increasing frequency would suggest that for similarly sized turbulent eddies, those moving faster and tending towards the outer portions of the boundary layer would be the first to decorrelate, while similarly sized eddies moving slower would tend to be more stable. The rough wall pressure spectra phase does in some cases however, exhibit a slightly negative phase angle at low frequencies for the smallest separation distance $0.20\delta^*$. Forest (2012) suggests that this result may be due to a form sort of vortex shedding off of the local roughness elements, since it is not seen for the larger separations. Also, the phase angles of each surface condition at 30 and 60 m/s shown in Figures 71 and 72 respectively are graphically identical for the smaller to mid-sized separations, except for the slightly negative phase present in the rough wall cases at the smallest separation, which would imply this is an effective scaling of the phase angles.

The phase angles for spanwise separations η were evaluated between $0.2\delta^*$ and $22.3\delta^*$ for the 1-mm ordered and 3-mm random rough surface cases. Figures 73 and 74 show the phase angle for Forest's (2012) smooth wall (a), the 1-mm ordered (b), 3-mm random (c), and Forest's (2012) 3-mm ordered roughness at 30 and 60 m/s respectively for the different spanwise separations η/δ^*. Since the flow is 2-dimensional, the larger phase angles contain no significant data and were not presented in Figures 73 and 74. Forest's (2012) smooth wall data (a) shows small separation lines represented only at the higher frequencies, however, he attributes this to the occasional large turbulent eddy affecting multiple spanwise locations, which is supported by the fact that there is essentially no phase or meaningful coherence data present for separations larger than $5.09\delta^*$. Turning our attention to the rough wall data, a similar behavior is seen for all cases, but with a slightly elevated phase value at low frequencies. This is thought to be due to the more chaotic nature of the rough wall flow, as the increased boundary layer mixing due to surface roughness could cause some spanwise turbulent eddy drift across different spanwise locations.

The phase convection velocity U_{cp} was determined by taking the product of the separation distance s and angular frequency ω and dividing by the phase angle α as was described by Blake(1970). The resulting phase convection velocities were then plotted for the different normalized streamwise separation distances ξ/δ^* as U_{cp}/U_e *vs.* $\omega\delta^*/U_e$ for the 1-mm ordered (b) and 3-mm random (c) rough surface conditions and compared with the results of

Forest's smooth wall (a) and 3-mm ordered rough wall (d) at 30 and 60 m/s in Figures 75 and 76 respectively. From these two figures it appears that the phase convection velocities are somewhat dependent on the blockage ratio δ/k_g. As the blockage ratio decreases it appears that the phase convection velocity decreases as well. This is to be expected since it would make sense for the smooth wall to have the highest phase convection velocities due to the lack of obstacles within the boundary layer. It is also important to note that the 3-mm random (c) and Forest's (2012) 3-mm ordered rough surface yield very similar results at each test speed.

Further examination of Figures 75 and 76 shows that the phase convection velocity tends to increase slightly as the Reynolds number increases, which is more prominent in the smooth wall data. Finally the phase convection velocity shows a frequency dependence, where the phase convection velocity peaks between $\omega\delta^*/U_e = 0.1 - 0.4$, and tends to shift up and back in the figures as the streamwise separations increase. According to Morrison *et al.* (1992) this is indicative of the turbulent eddies forming within the boundary layer slowly moving away from the wall towards the outer, faster portions of the boundary layer. However as Forest (2012) pointed out for the rough wall conditions, the higher frequency shift reflects the delayed onset of the mid-frequency region of the wall pressure spectra shown in figures 34, 36 and 37 and is due to the roughness turbulent kinetic energy shift towards the wall.

CHAPTER 4. CONCLUSIONS

The wall pressure fluctuations were measured for high Reynolds number zero pressure gradient turbulent boundary layer flows in a streamwise and spanwise array over a smooth surface, 1-mm ordered hemispherical rough surface, and a 3-mm randomly spaced hemispherical rough surface in the Virginia Tech Stability Wind Tunnel under conditions defined by Jimenez (2004) to be within the fully rough regime. The boundary layer velocity profiles and the mean pressure along the wall were also measured. The results were then compared to similar boundary layer studies in order to determine the scaling of the wall pressure spectrum. The conclusions of this investigation can be found below.

- Within the parameters defined in this study, it appears that the wall pressure spectrum and boundary layer parameters are almost independent of roughness distribution.

- The smooth and rough wall pressure spectrum scale on both the classical and mixed outer boundary layer variables at low frequencies $0.2 \lesssim \omega\delta^*/U_e \lesssim 3$ using the form $\Phi(\omega)U_e/(\tau_w^2\delta)\ vs.\ \omega\delta/U_e$ and $\Phi(\omega)U_e/(\tau_w^2\delta^*)\ vs.\ \omega\delta^*/U_e$ respectively.

- A universal viscous scaling of the form $\Phi(\omega)u_\nu^2/(\tau_\nu^2\nu)\ vs.\ \omega\nu/u_\nu^2$ collapses the highest frequencies $\omega\nu/u_\nu^2 \gtrsim 0.6$ of the wall pressure spectrum for both smooth and rough walls using a single variable. This variable has been named the viscous friction velocity u_ν and is used to determine τ_ν as $\tau_\nu = \rho u_\nu^2$

- For smooth wall boundary layers u_ν is equal to the friction velocity u_τ, and for rough wall boundary layers u_ν is always less than u_τ, since it appears to be the friction velocity without the contribution from the pressure drag on the roughness elements. When applying this reasoning, estimates of u_ν come close to the observed values.

- Using Blake's (1970) scaling $\Phi(\omega)u_\tau/(\tau_w^2 k_g)\ vs.\ \omega k_g/u_\tau$ or Varano's (2010) variant $\Phi(\omega)/(\rho^2 U_e^3 k_g)\ vs.\ \omega k_g/U_e$, the mid-frequencies tend to correlate quite well for the studies considered in this investigation. These scalings also depict the development of a -4/3 slope when plotted on a log-log scale at higher roughness Reynolds numbers.

- If there is sufficient scale separation between the boundary layer height, roughness size and viscous scale, it should follow that each of the corresponding regions scale on its corresponding length scale as was seen in this investigation. This, however, would suggest that sufficiently complex rough surfaces with multiple large length scale separations would produce spectral forms that have no universal mid or high frequency scaling even in high Reynolds number flows.

- When applied to a range of hydraulically smooth, transitionally rough and fully rough flows, the proposed empirical model shown in Equation 17 appears to describe the wall pressure spectra for the present study and Forest (2012).
- Surface roughness broadens the convective ridge of the wall pressure space-time correlation. This would suggest that the roughness inhibits the convective velocities within the inner portions of the boundary layer.

REFERENCES

Alexander, William Nathan. *Normalization of Roughness Noise on the Near-Field Wall Pressure Spectrum.* M.S. Thesis, Blacksburg, Virginia: Aerospace and Ocean Engineering Department, Virginia Tech, 2009.

Alexander W N, Devenport W J, and Glegg S A L, 2012, "Predictions of Sound from Rough Wall Boundary Layers", AIAA Journal, doi: 10.2514/1.J051840.

Aupperle, F. A., and R. F. Lambert. "Effects of Roughness on Measured Wall-Pressure Fluctuations beneath a Turbulent Boundary Layer." *The Journal of the Acoustical Society of America*, 1970: Vol. 47, pp. 359-370.

Blake, William K. "Turbulent Boundary-Layer Wall-Pressure Fluctuations on Smooth and Rough Walls." *Journal of Fluid Mechanics*, 1970: Vol. 44, pp. 637-660.

Blake, William. "Turbulent Velocity and Pressure Fields in Boundary-Layer Flows Over Rough Surfaces." *Turbulence in Liquids Symposium.* University of Missouri-Rolla, October 5, 1971.

Bennington, L. Jeremy. *Effects of Various Shaped Roughness Elements in Two-Dimensional High Reynolds Number Turbulent Boundary Layers.* MS Thesis, Blacksburg, VA: Aerospace and Ocean Engineering Department Virginia Tech, 2004.

Borgoltz, Aurelien. *Modifications of Coherent Structures in Fan Blade Wakes for Broadband Noise Reduction.* Ph.D Dissertation, Blacksburg, VA: Aerospace and Ocean Engineering Department, Virginia Tech, 2007.

Bradshaw, P. "'Inactive' Motion and Pressure Fluctuations in Turbulent Boundary Layers." *Journal of Fluid Mechanics*, 1967: Vol. 30, pp. 241-258.

Bandyopadhyay P. R. and R. D. Watson, "Structure of rough-wall turbulent boundary layers, "Physics of Fluids, vol. 31, pp. 1877-1883, July 1988.

Bull, M. K. "Wall-Pressure Fluctuations Associated with Subsonic Turbulent Boundary Layer Flow." *Journal of Fluid Mechanics*, 1967: Vol. 28, pp. 719-754.

Corcos, G. M. "Resolution of Turbulence in Pressure." *The Journal of the Acoustical Society of America*, 1963: Vol. 35, No. 2, pp. 192-199.

Crede, Erin Dawne. *Aerodynamics and Acoustics of the Virginia Tech Stability Tunnel Anechoic System.* M.S. Thesis, Blacksburg, VA: Aerospace and Ocean Engineering Department, Virginia Tech, 2008.

Devenport, W. J., R. Burdisso, A. Borgoltz, A., RAVETTA, P. A., BARONE, M. F., BROWN, K. A. AND Morton, M. A., 2013, "The Kevlar-walled anechoic wind tunnel", *Journal of Sound and Vibration*, vol. 332(17), pp. 3971-3991.

Devenport, W. J., R. Burdisso, A. Borgoltz, R. Patricio, and M. Barone. "Aerodynamic and Acoustic Corrections for a Kevlar-Walled Anechoic Wind Tunnel." *16th AIAA/CEAS Aeroacoustics Conference.* Stockholm, Sweden, June 7-9, 2010. AIAA-2010-3749.

Devenport, William J., Dustin L. Grissom, W. Nathan. Alexander, Benjamin S. Smith, and Stewart A.L. Glegg. "Measurements of Roughness Noise." *Journal of Sound and Vibration*, 2011: doi:10.1016/j.jsv.2011.03.017.

Dirling, R. B., Jr. "A Method for Computing Roughwall Heat Transfer Rates on Reentry Nosetips." *8th AIAA Thermophysics Conference.* Palm Springs, California, July 16-18, 1973. AIAA-1973-763.

Farabee, Theodore M., and Mario J. Casarella. "Spectral Features of Wall Pressure Fluctuations beneath Turbulent Boundary Layers." *Physics of Fluids*, 1991: Vol. A3, No. 10, pp. 2410-2420.

Fernholz, H., and P. Finley. "The Incompressible Zero-Pressure Gradient Turbulent Boundary Layer: An Assessment of the Data." *Progress in Aerospace Science*, 1996: Vol. 32, pp. 245-311.

Forest, J., 2012, "The Wall Pressure Spectrum of High Reynolds Number Rough-Wall Turbulent Boundary Layer", M.S. Thesis, Aerospace and Ocean Engineering Department, Virginia Tech.

Glegg S, and Devenport W, 2009, "FAR-FIELD SOUND FROM ROUGH-WALL BOUNDARY LAYERS", PROC. R. SOC. A., VOL. 465, PP. 1717-1734.

Goody, Michael. *An Experimental Investigation of Pressure Fluctuations in Three-Dimensional Turbulent Boundary Layers.* Ph.D Dissertation, Blacksburg, VA: Aerospace and Ocean Engineering Department, Virginia Tech, 1999.

Goody, Michael. "Empirical Spectral Model of Surface Pressure Fluctuations." *AIAA Journal*, 2004: Vol. 24, No. 9.

Gravante, S. P., A. M. Naguib, C. E. Wark, and H. M. Nagib. "Characterization of the Pressure Fluctuations Under a Fully Developed Turbulent Boundary Layer." *AIAA Journal*, 1998: Vol. 36, No. 10, pp. 1808-1816.

Horne, Michael P. *Physical and Computational Investigation of the Wall Pressure Fluctuations in a Channel Flow.* NRL Memorandum Report 6628, Washington, DC: Laboratory for Computational Physics and Fluid Dynamics, 1990.

Jiménez, Javier. "Turbulent Flows over Rough Walls." *Annual Review of Fluid Mechanics*, 2004: Vol. 36 pp. 173-196.

Liu Y. and Dowling A. P., 2007, "Assessment Of The Contribution Of Surface Roughness To Airframe Noise", AIAA Journal, vol. 45, no. 4, pp. 855-870.

Maury C., Gardonio P. and Elliott S. J., 2002, "A Wavenumber Approach To Modeling The Response Of A Randomly Excited Panel, Part II: Application To Aircraft Panels Excited By A Turbulent Boundary Layer", Journal of Sound and Vibration, vol. 252, pp. 115-139.

McGrath, B., and R. Simpson. *Some Features of Surface Pressure Fluctuations in Turbulent Boundary Layers with Zero and Favorable Pressure Gradients.* NASA Contract Rep. 4051, Blacksburg, Va: Aerospace and Ocean Engineering Department, Virginia Tech, 1987.

Moriarty P. J., Guidati G. and Migliore P., 2005, "Prediction Of Turbulent Inflow And Trailing-Edge Noise For Wind Turbines", 11th AIAA/CEAS Aeroacoustics Conference, Monterey CA, May 23-25, AIAA-2005-2881.

Morrison, J. F., C. S. Subramanian, and P. Bradshaw. "Bursts and the Law of the Wall in Turbulent Boundary Layers." *Journal of Fluid Mechanics*, 1992: Vol. 241, pp. 75-108.

Morrison, Jonathan F. "The Interaction Between Inner and Outer Regions of Turbulent Wall-Bounded Flow." *Philosophical Transactions of the Royal Society*, 2007: Vol. 365, pp. 683-698.

Morton, M. A., 2012, "Rotor Inflow Noise Caused by a Boundary Layer: Inflow Measurements and Noise Predictions", M.S. Thesis, Aerospace and Ocean Engineering Department, Virginia Tech, 2012.

Nikuradse J., Strmungsgesetze in rauhen Rohren,"VDI-Forschchungsheft, vol. 361,1933. English translation, "Laws of ow in rough pipes," NACA TM 1292, 1950.

Oerlemans S., Sijtsma P. and Mendez Lopez B., 2007, “Location And Quantification Of Noise Sources On A Wind Turbine”, Journal of Sound and Vibration, vol. 299, pp. 869-883.

Panton, Ronald L., and John H. Linebarger. "Wall Pressure Spectra Calculations for Equilibrium Boundary Layers." *Journal of Fluid Mechanics*, 1974: Vol. 65 pt. 2, pp. 261-287.

Perry A. E., W. H. Schoeld, and P. N. Joubert, \Rough wall turbulent boundary layers, "Journal of Fluid Mechanics, vol. 37, no. 2, pp. 383-413, 1969.

Remillieux, M. C., *et al*. "Calibration and Demonstration of the New Virginia Tech Anechoic Wind Tunnel." *14th AIAA/CEAS Aeroacoustics Conference.* Vancouver, British Columbia, May 5-7, 2008. AIAA-2008-2911.

Schetz, Joseph. *Boundary Layer Analysis.* Upper Saddle River, NJ: Prentice-Hall Inc., 1993.

Schlichting, Herman. *Boundary-Layer Theory.* McGraw-Hill, Inc, 1979.

Smith, B. S., H. E. Camargo, R. A. Burdisso, and W. J. Devenport. "Development and Testing of a Novel Acoustic Wind Tunnel Concept." *11th AIAA/CEAS Aeroacoustics Conference.* Monterey, CA, May 23-25, 2005. AIAA-2005-3053.

Smith, Benjamin S. *Wall Jet Boundary Layer Flows Over Smooth and Rough Surfaces.* Ph.D Dissertation, Blacksburg, VA: Aerospace and Ocean Engineering Department, Virginia Tech, 2008.

Varano, Nathaniel D. *Fluid Dynamics and Surface Pressure Fluctuations of Turbulent Boundary Layers Over Sparse Roughness.* Ph.D Dissertation, Blacksburg, VA: Aerospace and Ocean Engineering Department, Virginia Tech, 2010.

Wittmer, K. S., W. J. Devenport, and J. S. Zsoldos. "A Four Sensor Hot Wire Probe System for Three Component Velocity Measurements." *Experiments in Fluids*, 1998: Vol. 24, pp. 416-423.

Yang, Q. and Wang, M.,"Computational Study of Roughness-Induced Boundary-Layer Noise" AIAA JOURNAL Vol. 47, No. 10, October 2009

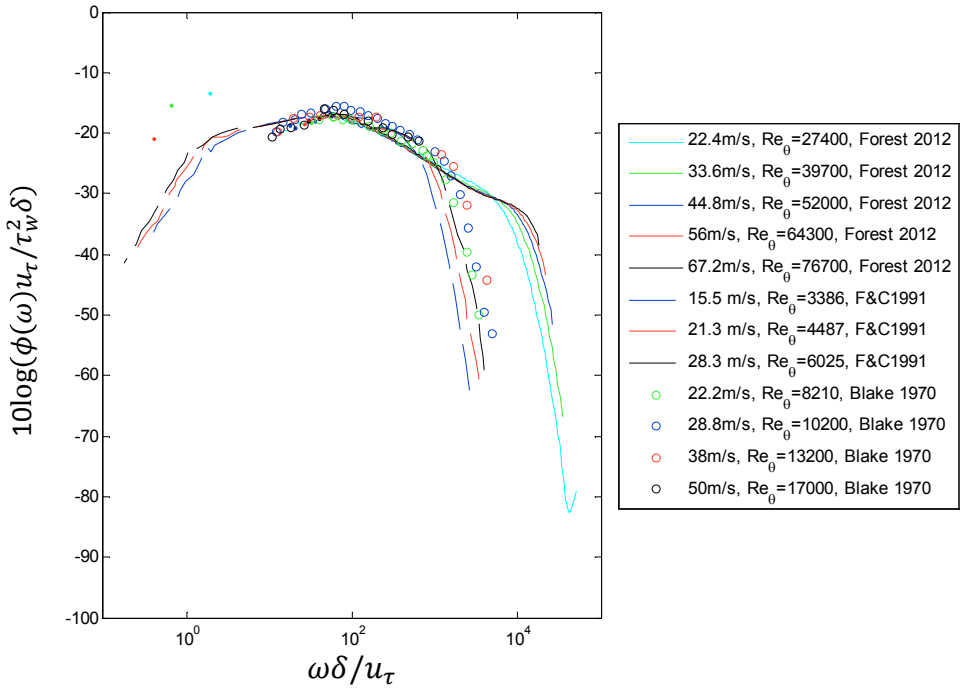

Figure 1: Classical outer scaling applied to smooth wall data from Blake (1970), Farabee and Casserella (1991), and Forest (2012)

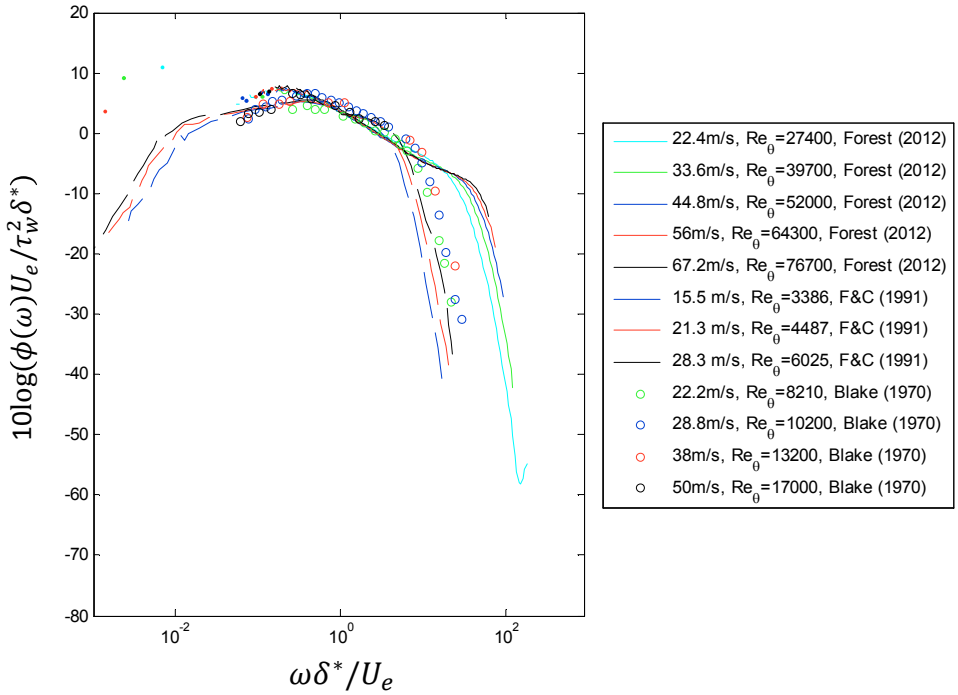

Figure 2: Mixed outer scaling applied to smooth wall data from Blake (1970), Farabee and Casserella (1991), and Forest (2012)

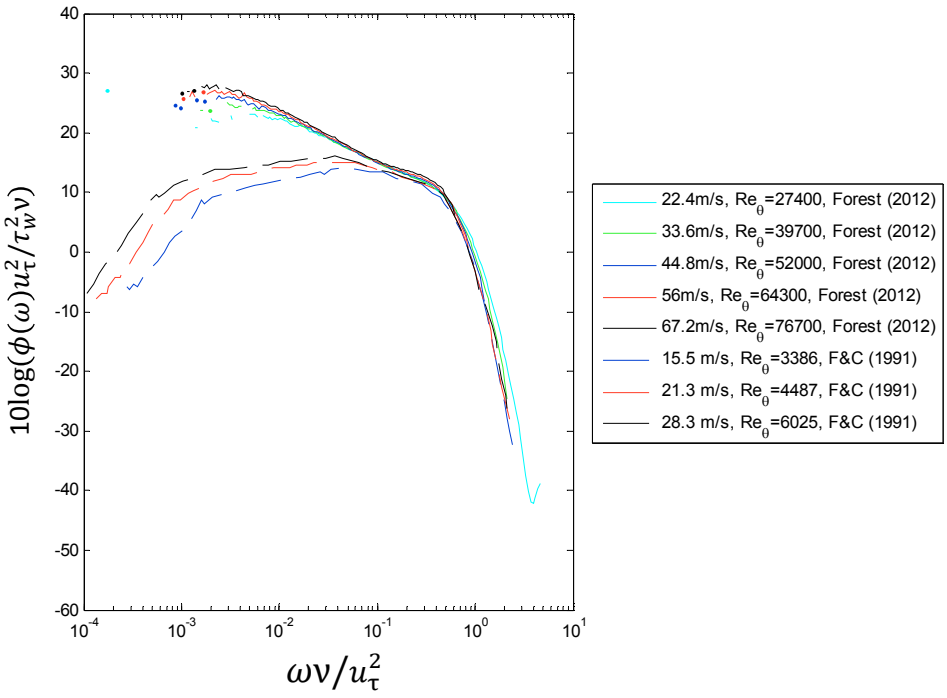

Figure 3: Viscous scaling applied to smooth wall data from Blake (1970), and Forest (2012)

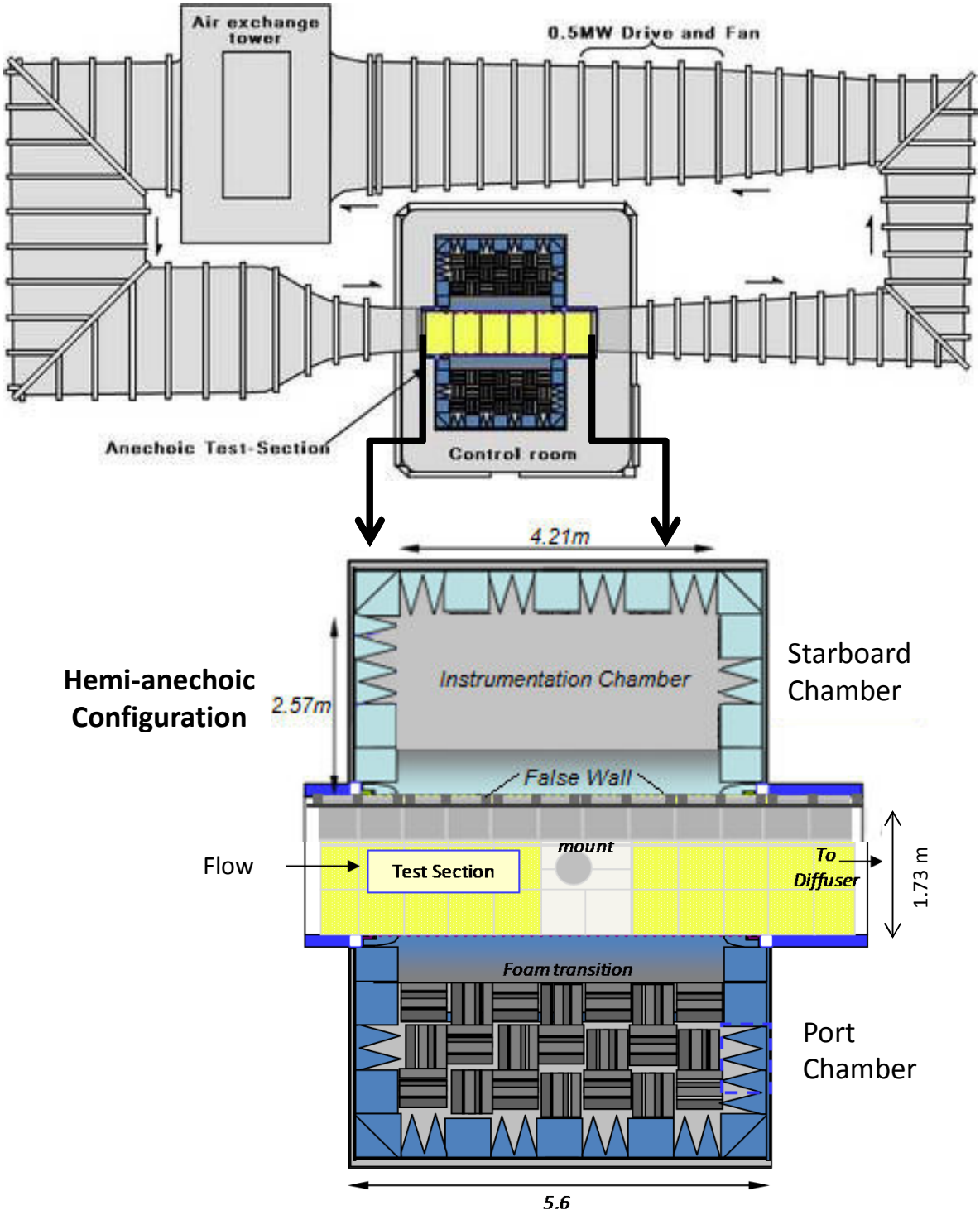

Figure 4: The Virginia Tech Stability Wind Tunnel (figure courtesy of AOE Department) shown with the full anechoic configuration, and its modification to the hemi-anechoic test section used for this investigation. (Modified figure used with permission of Dr. William J. Devenport and Jonathan B. Forest)

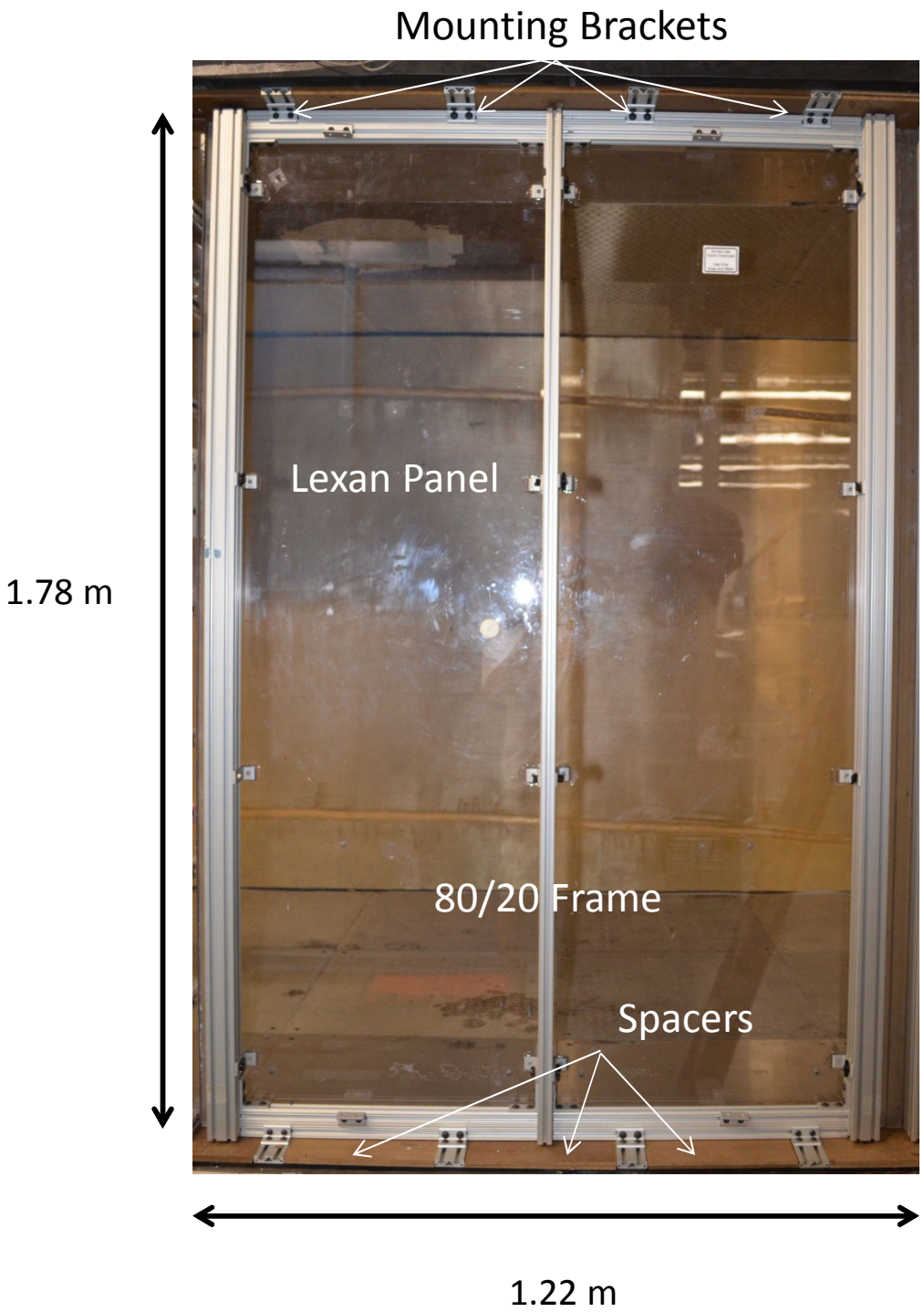

Figure 5: Framed Lexan panel and mounting system

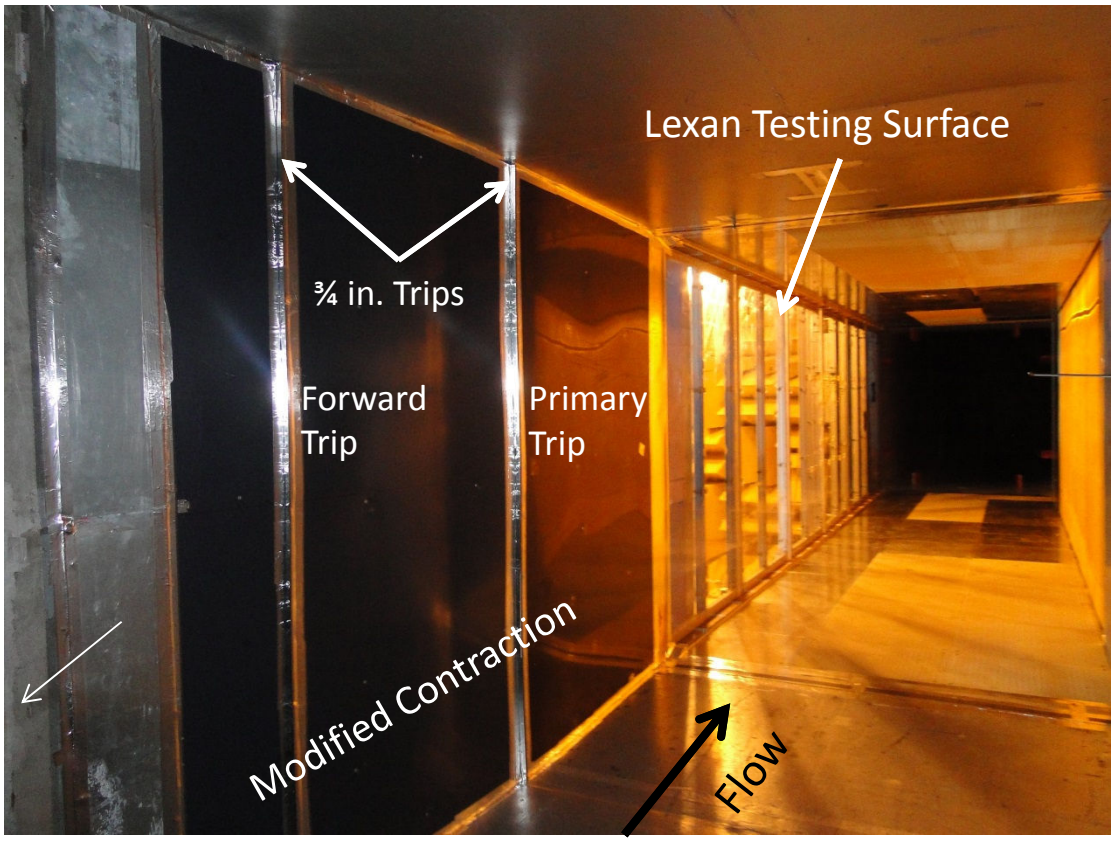

Figure 6: Modified contraction, primary trips and testing surface

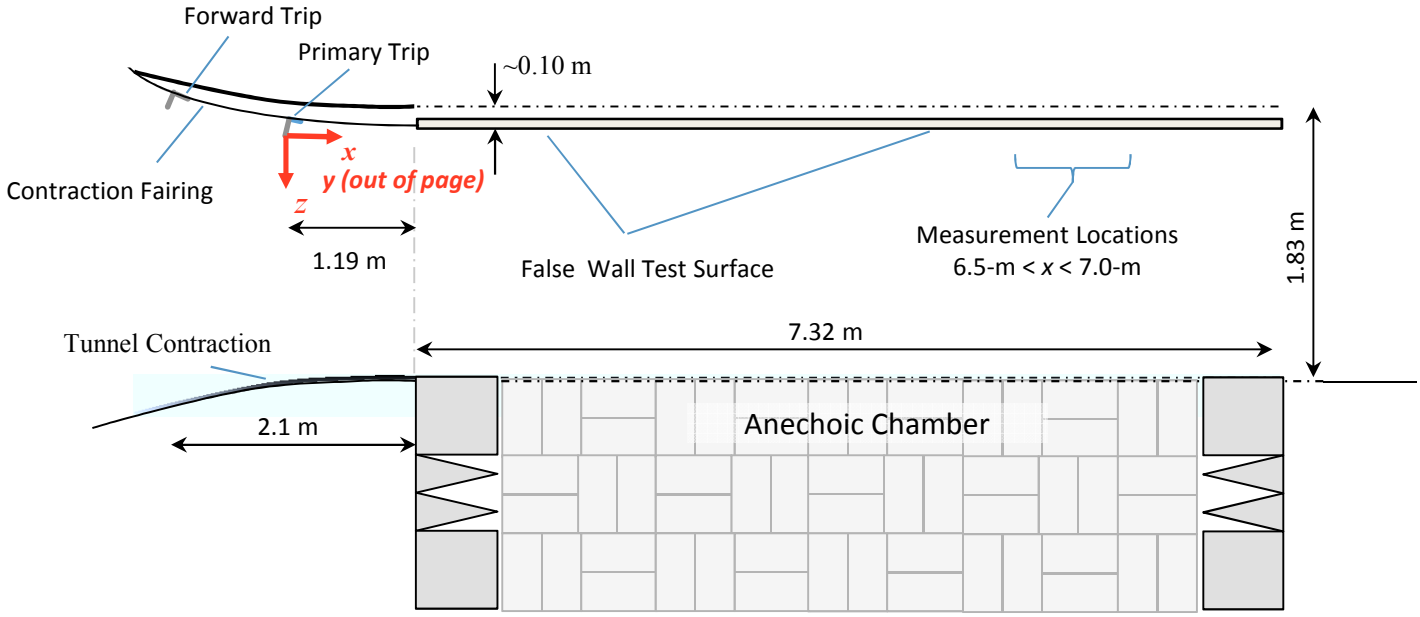

Figure 7: General test section configuration and coordinate system where the *x*, *y*, and *z* coordinates correspond to the streamwise, spanwise, and wall normal coordinate. The origin of which is located at the primary trip at the centerline and flush with the testing surface. (Modified figure used with permission of Jonathan B. Forest)

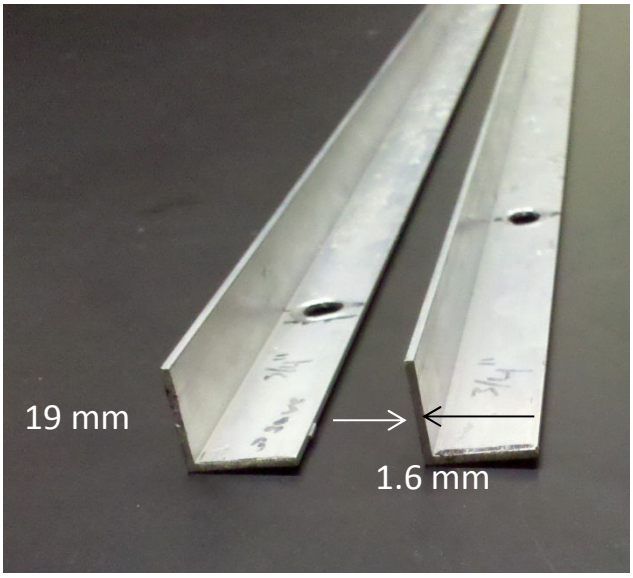

Figure 8: Forward and primary 19 mm angled aluminum trips

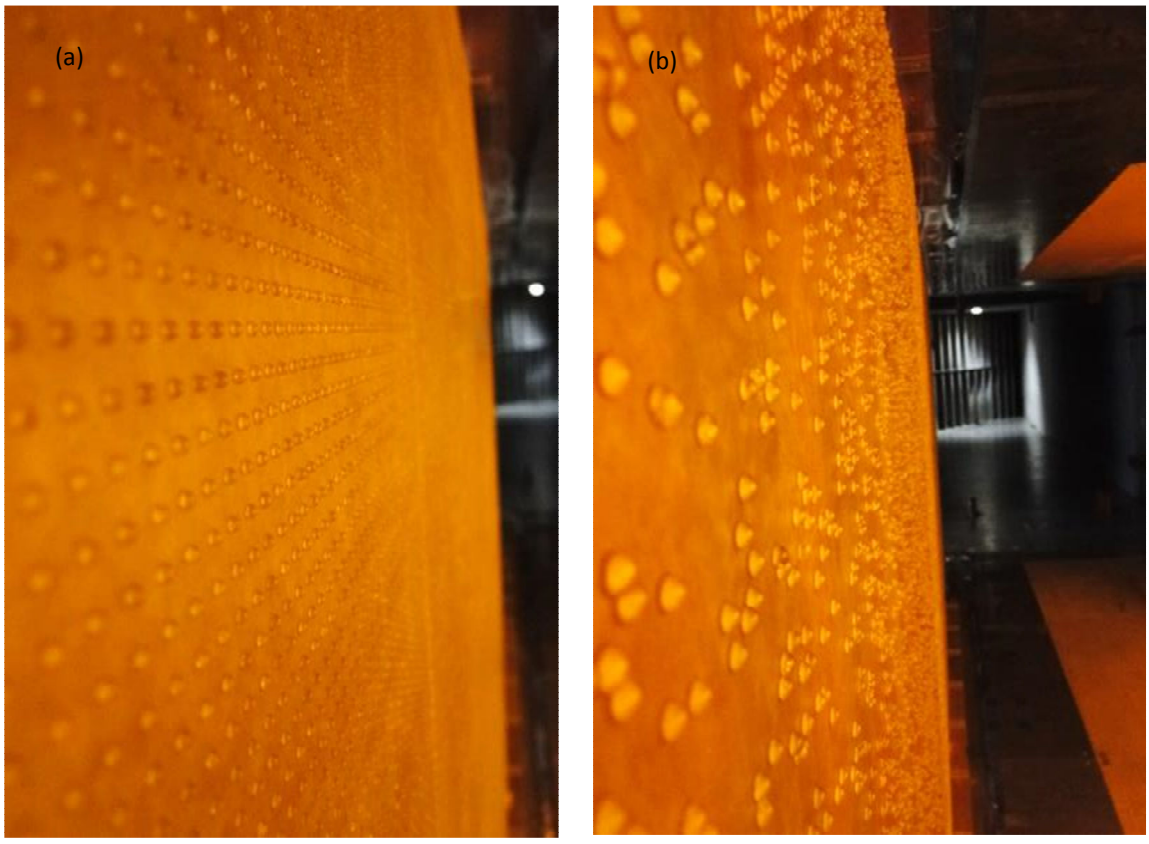

Figure 9: Ordered distribution of 1-mm hemispherical roughness (a) and random distribution of 3-mm hemispherical roughness (b).

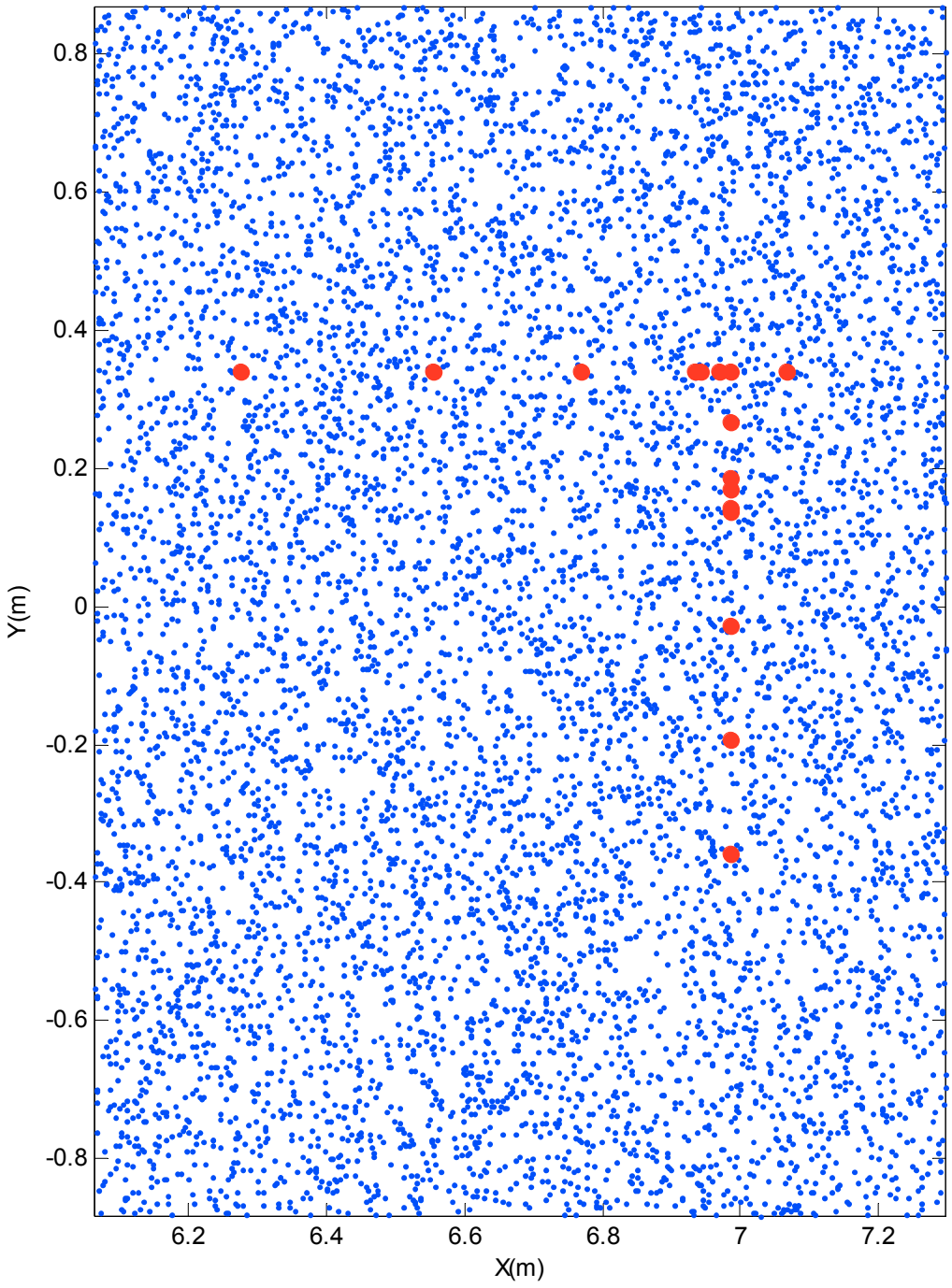

Figure 10: 3-mm random roughness distribution shown with microphone locations

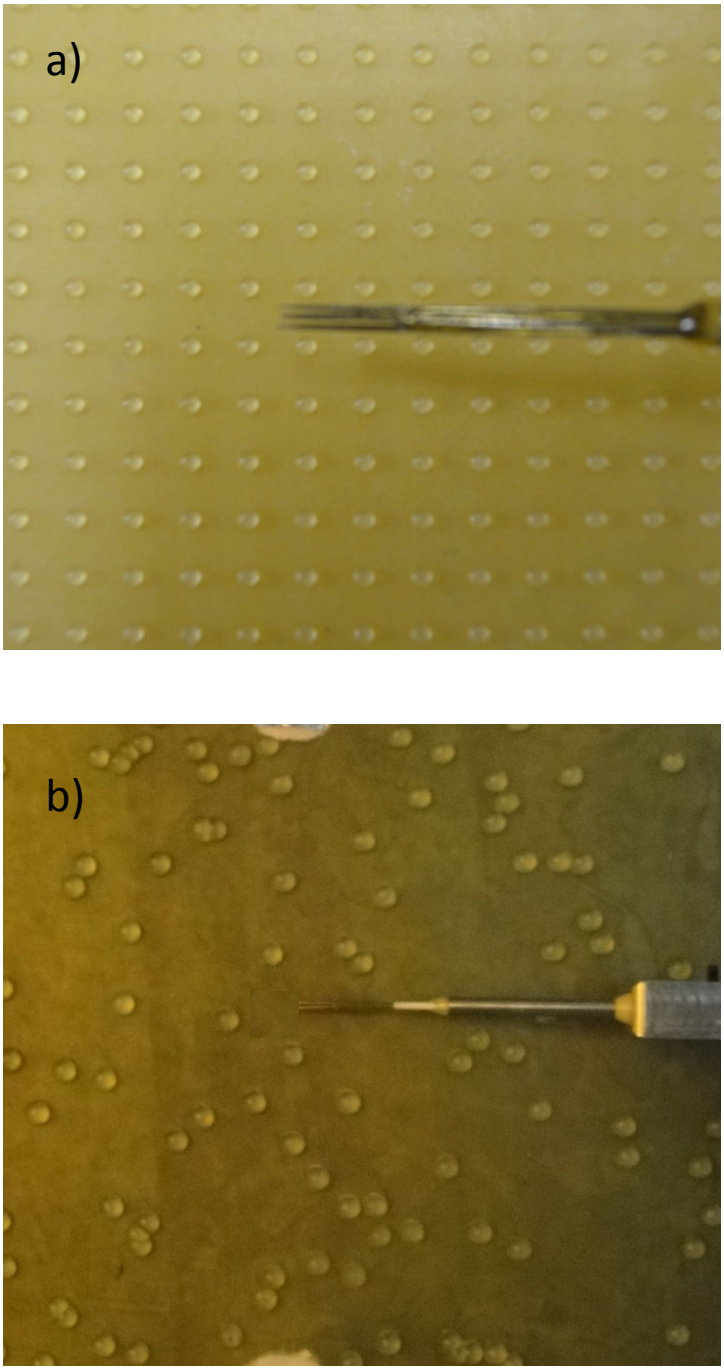

Figure 11: (a) quad-hotwire positioning with respect to 1-mm ordered roughness elements, and (b) quad-hotwire positioning with respect to 3-mm random roughness elements

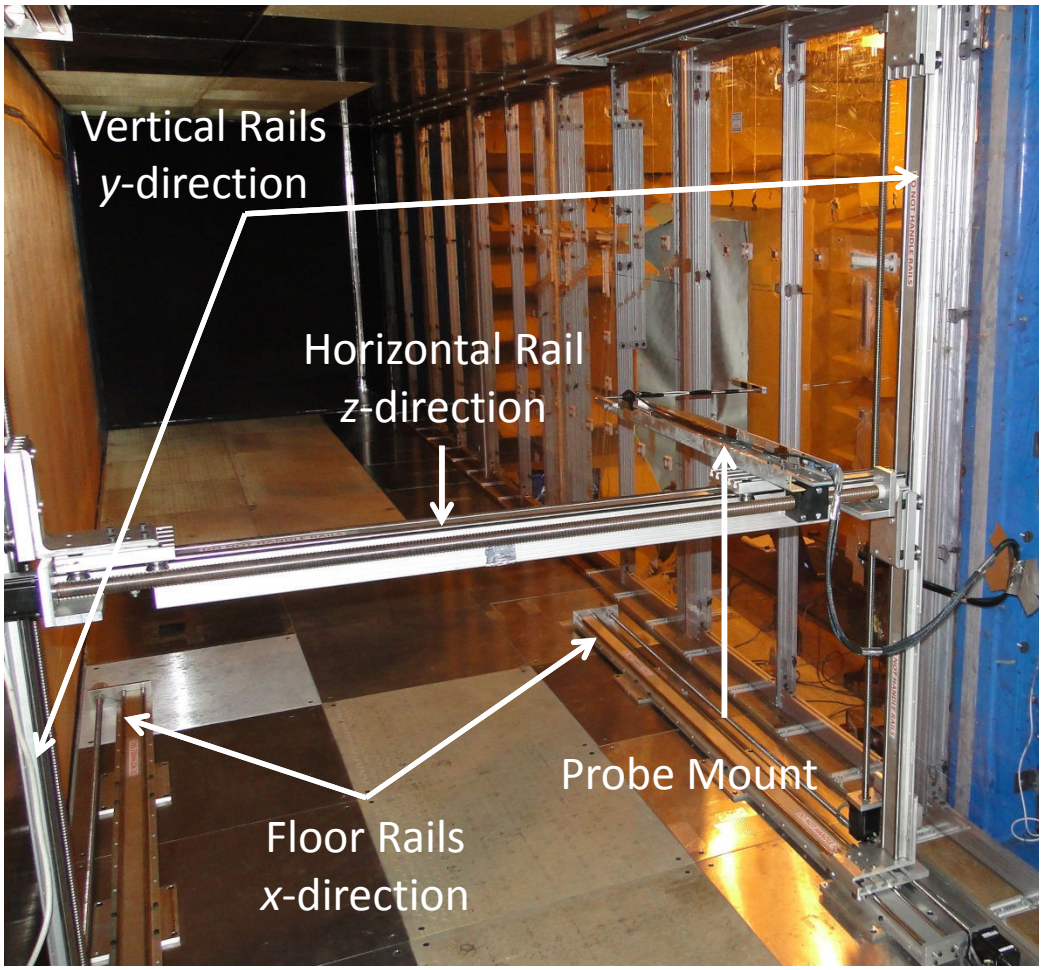

Figure 12: Traverse system used to position the hotwire probes.

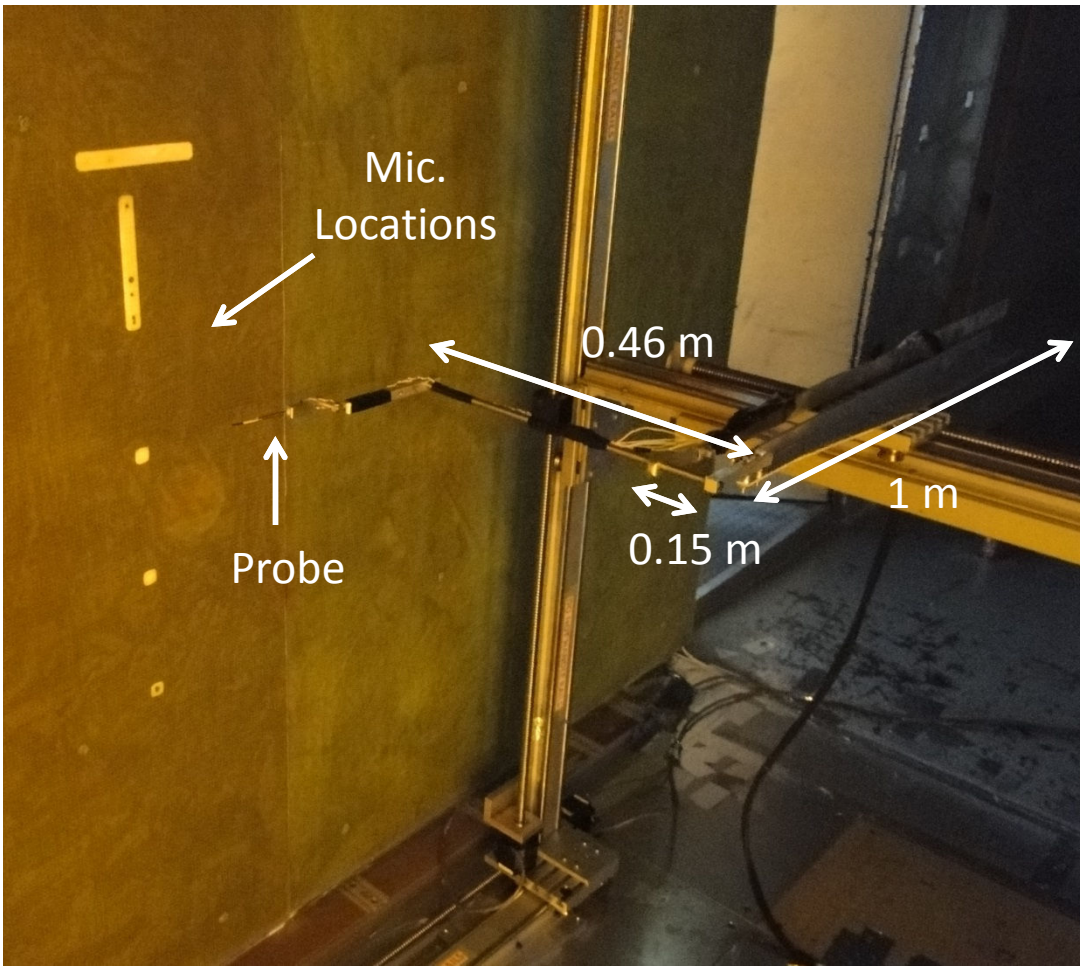

Figure 13: Traverse probe mount configuration

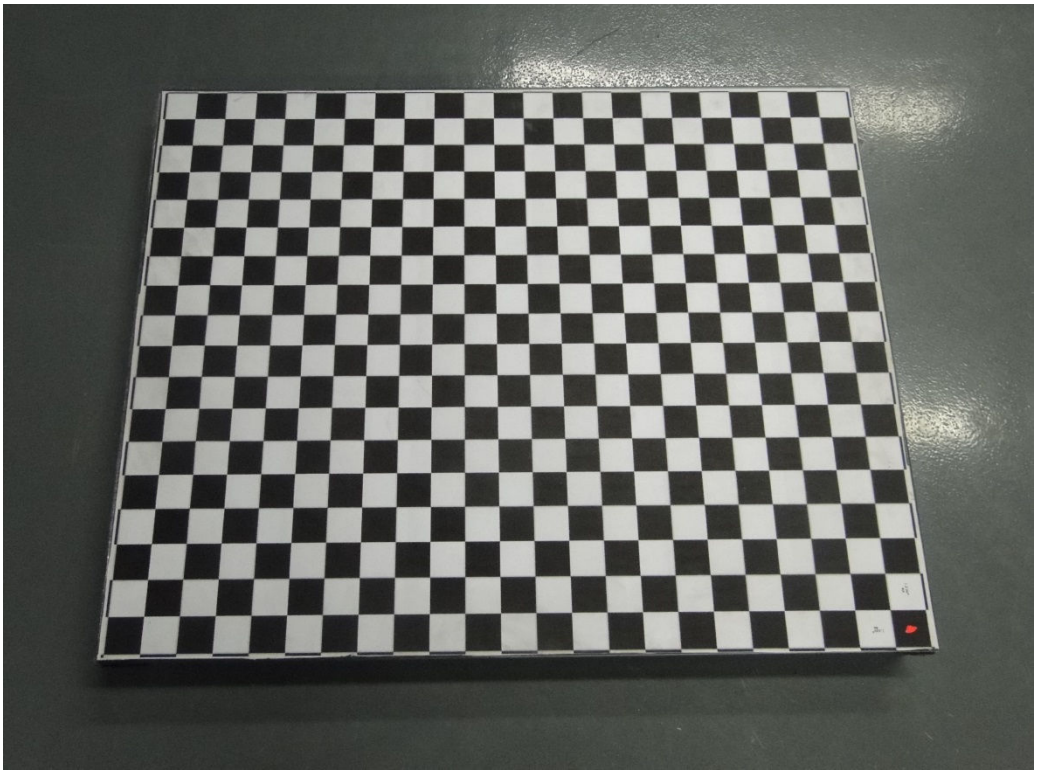

Figure 14: Example lens calibration photo

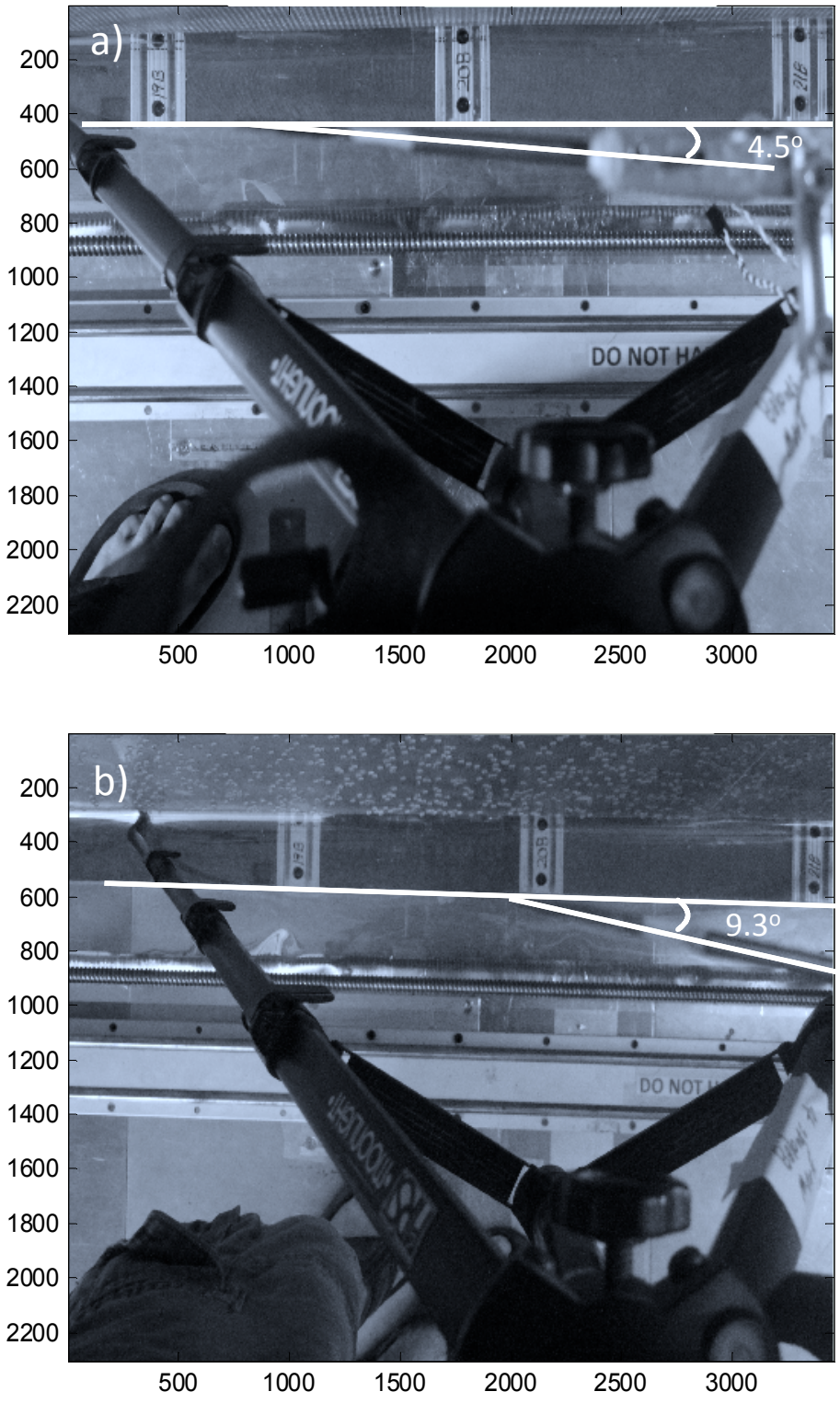

Figure 15: Undistorted measured yaw angles of the 1-mm ordered (a) and 3-mm random (b) rough surfaces.

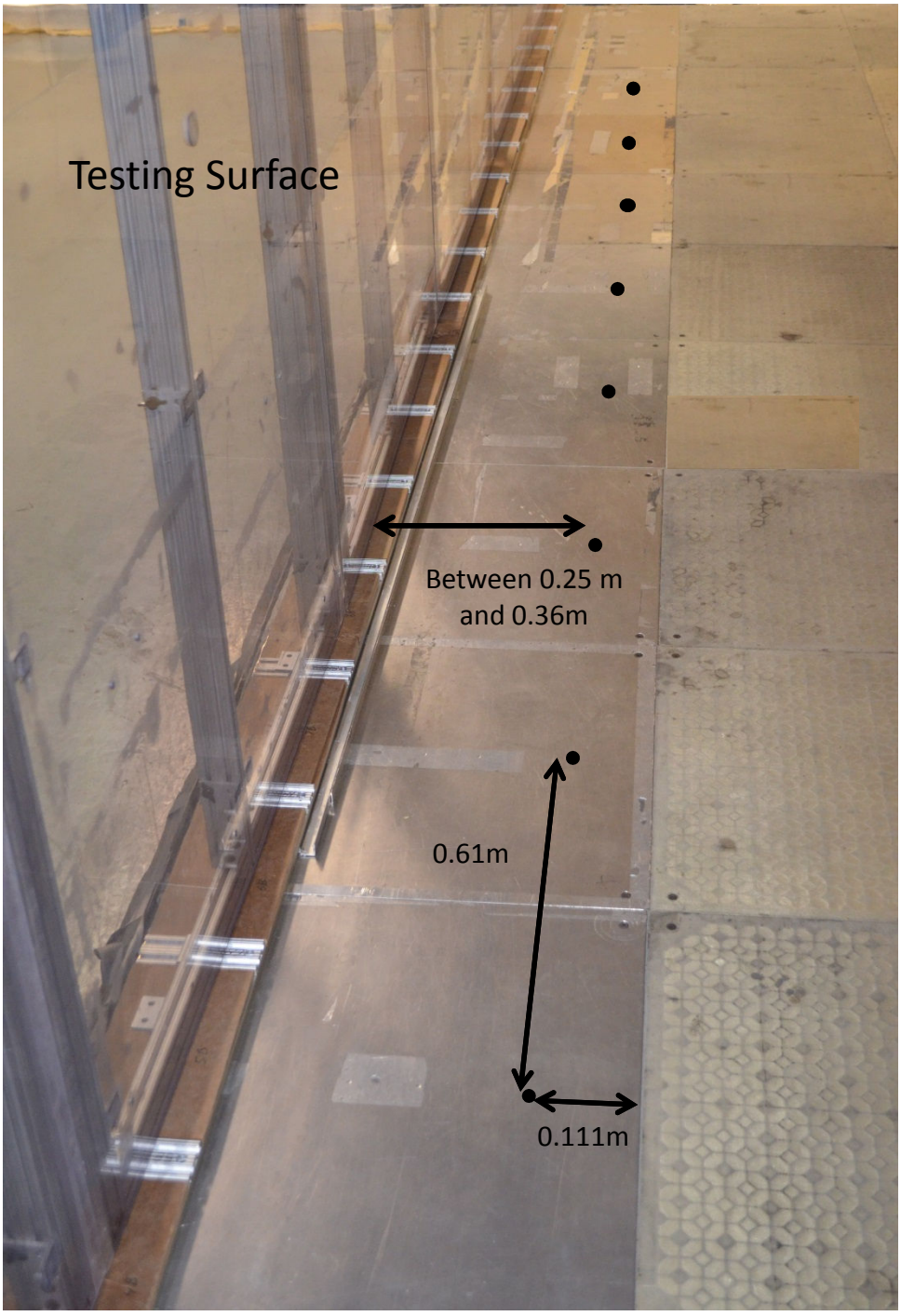

Figure 16: Example of ½ mm pressure tap locations

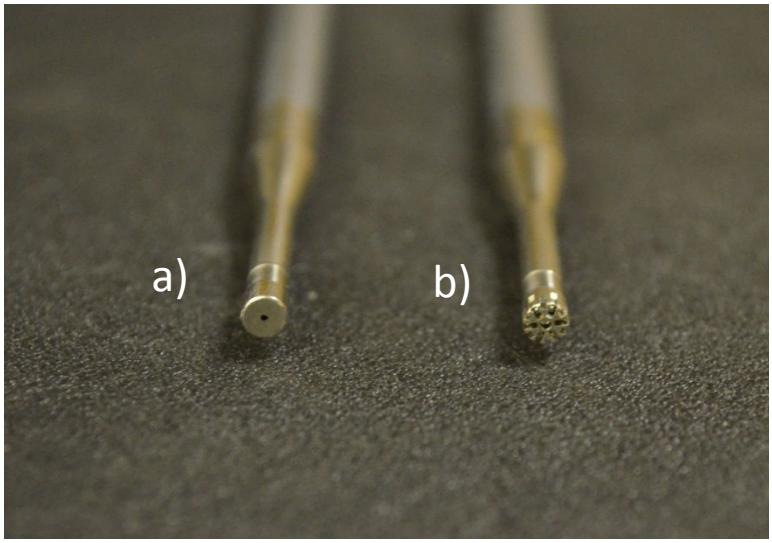

Figure 17: B&K 4138-A-015 1/8th inch microphones fitted with ½ mm pinhole cap (a) and standard microphone cap (b).

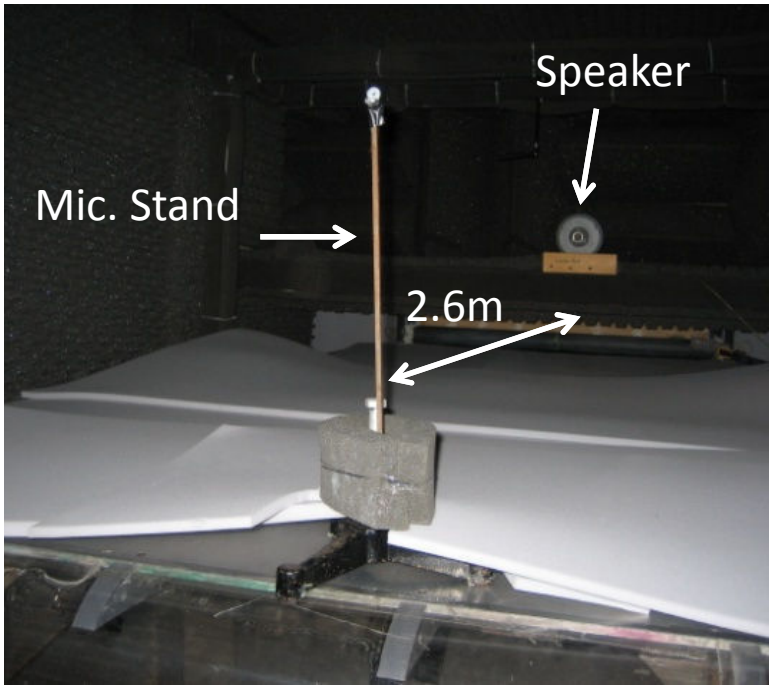

Figure 18: Microphone calibration setup

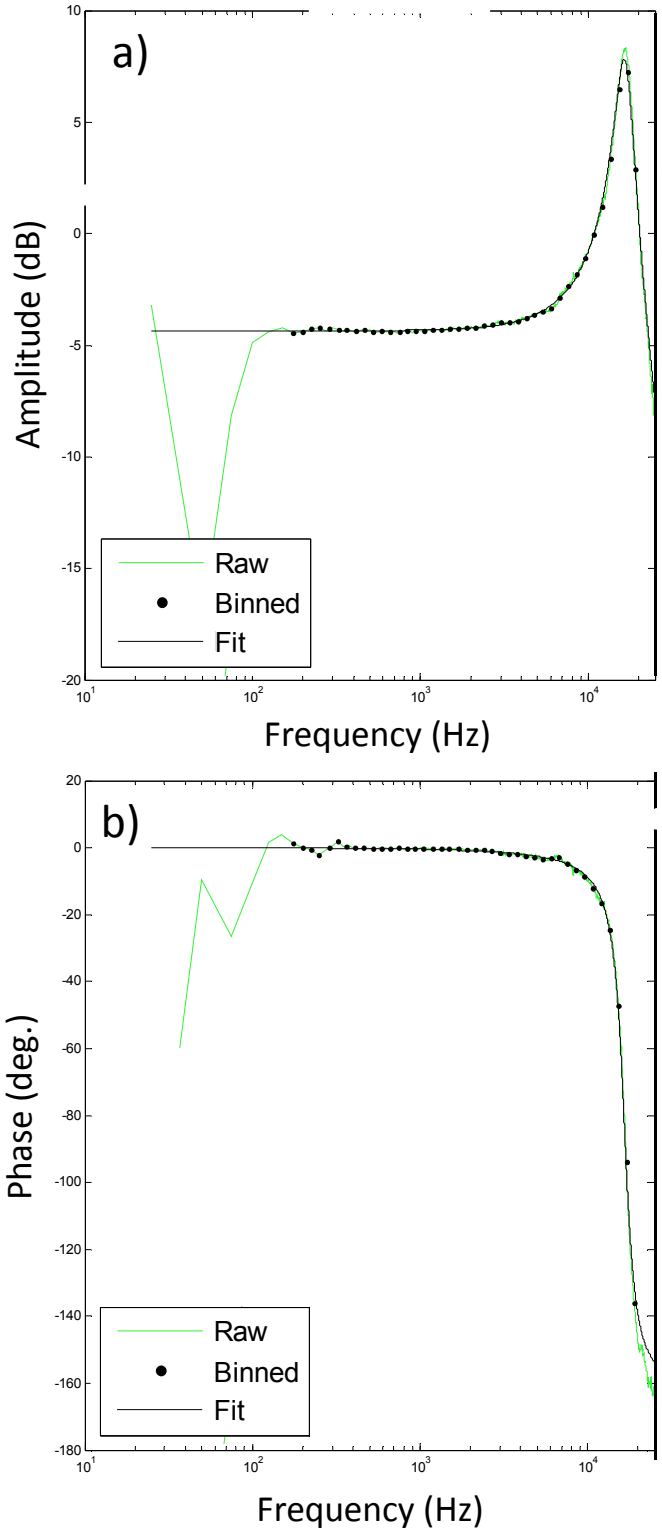

Figure 19: Optimized calibrations (black) plotted with raw calibration (green) for amplitude (a) and phase (b)

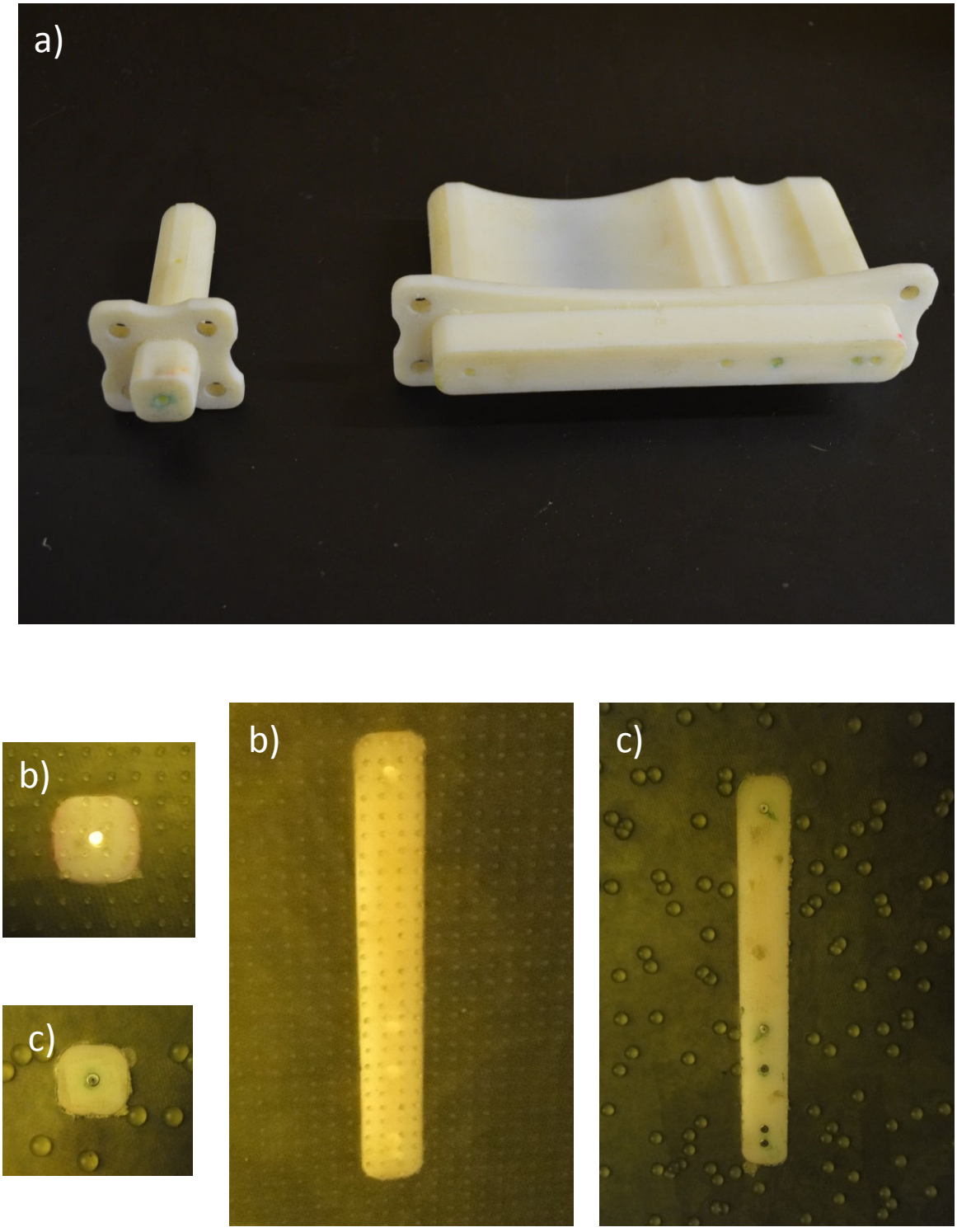

Figure 20: Microphone holders (a) and an example of the position of the holders with respect to the 1-mm ordered (b) and 3-mm random (c) roughness elements.

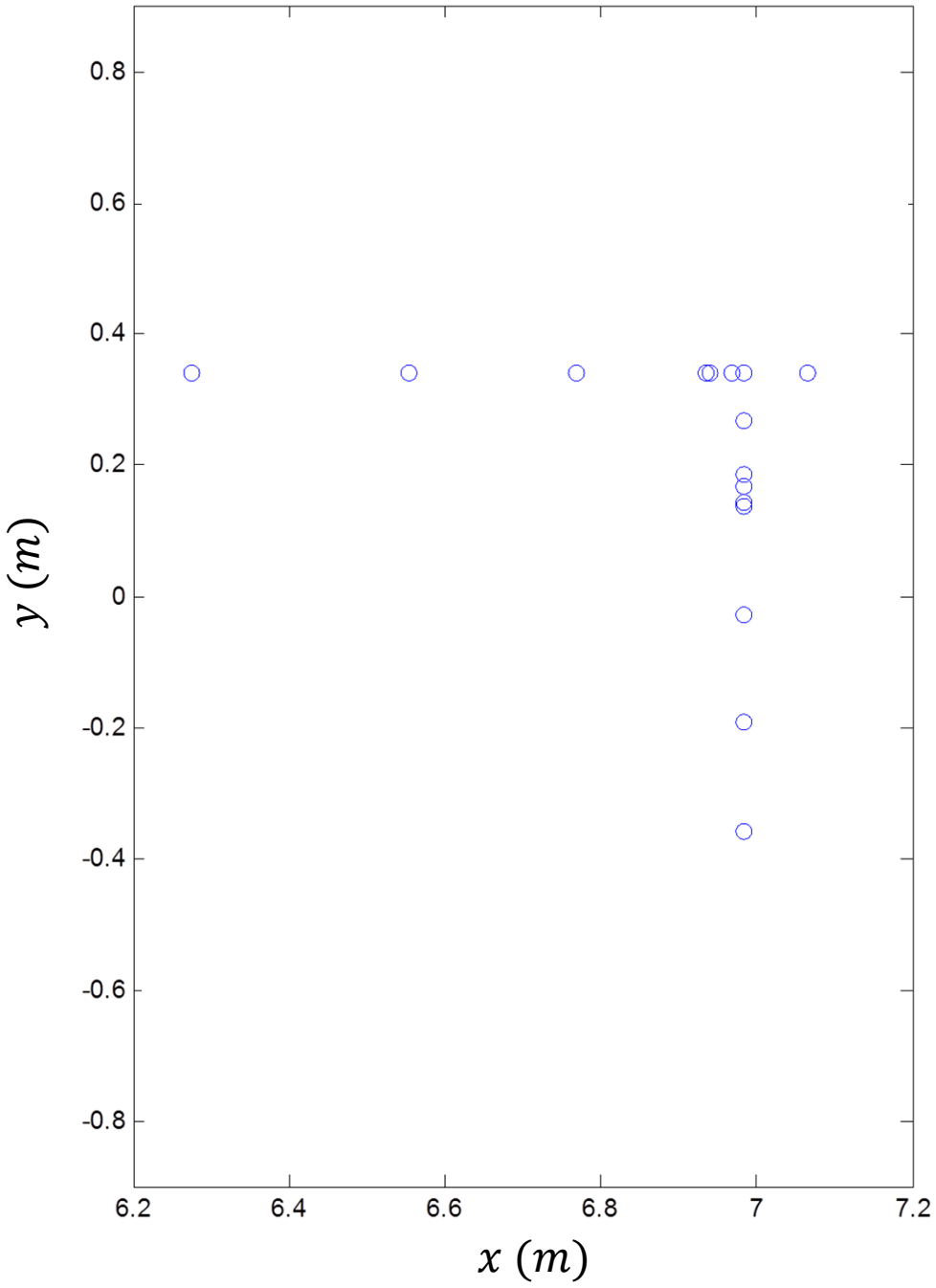

Figure 21: Microphone measurement locations with respect to the Lexan panel.

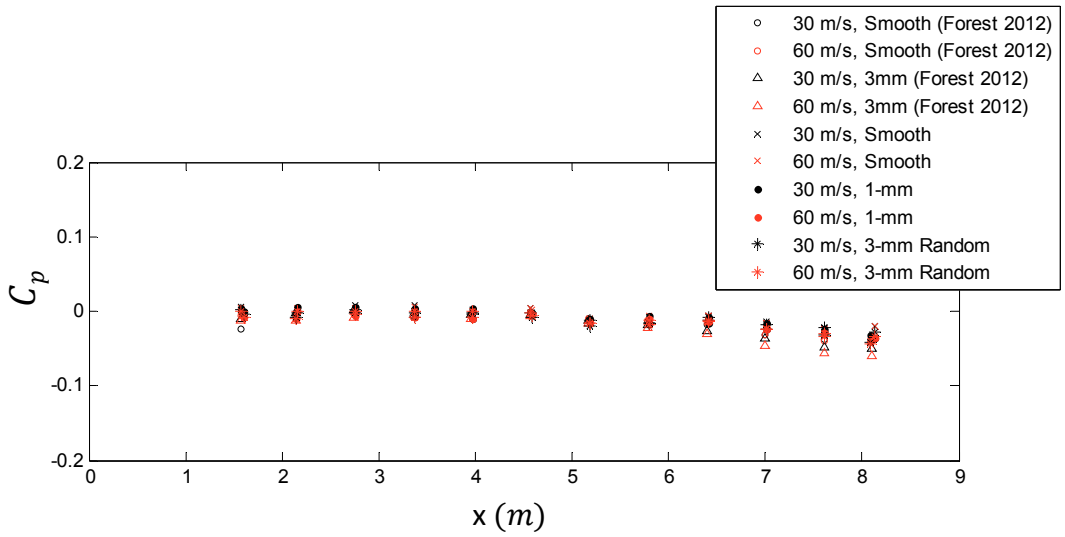

Figure 22: Mean streamwise pressure coefficient distribution as a function of surface type. Data from Forest (2012) included for comparison.

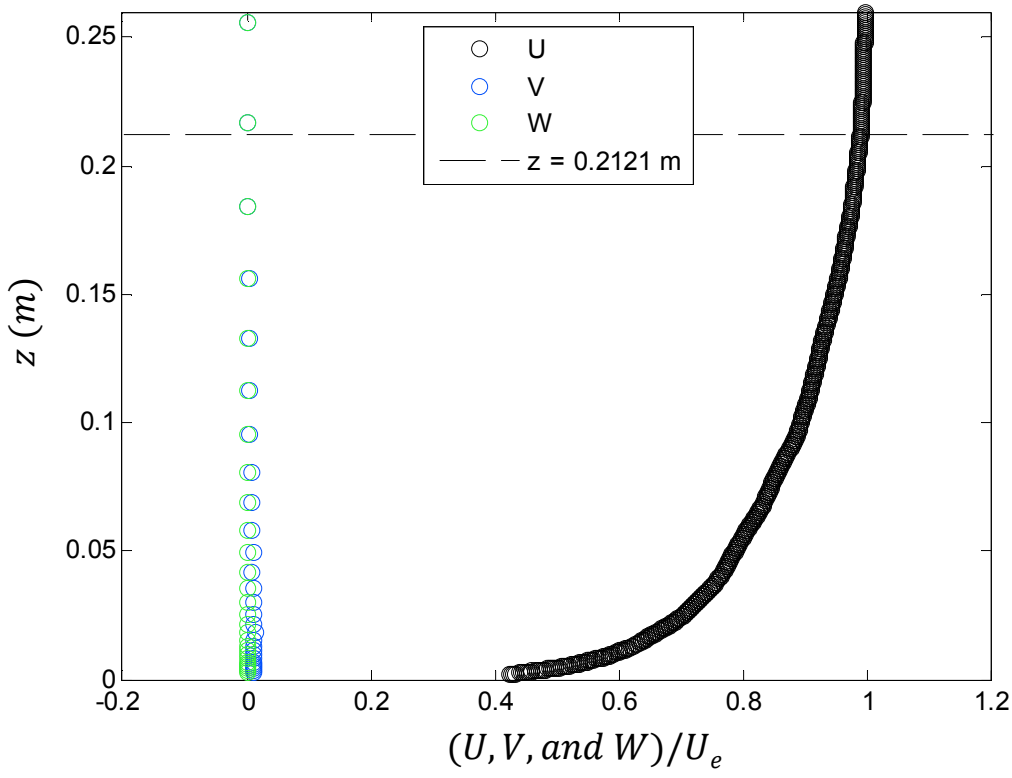

Figure 23: Boundary layer thickness determination from the quad hotwire for the 1-mm ordered roughness at 30 m/s.

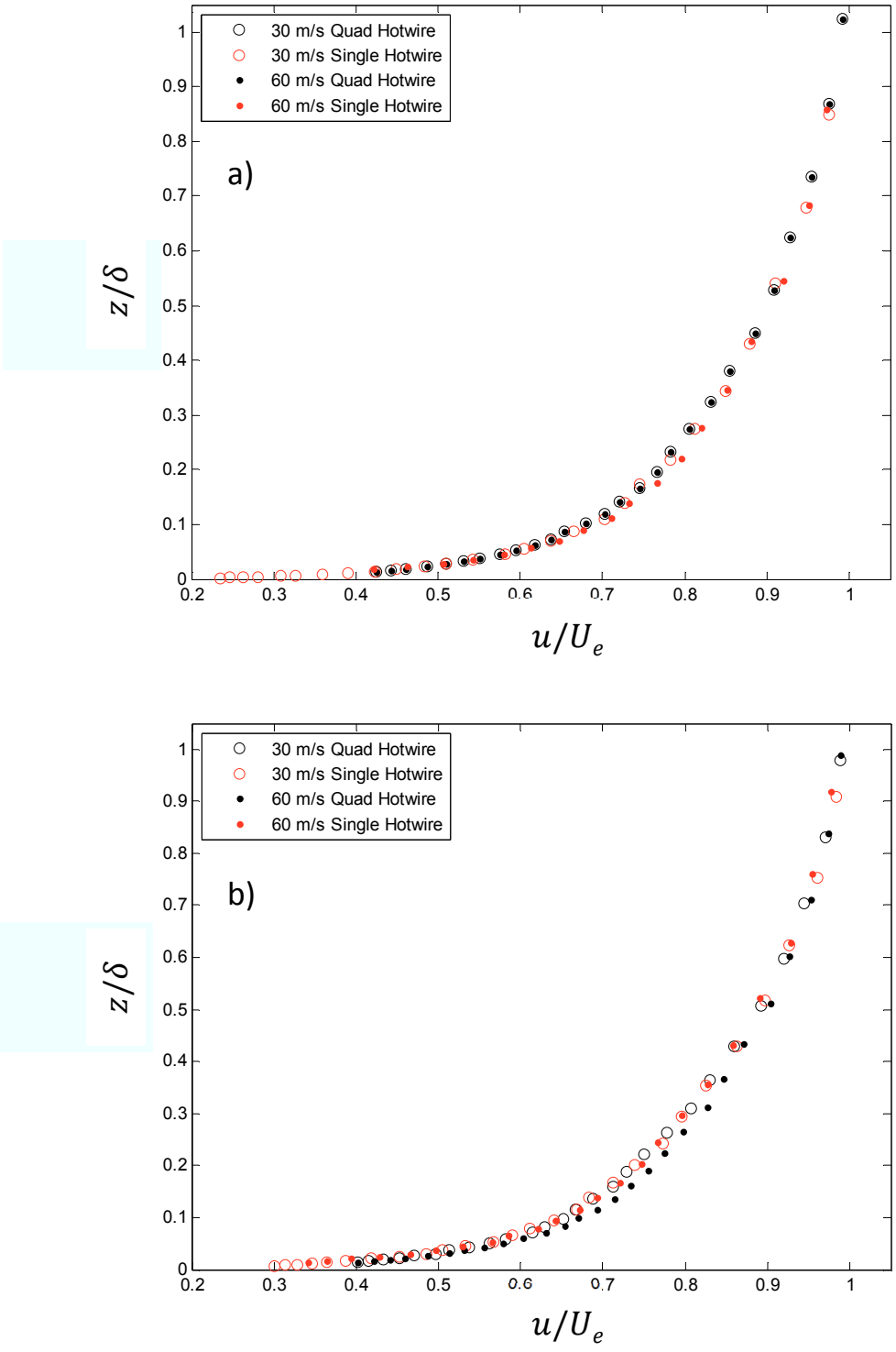

Figure 24: Boundary layer profile comparison of single and quad hot-wire results for (a) the 1-mm roughness and (b) the 3-mm random roughness

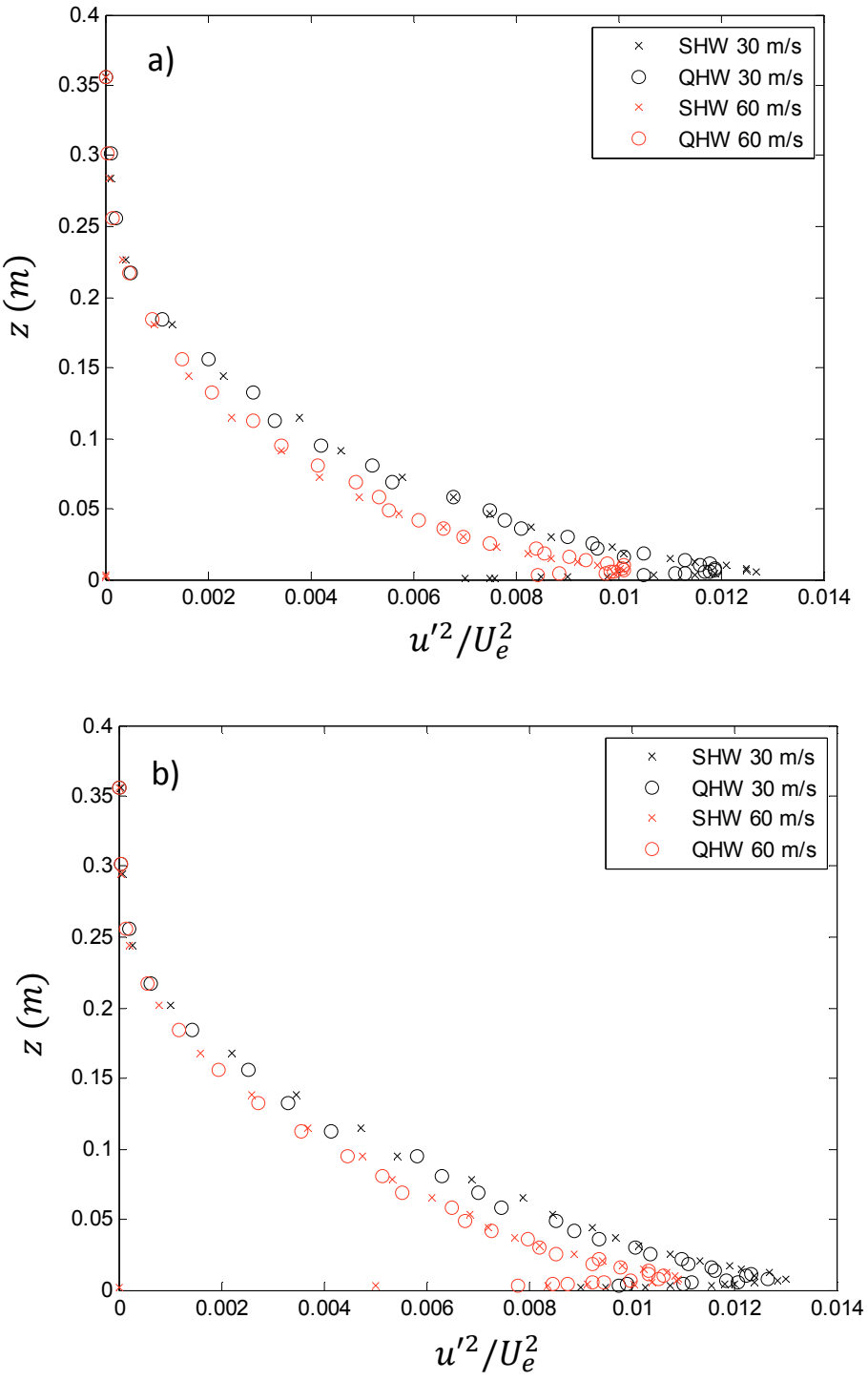

Figure 25: Comparison of single hotwire (SHW) and quad hotwire (QHW) u'^2/U_e^2 profiles for the 1-mm ordered (a) and 3-mm random (b) rough surface conditions.

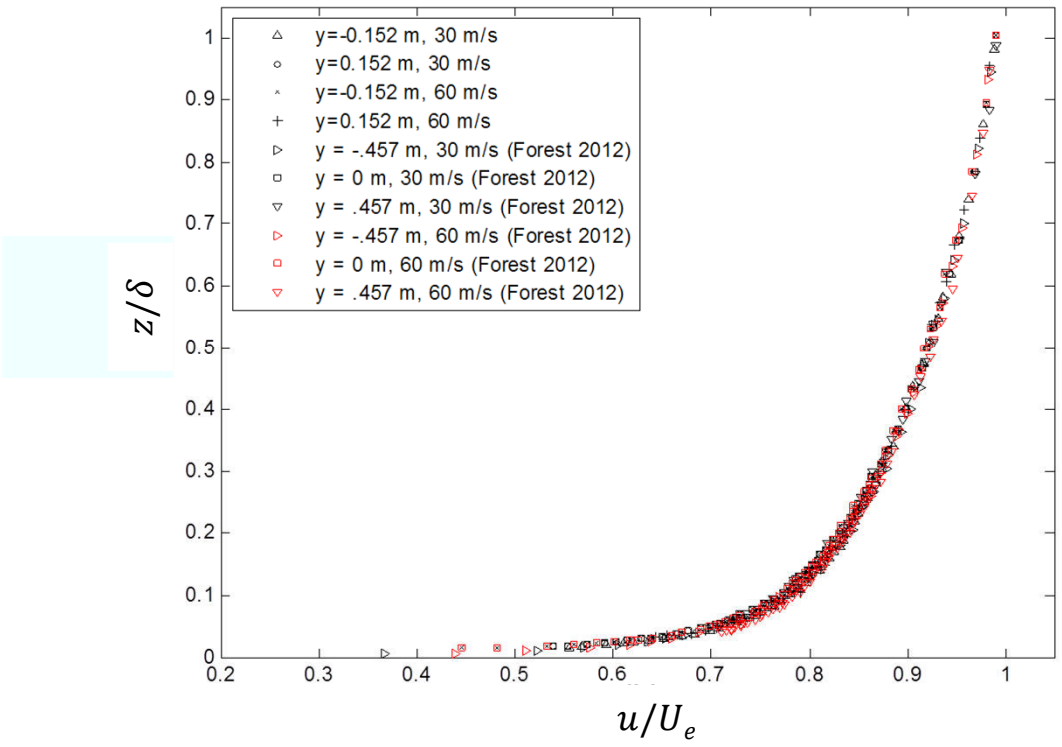

Figure 26: Boundary layer non-dimensionalized smooth surface profiles at 6.98 m for the present study's data at varying heights along the wall compared to data from Forest (2012).

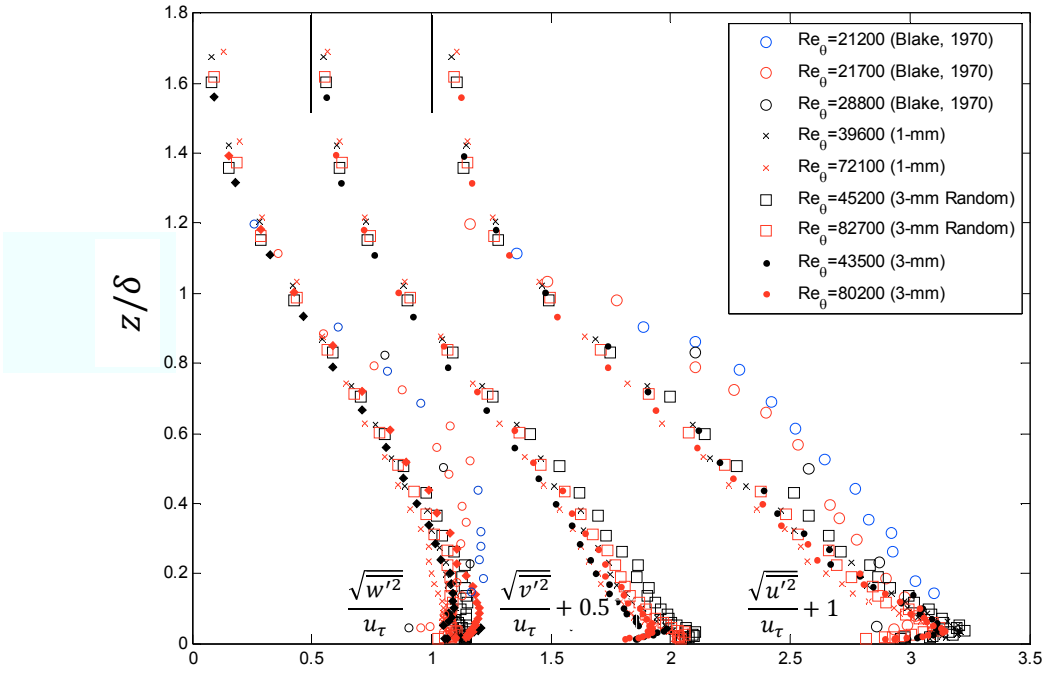

Figure 27: Rough surface turbulence intensity profiles where $\sqrt{\overline{v'^2}}/u_\tau$ is offset by +0.5 and $\sqrt{\overline{u'^2}}/u_\tau$ is offset by +1 as shown in figure. Data from Blake (1970) and Forest (2012) is also included.

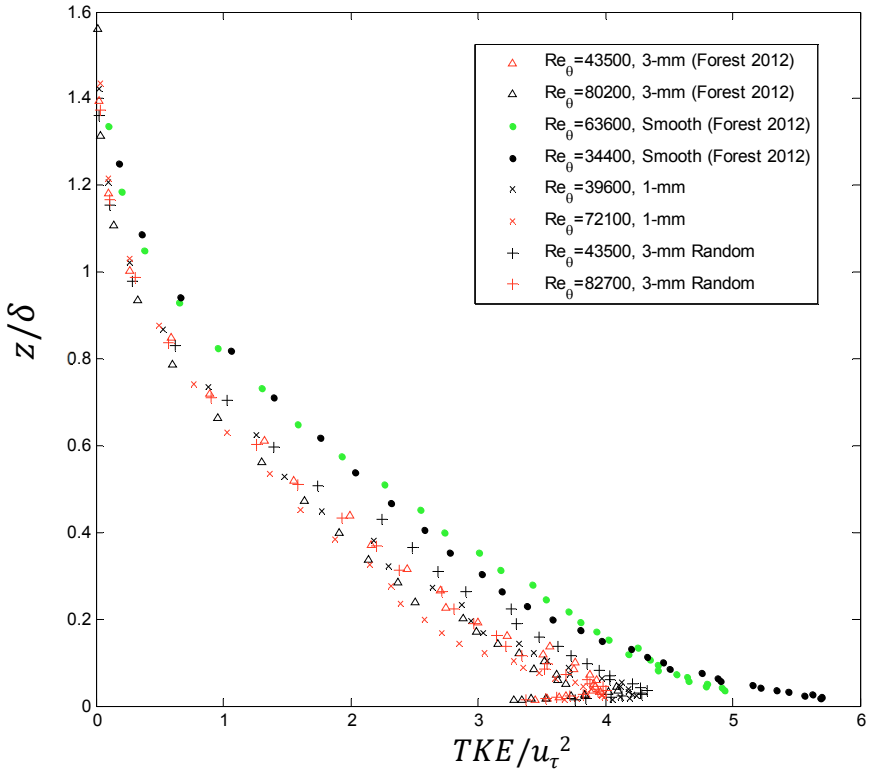

Figure 28: Turbulent kinetic energy profiles (TKE) plotted as *z*/δ *vs. TKE* /u_τ^2. Data from Forest (2012) included for comparison.

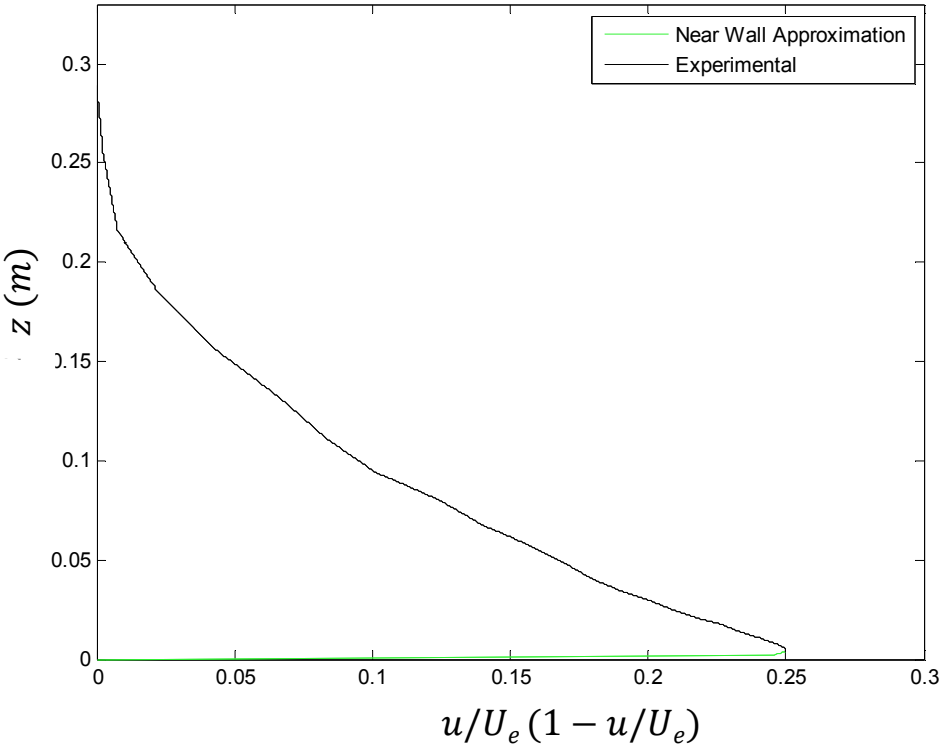

Figure 29: Momentum thickness estimation for the 1-mm ordered roughness at 30 m/s

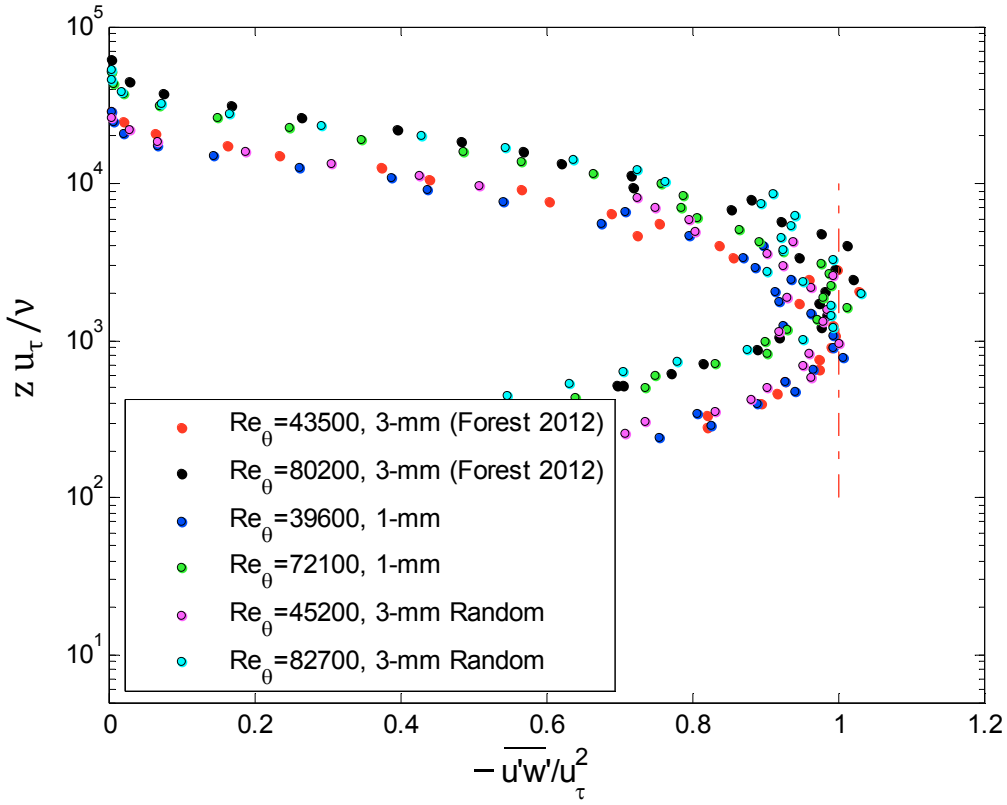

Figure 30: Inner scaling of rough surface Reynolds shear stress used to obtain u_τ

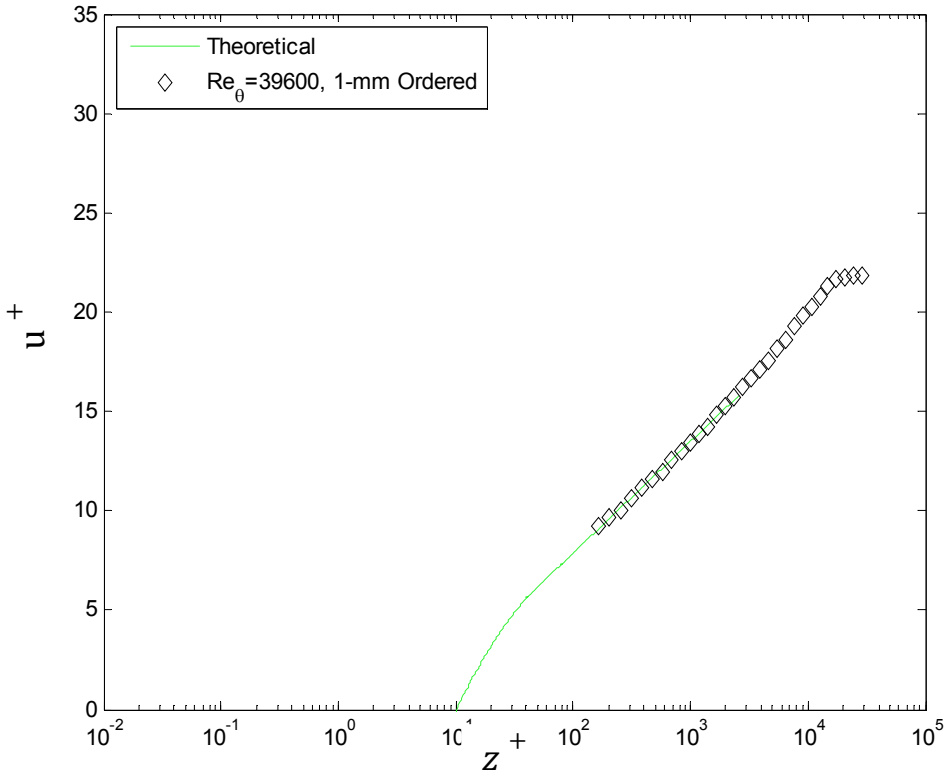

Figure 31: Experimental data compared to the theoretical results obtained from Equation 3.6 for the 1-mm ordered roughness at 30 m/s

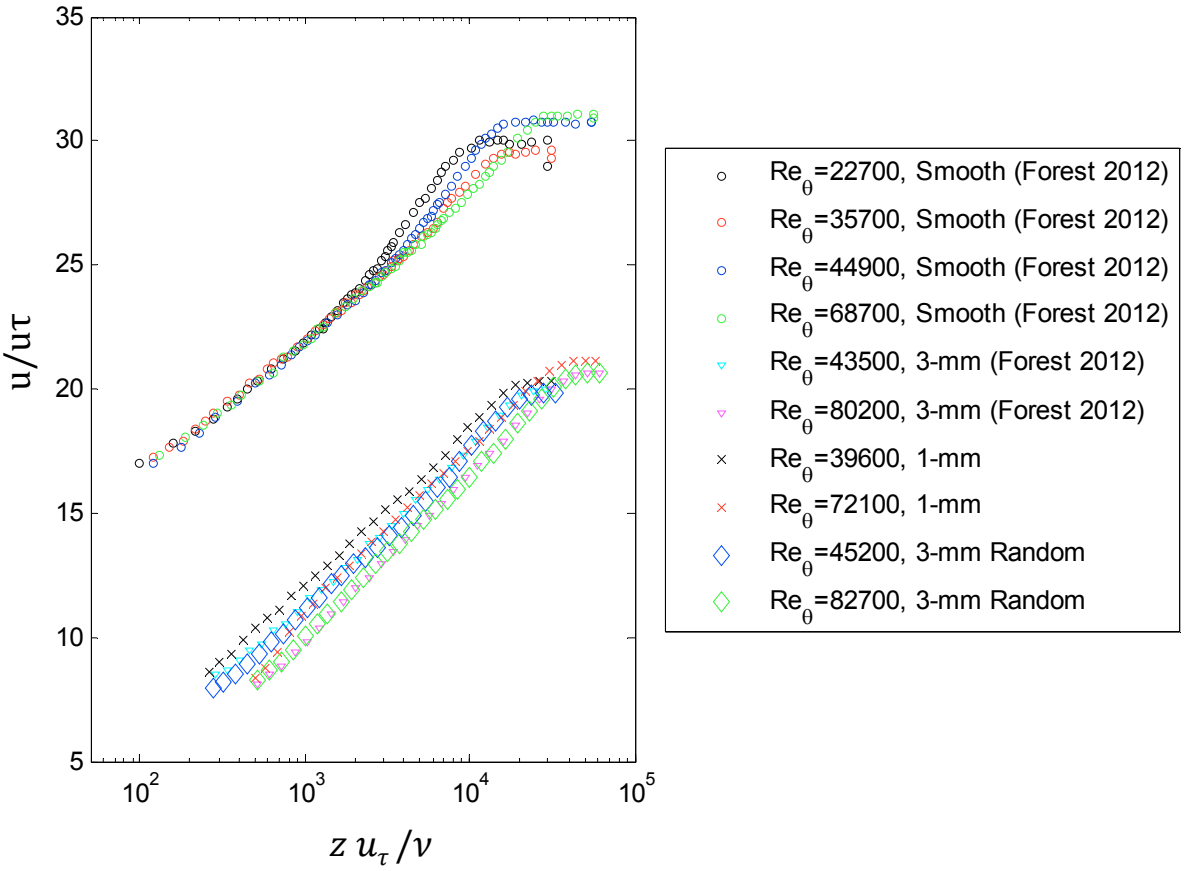

Figure 32: Mean velocity profiles plotted in terms of inner variables.

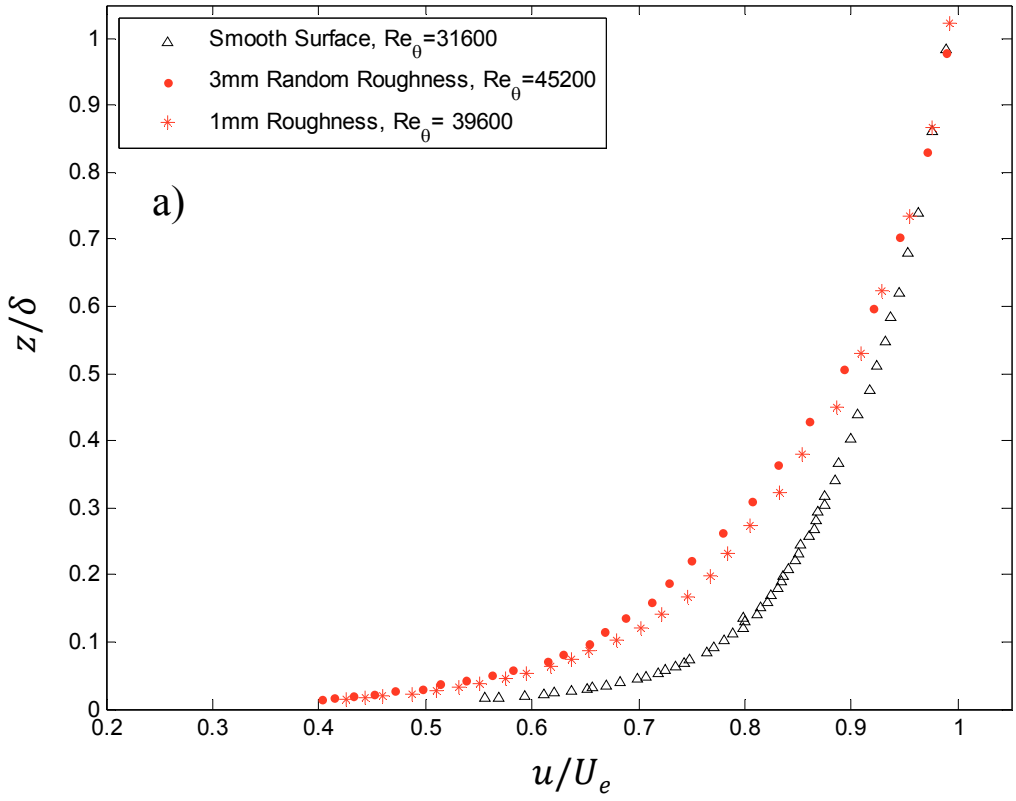

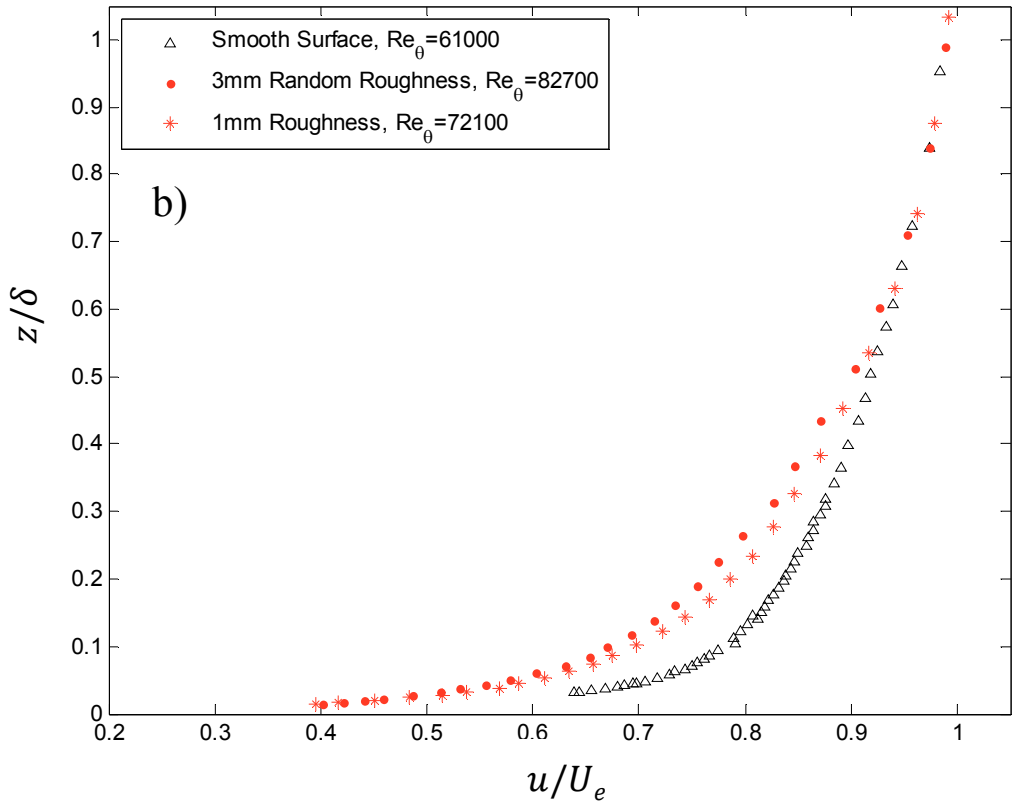

Figure 33: Boundary layer roughness effects comparison for 30 m/s (a) and 60 m/s (b).

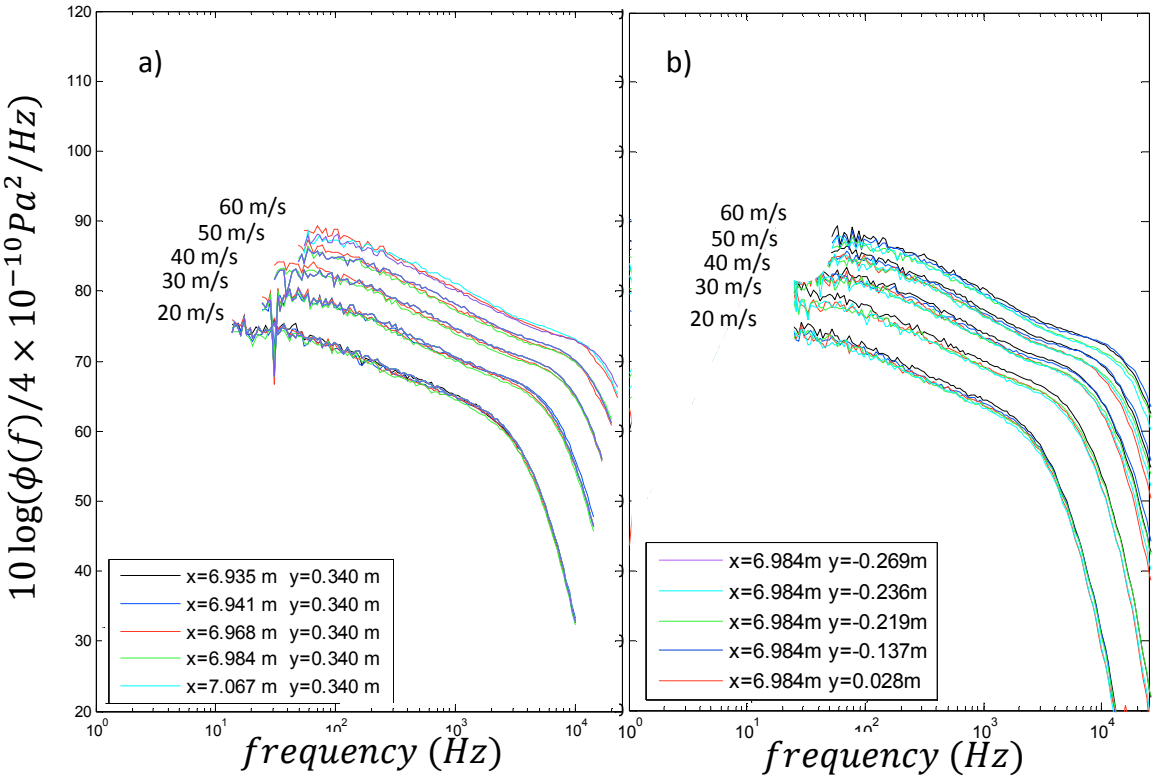

Figure 34: Homogeneity of the smooth wall pressure fluctuations at each test speed for the streamwise a) and spanwise b) locations

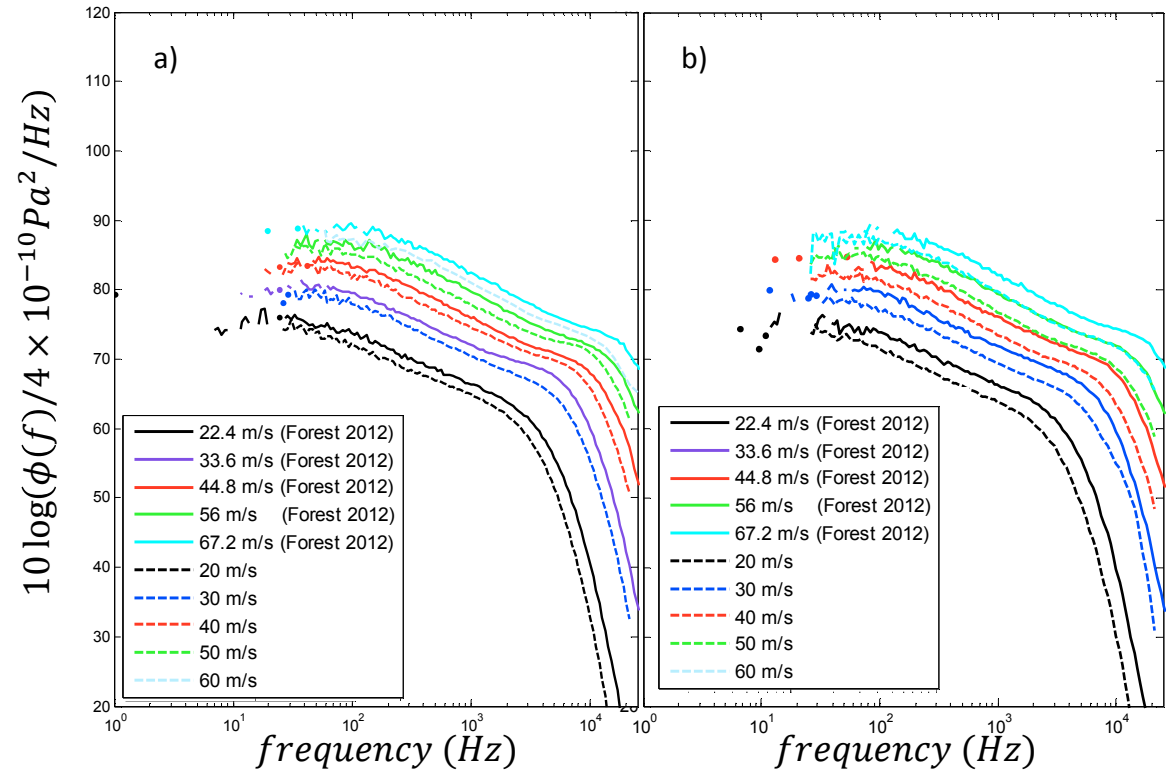

Figure 35: The smooth wall pressure spectra at each test speed compared to Forest's (2012) smooth wall pressure spectra at slightly different test speeds for the streamwise a) and spanwise b) locations.

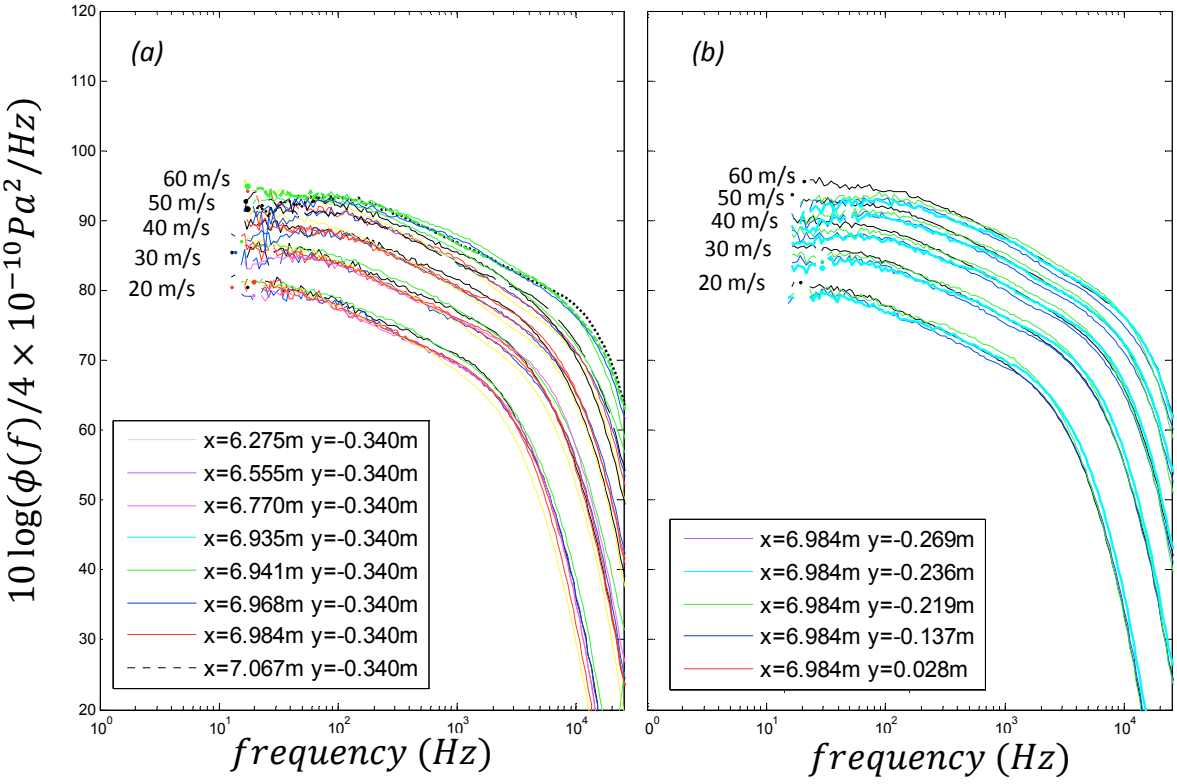

Figure 36: 1-mm roughness auto spectra at each speed for the (*a*) streamwise and (*b*) spanwise microphone rows

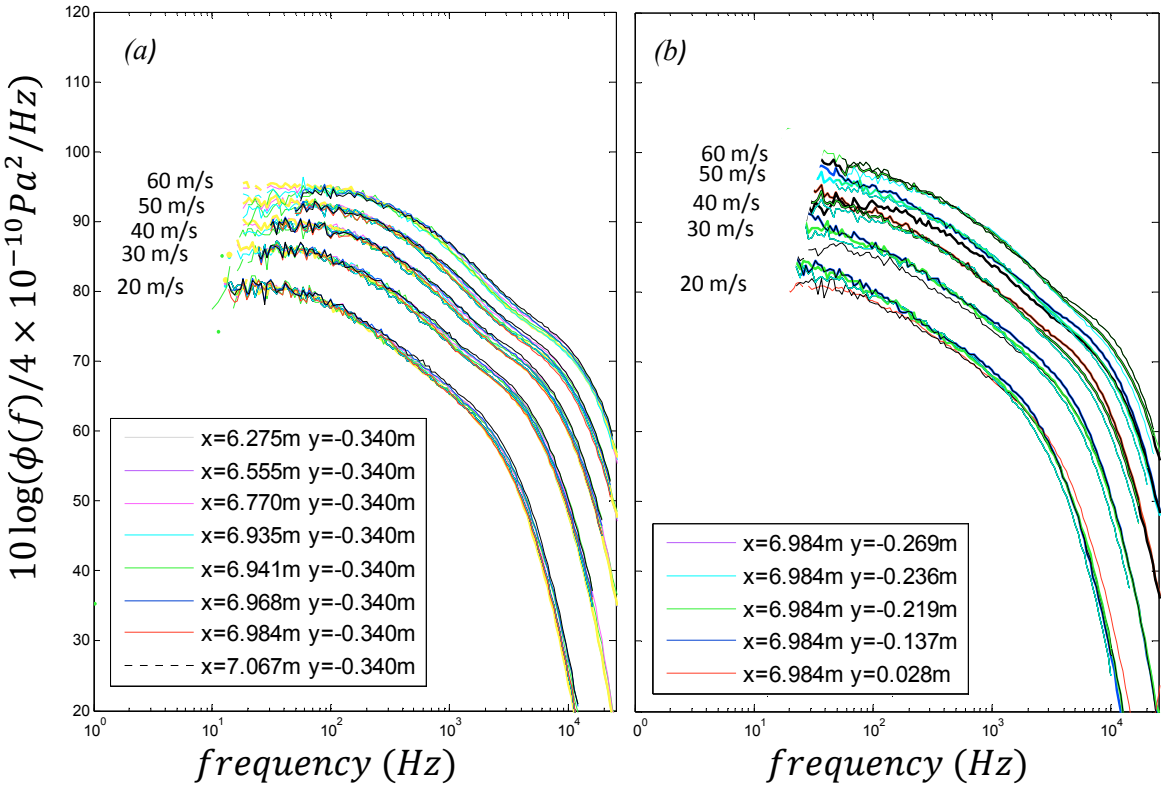

Figure 37: Random 3-mm roughness auto spectra at each speed for the (*a*) streamwise and (*b*) spanwise microphone rows

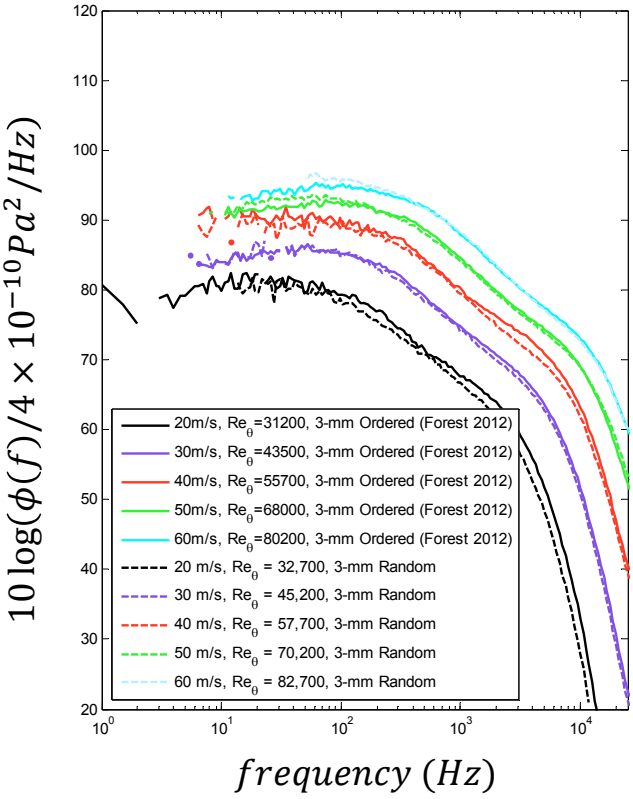

Figure 38. Comparison surface pressure spectra for the 3-mm random roughness with Forest's (2012) results for the 3-mm ordered roughness

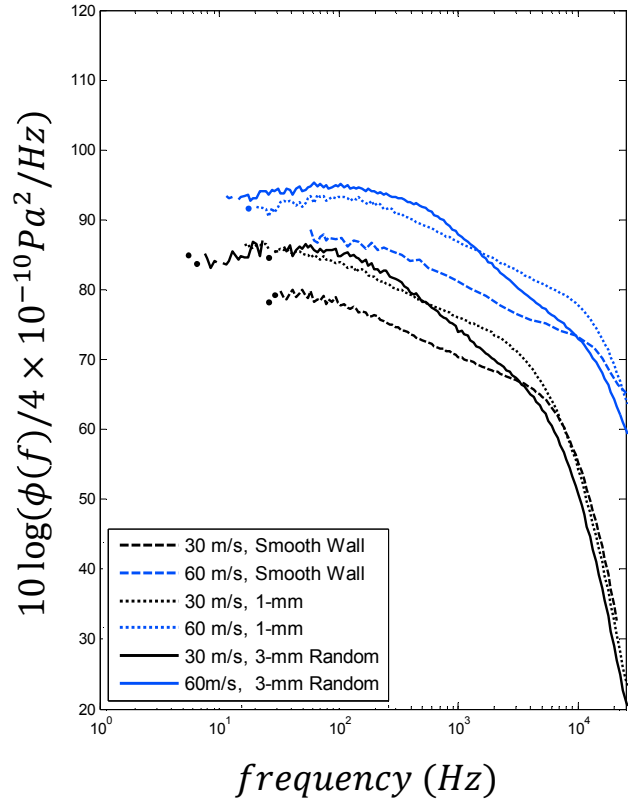

Figure 39: Effects of the surface condition on the pressure spectrum for two test speeds

Figure 40: Legend for rough wall studies analyzed in Figures 41 through 53 where A&L refers to Aupperle and Lambert (1970)

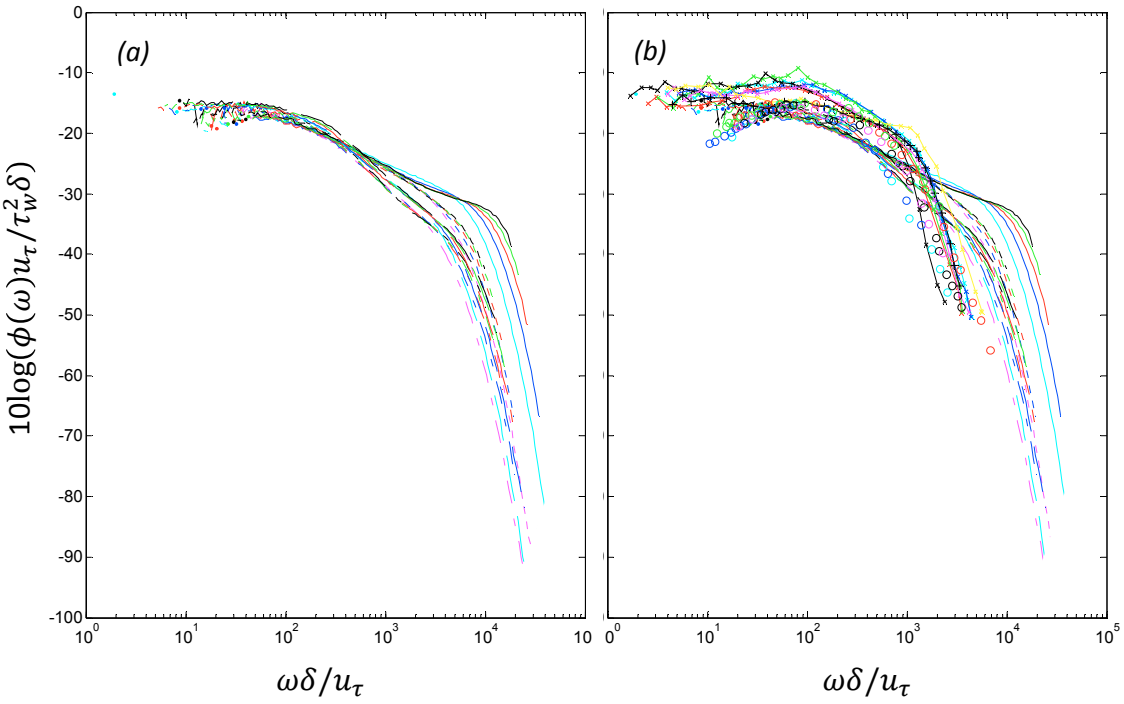

Figure 41: Classical outer scaling applied to (a) smooth and rough wall data from Forest (2012), and the present study, and (b) the data of Blake (1970), Forest (2010), Varano (2010) and the present study.

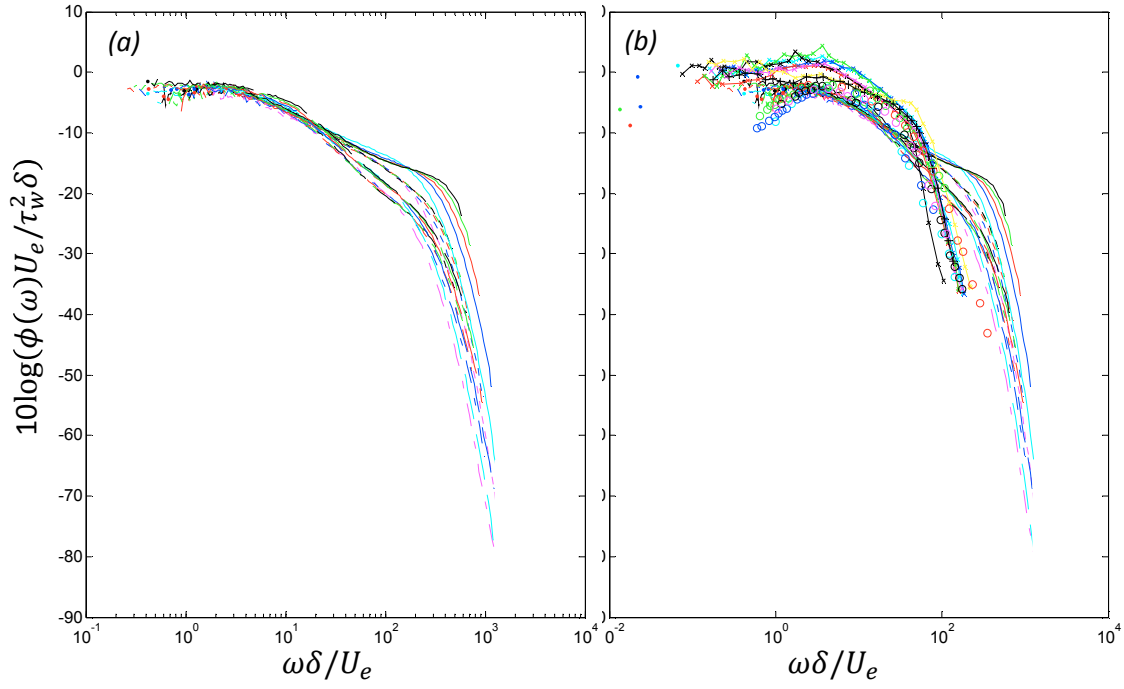

Figure 42: Outer scaling based on U_e, δ, and τ_w applied to (a) smooth and rough wall data from Forest (2012), and the present study, and (b) the data of Blake (1970), Forest (2010), Varano (2010) and the present study.

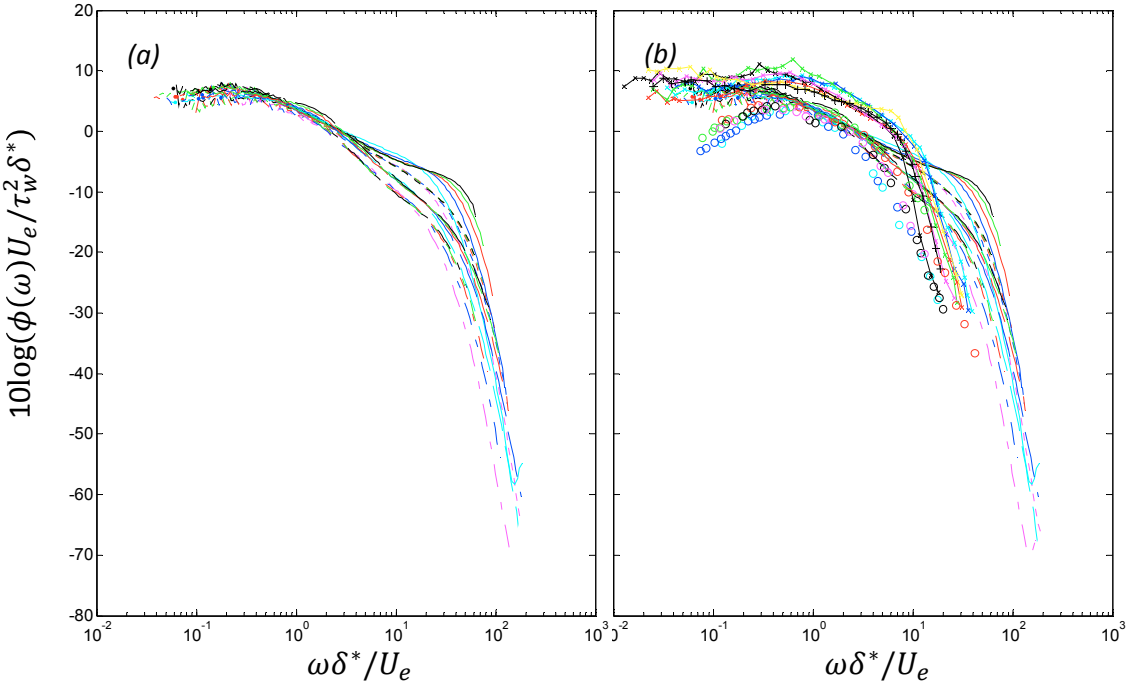

Figure 43: Mixed outer scaling applied to (a) smooth and rough wall data from Forest (2012), and the present study, and (b) the data of Blake (1970), Forest (2010), Varano (2010) and the present study.

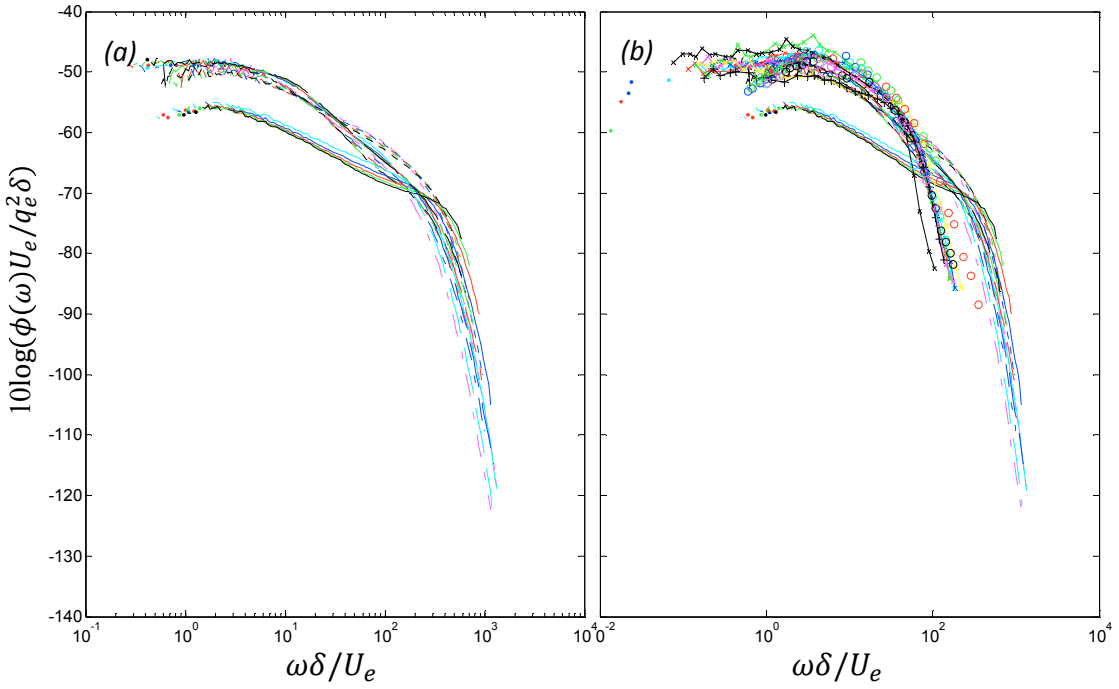

Figure 44: Outer scaling based on U_e, δ, and q_e applied to (a) smooth and rough wall data from Forest (2012), and the present study, and (b) the data of Blake (1970), Forest (2010), Varano (2010) and the present study

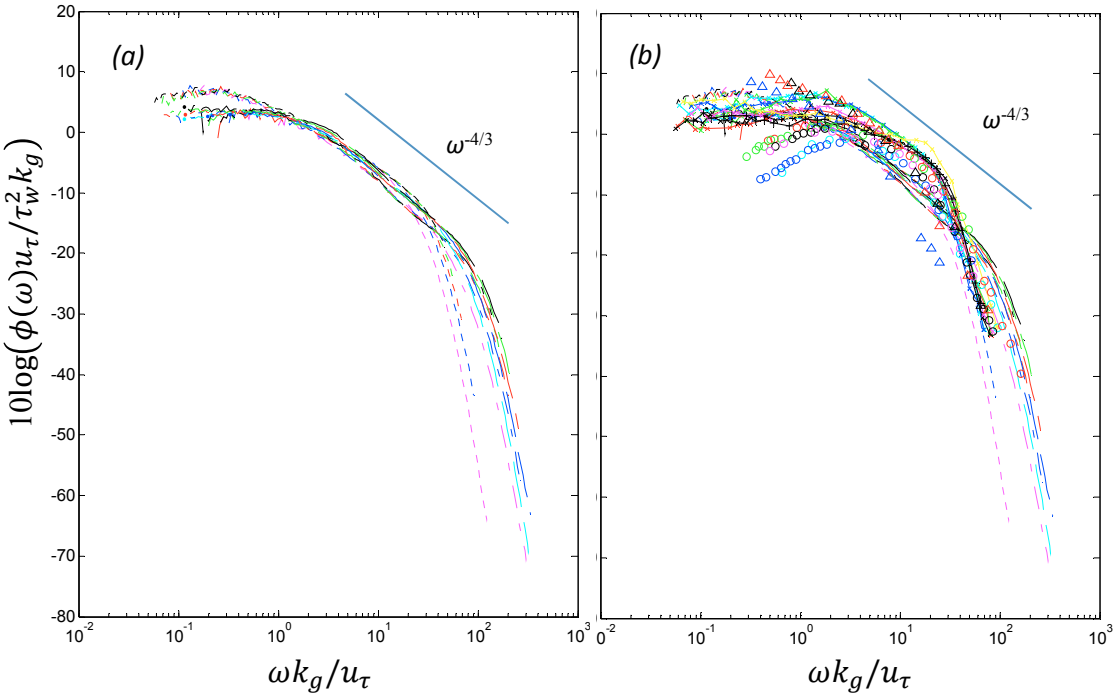

Figure 45: Blake's roughness scaling applied to data from (a) Forest (2012), and the present study, and (b) Blake (1970), Aupperle and Lambert (1970), Varano (2010), Forest (2012), and the present study.

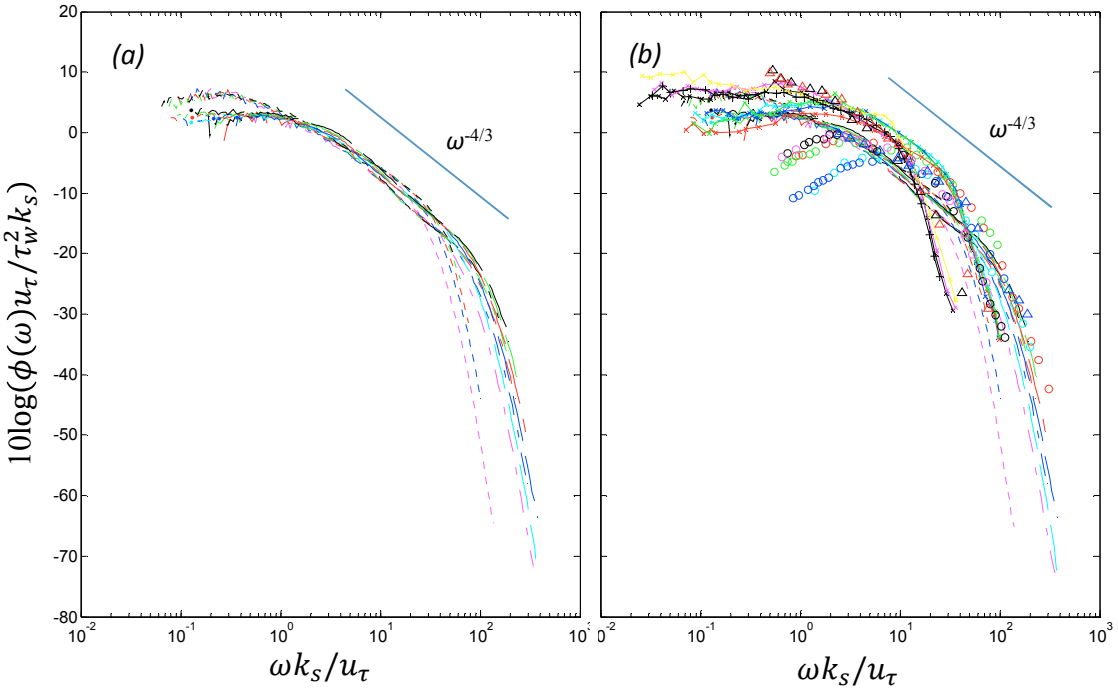

Figure 46: Blake's modified roughness scaling on k_s applied to data from (a) Forest (2012) and the present study, and (b) Blake (1970), Aupperle and Lambert (1970), Varano (2010), Forest (2012), and the present study.

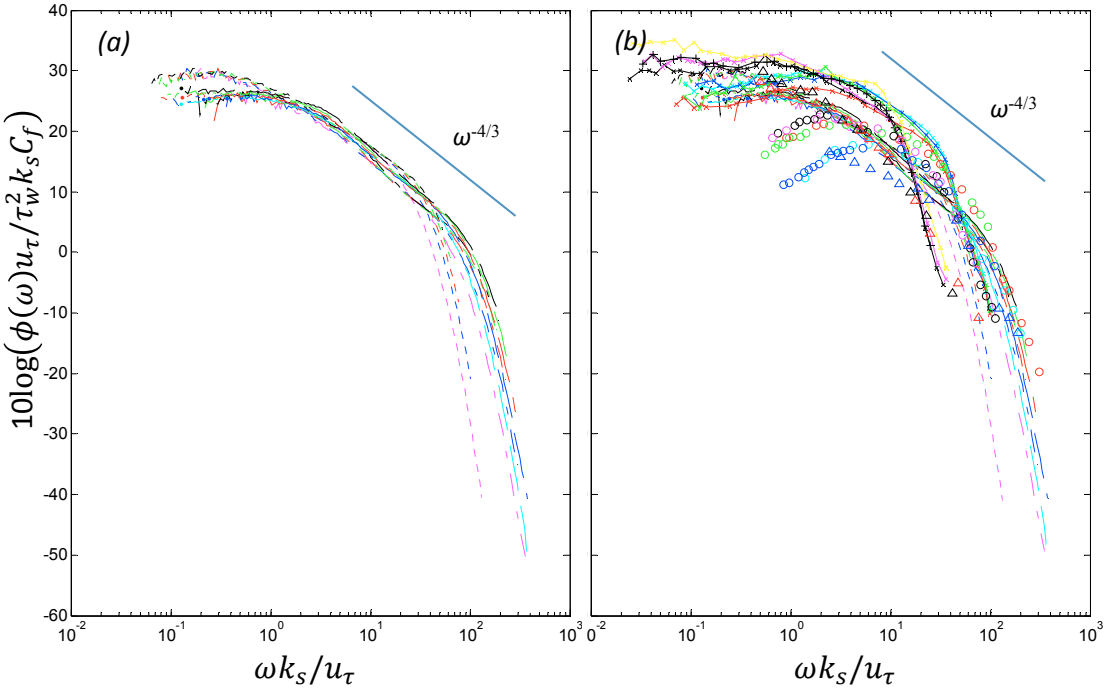

Figure 47: Aupperle and Lambert's (1970) scaling applied to data from (a) Forest (2012), and the present study , and (b) Blake (1970), Varano (2010), Forest (2012), and the present study.

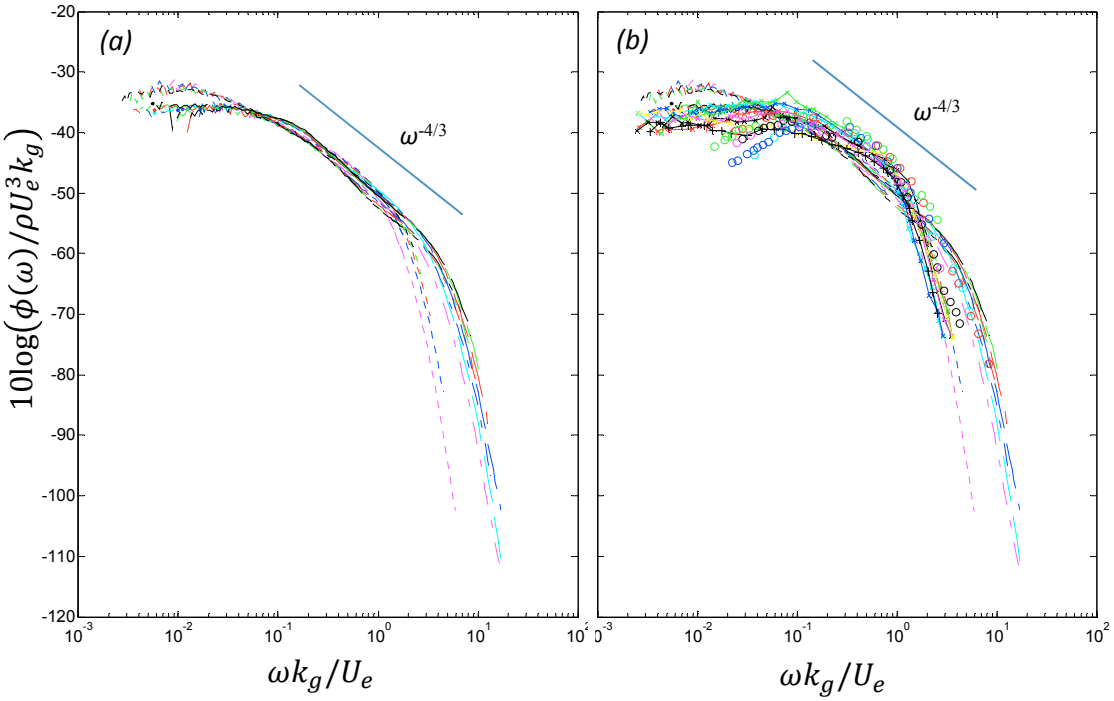

Figure 48: Varano's roughness scaling applied to data from (a) Forest (2012), and the present study, and (b) Blake (1970), Varano (2010), Forest (2012), and the present study.

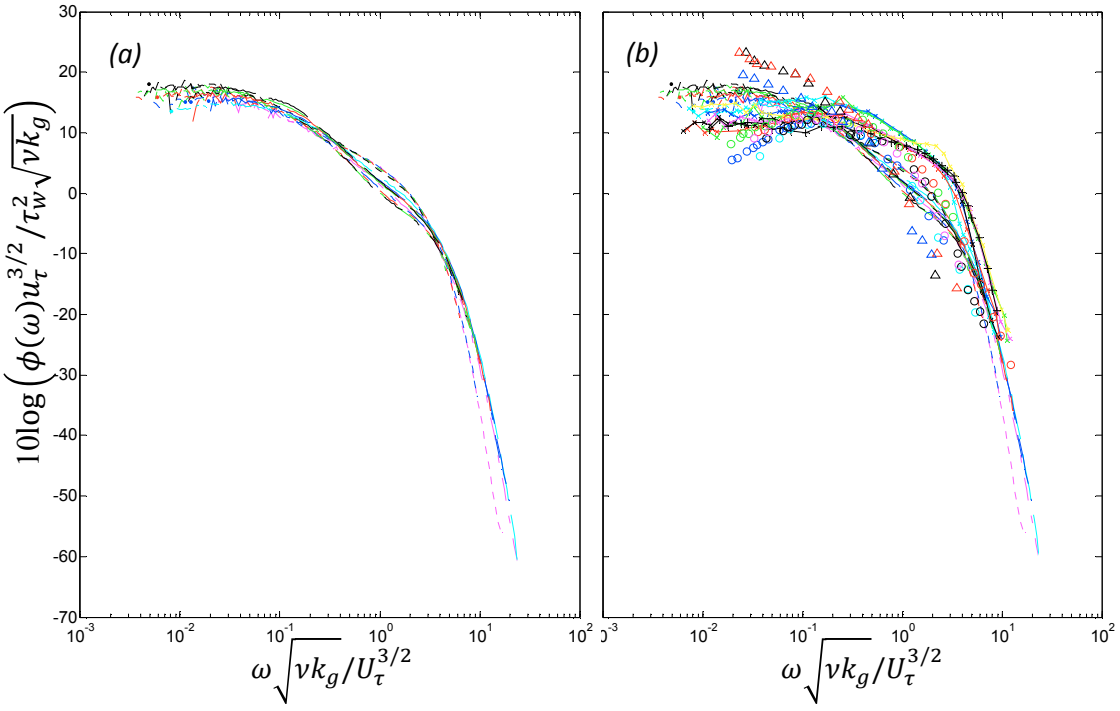

Figure 49: Forest's (2012) roughness scaling on k_g for data from (a) Forest (2012), and the present study, and (b) Blake (1970), Aupperle and Lambert (1970), Forest (2012), Varano (2010) and the present study.

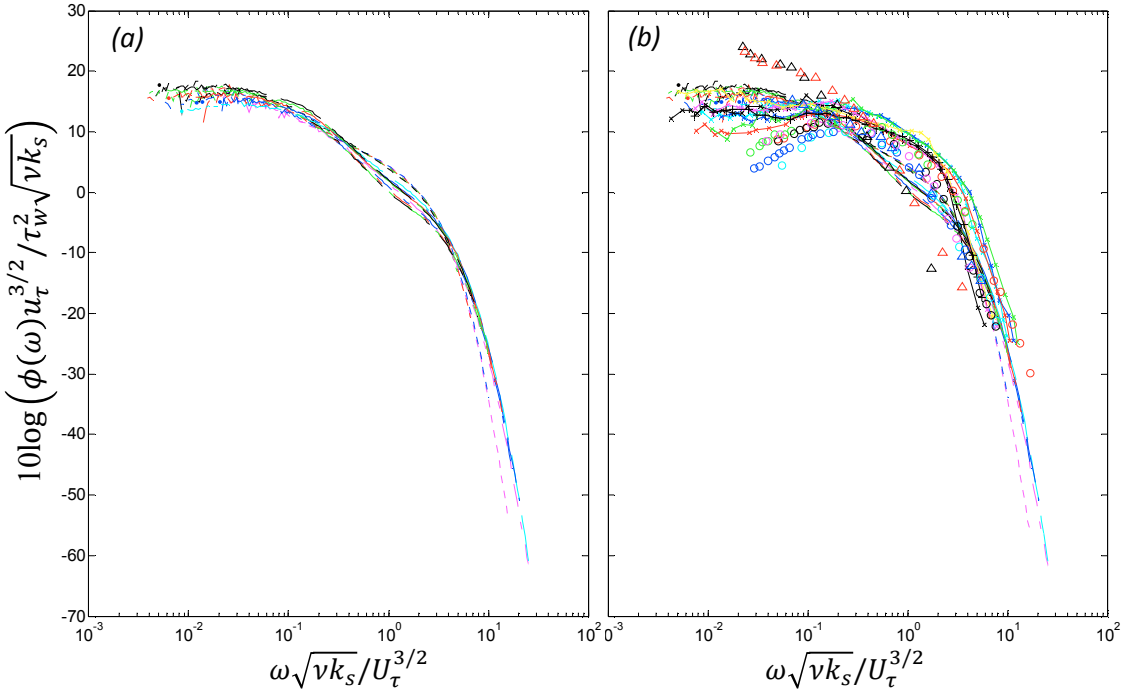

Figure 50: Forest's (2012) modified roughness scaling on k_s for data from (a) Forest (2012), and the present study, and (b) Blake (1970), Aupperle and Lambert (1970), Varano (2010) Forest (2012), and the present study.

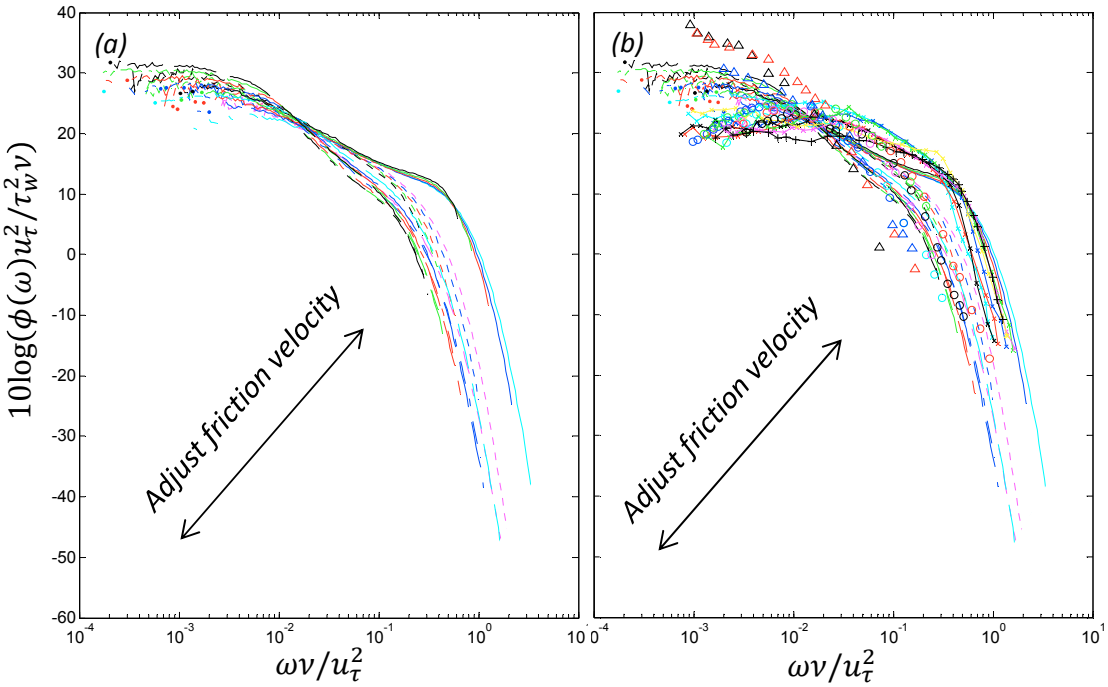

Figure 51: Rough wall pressure spectra scaled on smooth wall inner variables for (a) Forest (2012) and the present study's data, and (b) Blake (1970), Aupperle and Lambert (1970), Varano (2012), Forest (2012), and the present study.

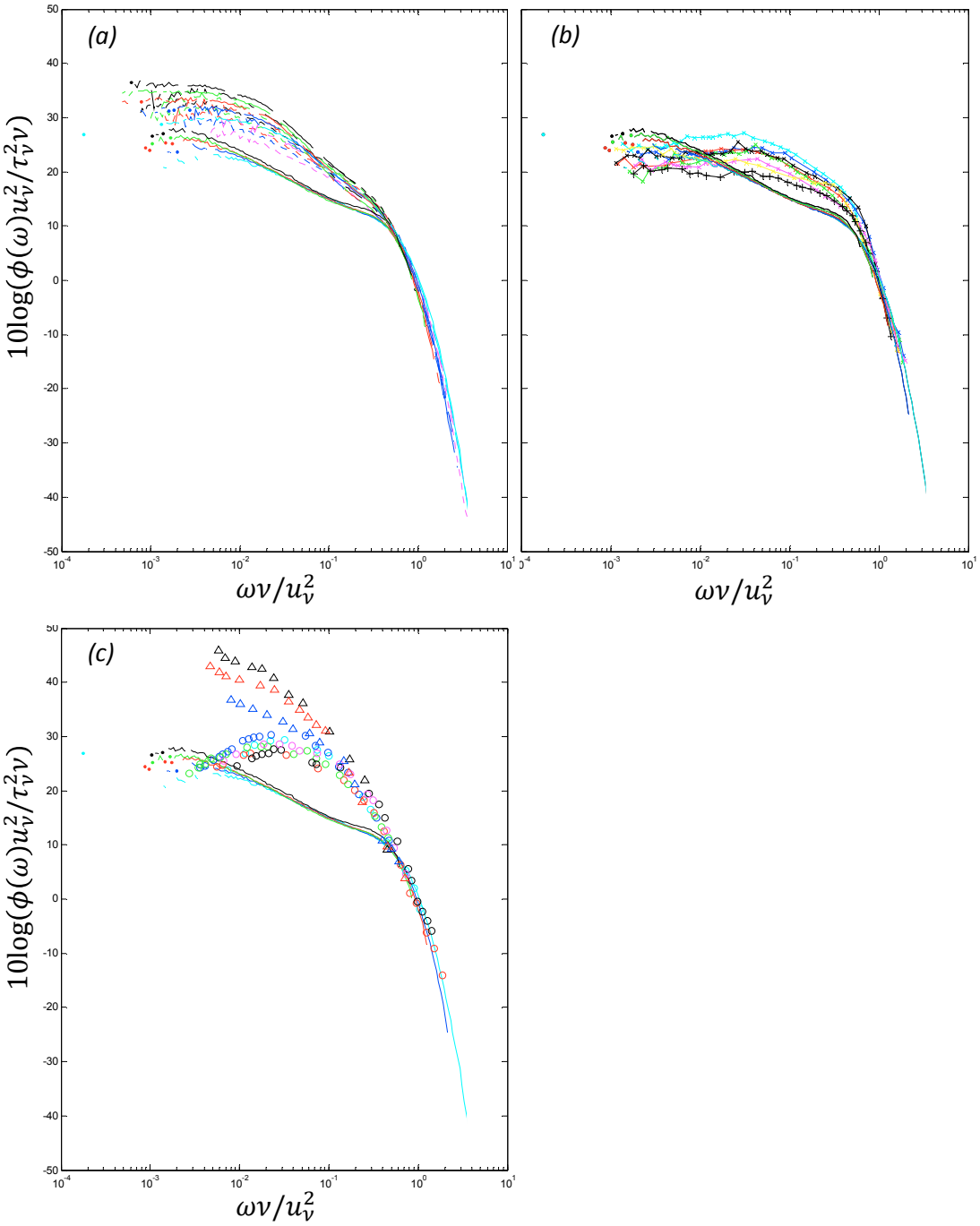

Figure 52: The unified high frequency viscous scaling applied to data from (a) Forest (2012) and the present study, (b) Varano (2010) , and (c) Blake (1970) and Aupperle and Lambert (1971).

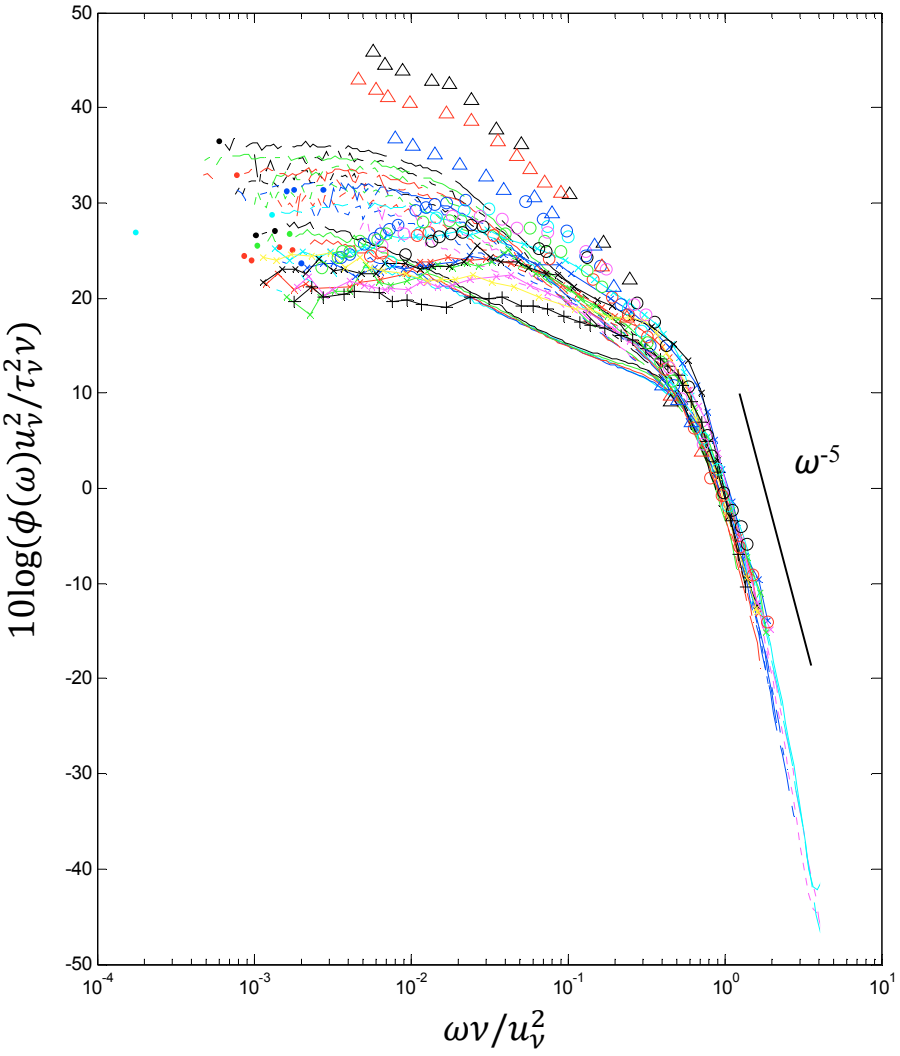

Figure 53: The unified high frequency viscous scaling applied to data from Blake (1970) and Aupperle and Lambert (1970), Varano (2010), Forest (2012) and the present study.

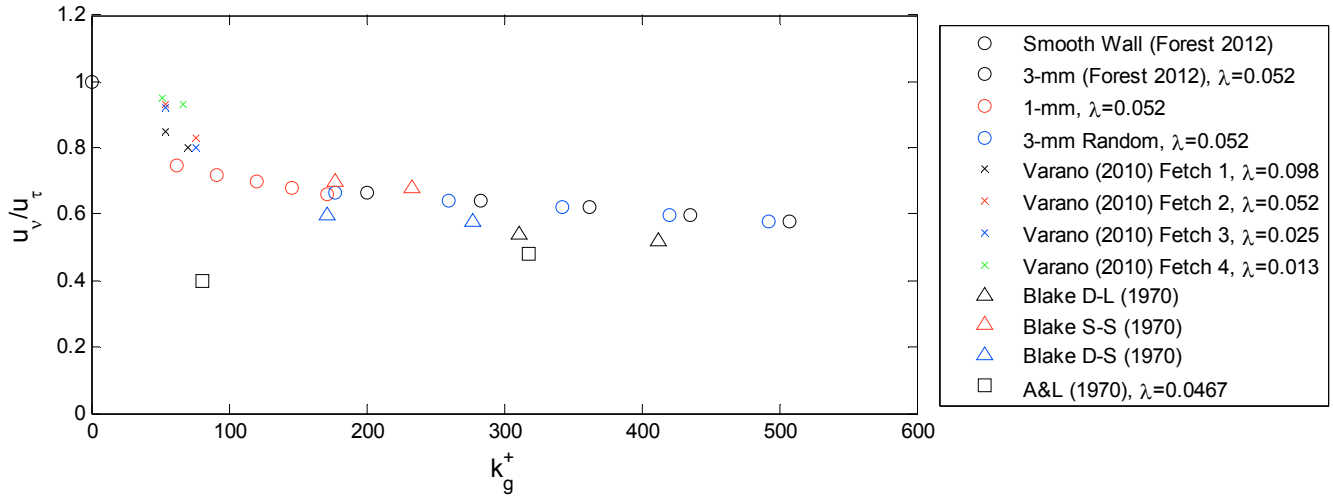

Figure 54: Ratio of friction velocities determined from pressure spectra from the present flows (λ=0.052) compared with Aupperle and Lambert's (1971), λ=0.0467, and Blake (1970) and Varano's (2010) varying sparseness ratios.

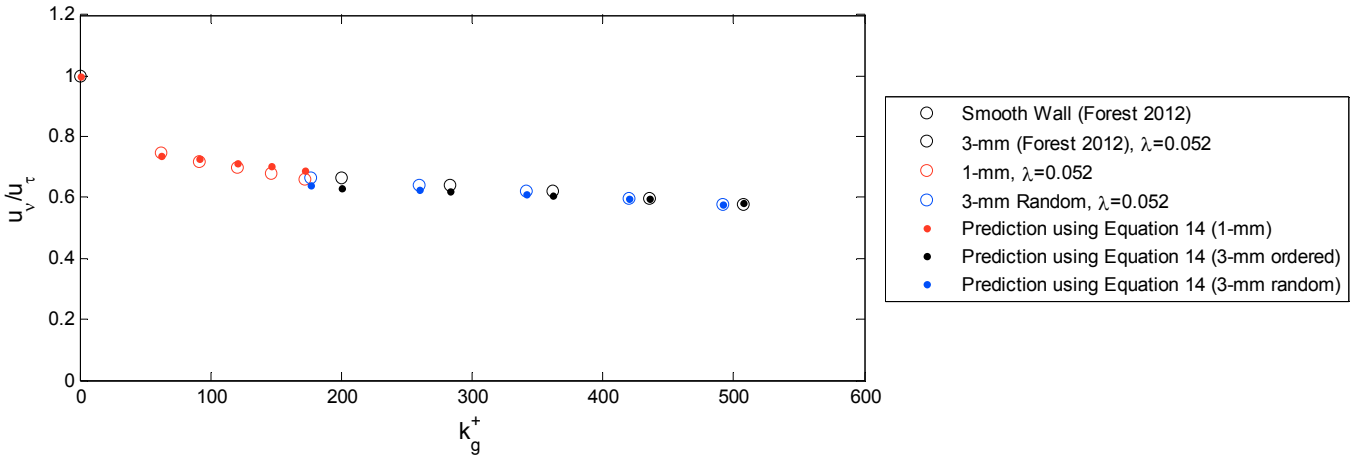

Figure 55: Ratio of friction velocities estimated using Equation 14 compared to the ratio of friction velocities determined from the pressure spectra for the present study and that of Forest's (2012)

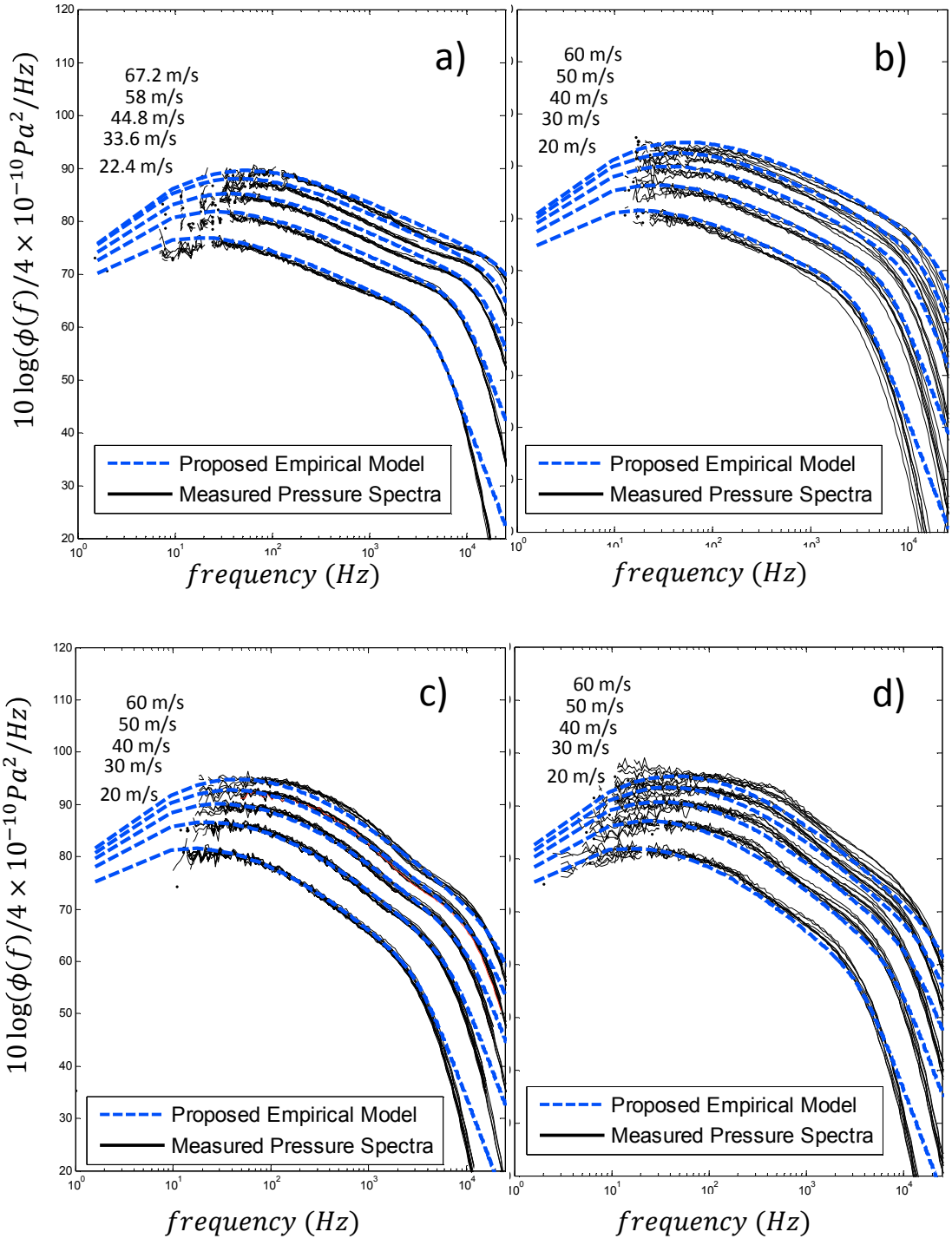

Figure 56: Spectral predictions using Equation 17 of Forest's (2012) smooth wall (a), the 1-mm ordered (b), Forest's (2012) 3-mm ordered (c) and the 3-mm random (d) rough surface conditions for each test speed overlaid on a darkened figure of the spectral measurements.

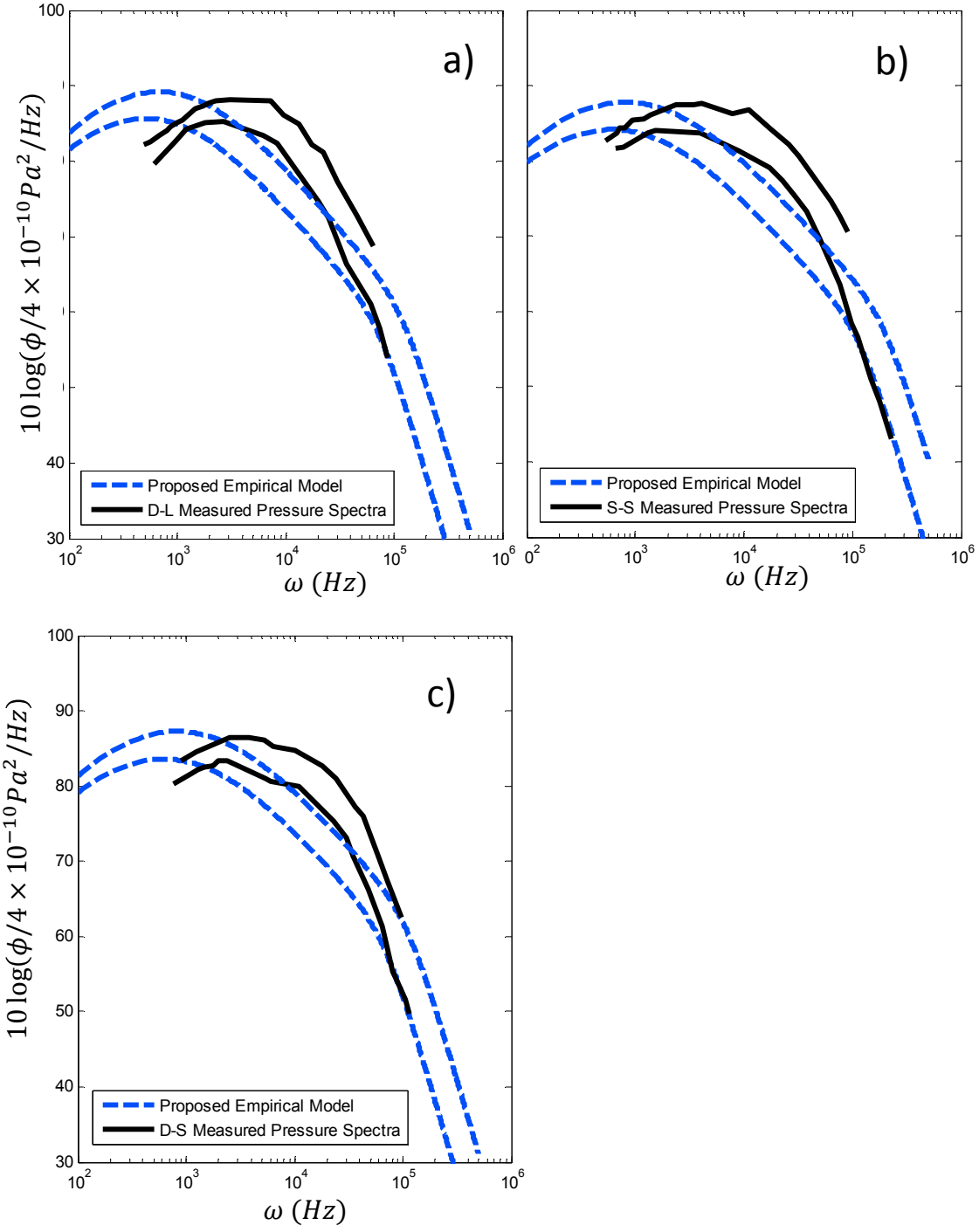

Figure 57: Spectral predictions using Equation 17 of Blakes's (1971) rough wall pressure spectra for the D-L (a), S-S (b), and D-S (c) surface conditions at 38 and 50 m/s overlaid on a darkened figure of the spectral measurements.

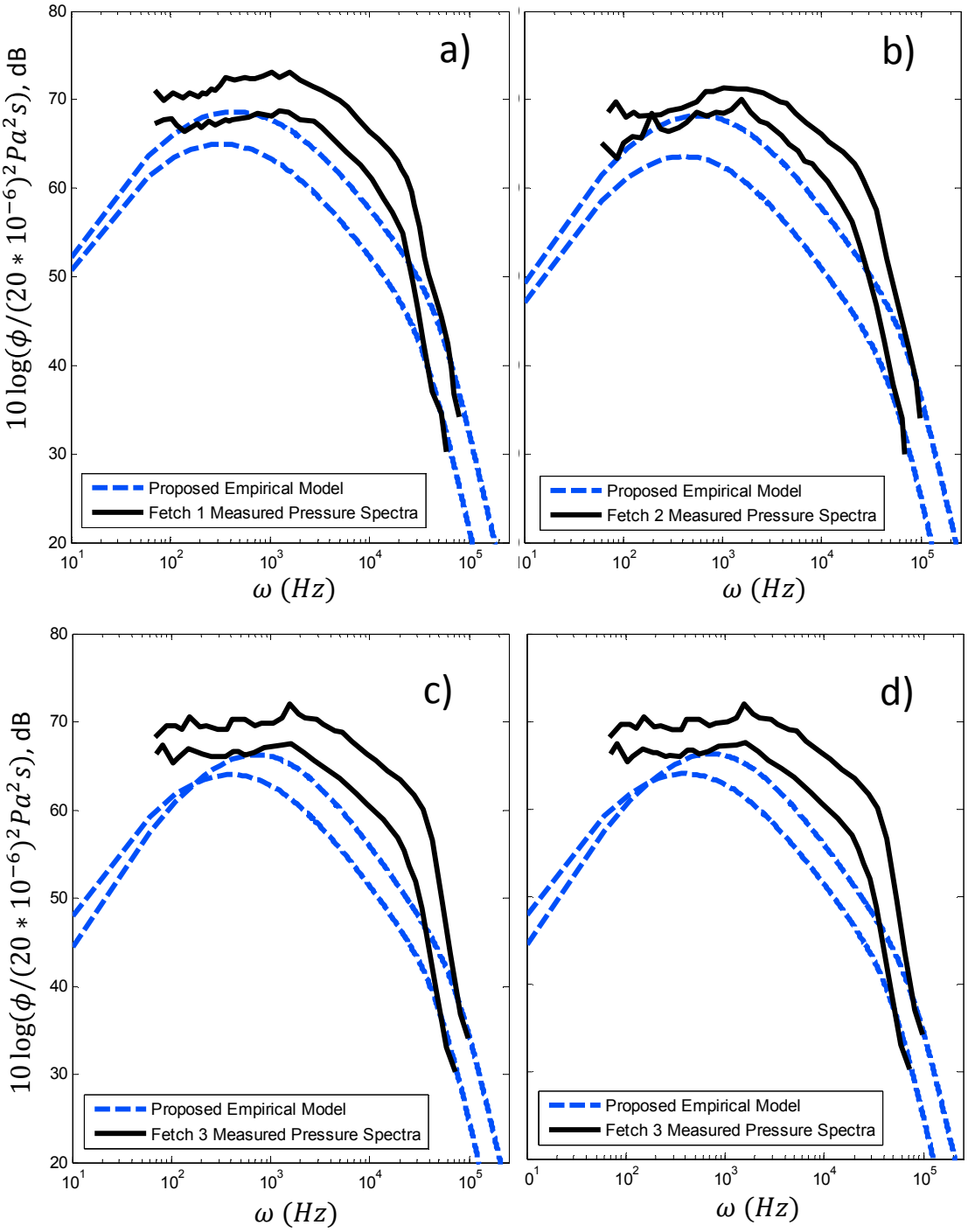

Figure 58: Spectral predictions using Equation 17 of Varano's (2010) rough wall pressure spectra for Fetch 1 (a), Fetch 2 (b), Fetch 3 (c), and Fetch 4 (d) at 20.5 and 27.5 m/s overlaid on a darkened figure of the spectral measurements.

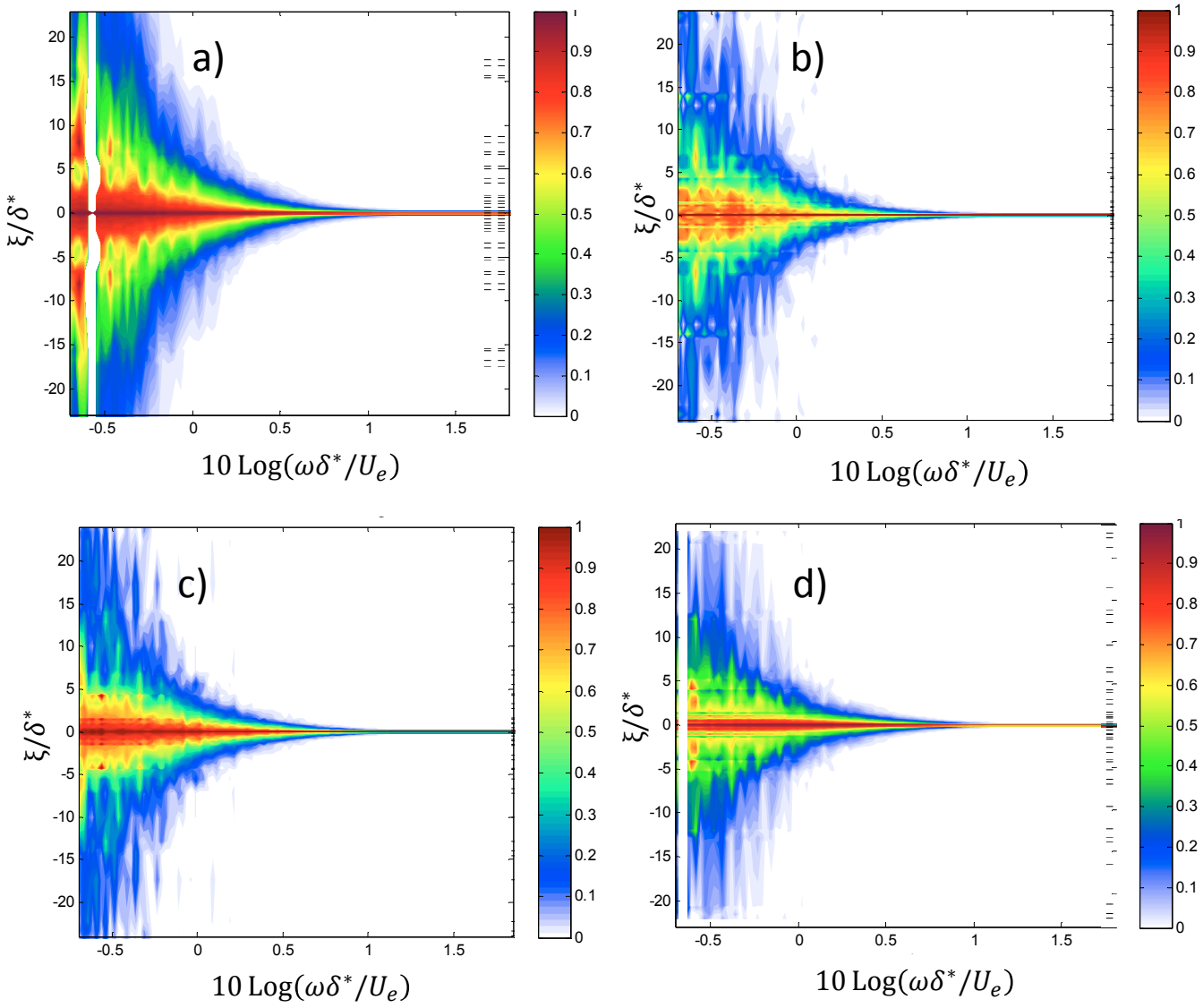

Figure 59: Mapped streamwise coherence for Forest's (2012) smooth wall (a) at 33.6 m/s, the ordered 1-mm roughness (b), the random 3-mm roughness (c), and Forest's (2012) ordered 3-mm roughness (d) at 30 m/s.

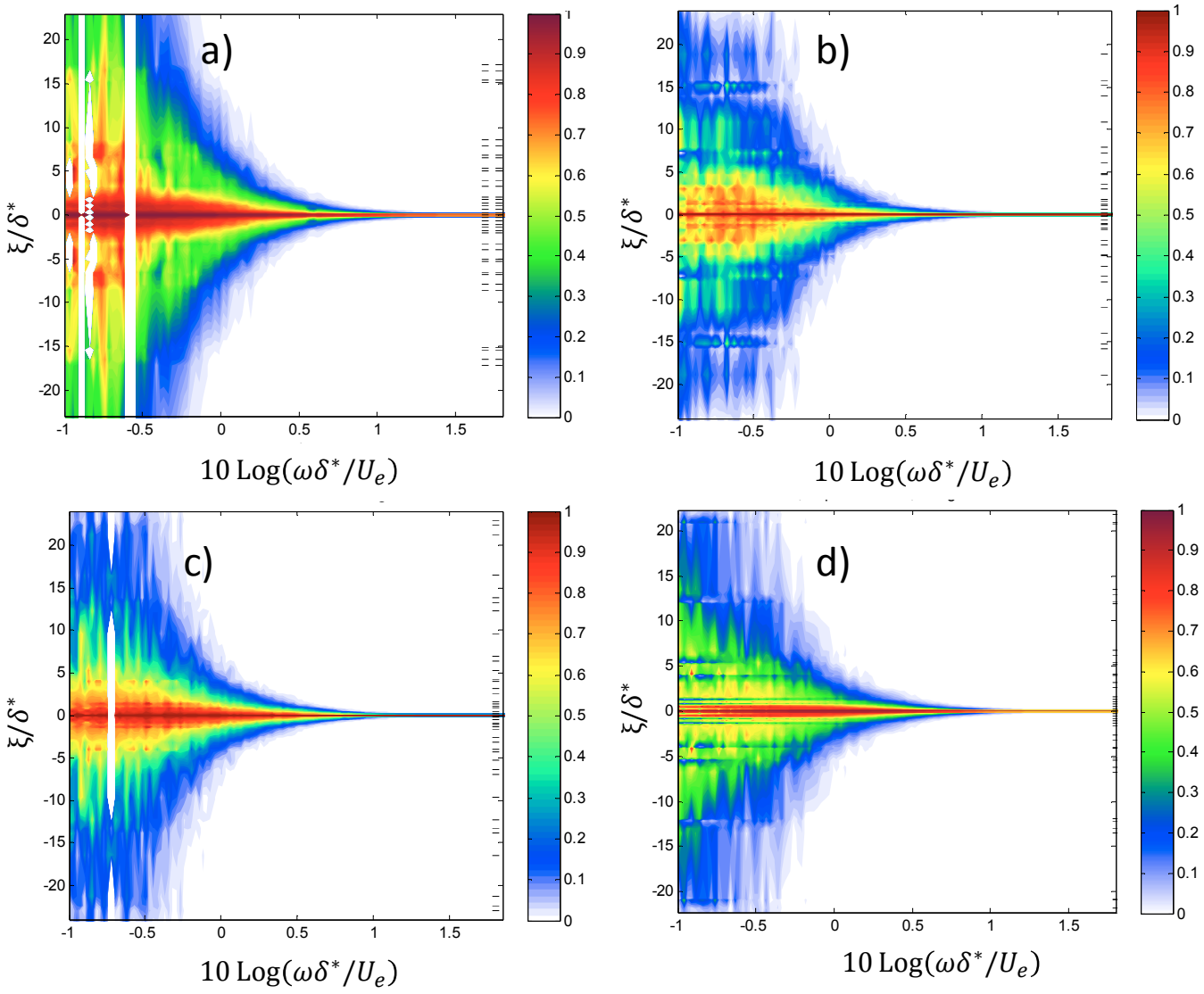

Figure 60: Mapped streamwise coherence for Forest's (2012) smooth wall (a) at 67.2 m/s, the ordered 1-mm roughness (b), the random 3-mm roughness (c), and Forest's (2012) ordered 3-mm roughness (d) at 60 m/s.

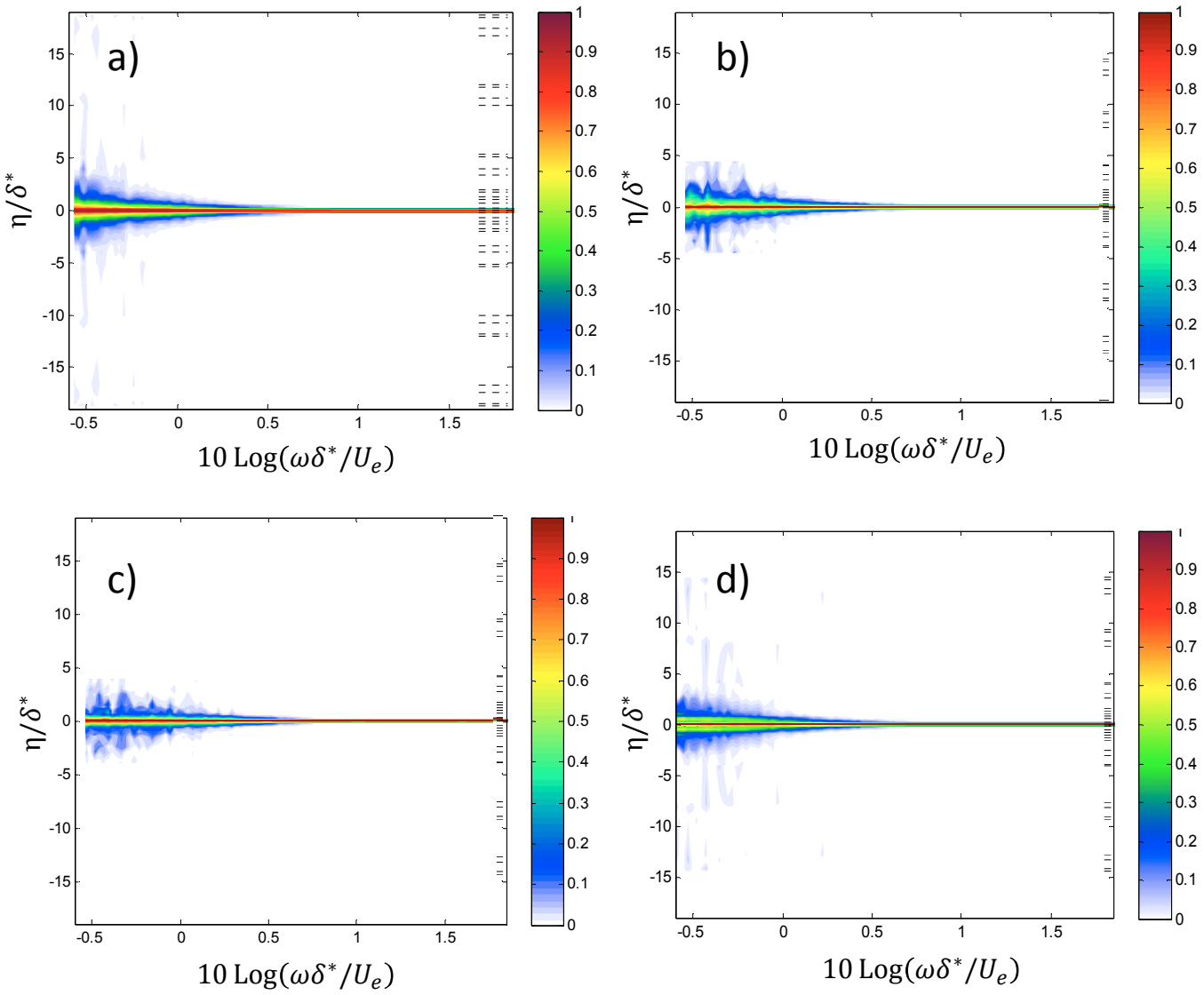

Figure 61: Mapped spanwise coherence for Forest's (2012) smooth wall (a) at 33.6 m/s, the ordered 1-mm roughness (b), the random 3-mm roughness (c), and Forest's (2012) ordered 3-mm roughness (d) at 30 m/s.

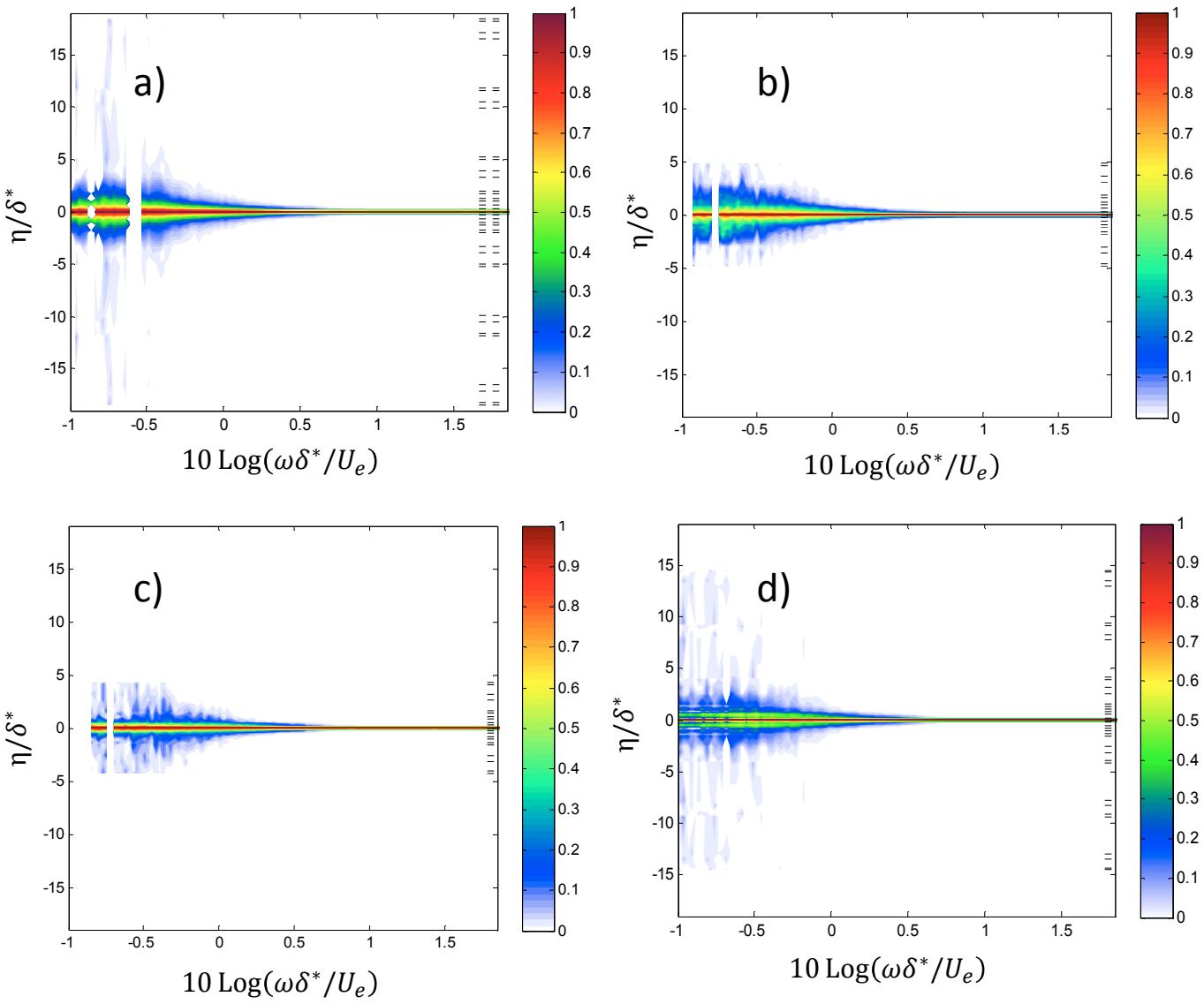

Figure 62: Mapped spanwise coherence for Forest's (2012) smooth wall (a) at 67.2 m/s, the ordered 1-mm roughness (b), the random 3-mm roughness (c), and Forest's (2012) ordered 3-mm roughness (d) at 60 m/s.

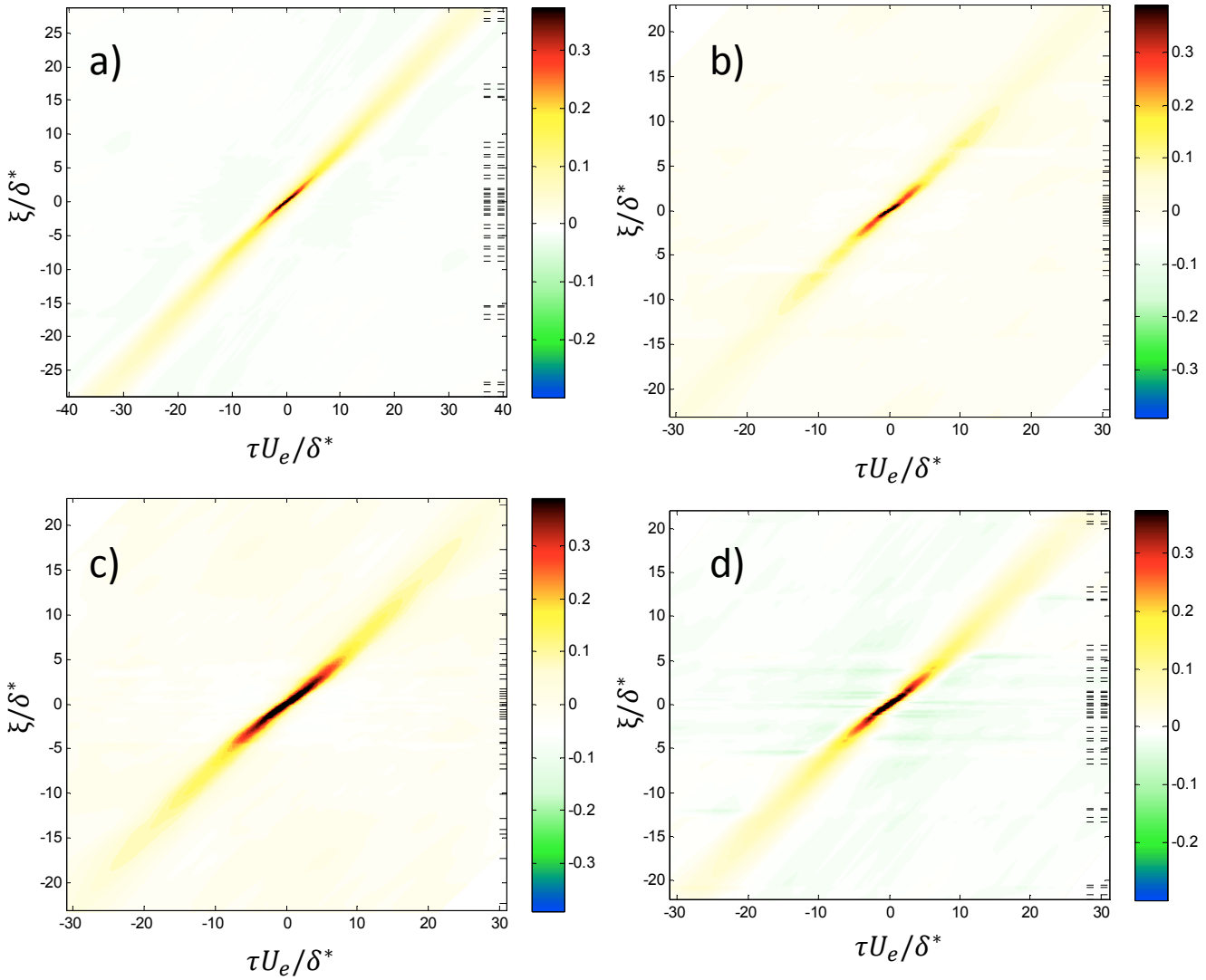

Figure 63: Mapped streamwise correlation for Forest's (2012) smooth wall (a) at 33.6 m/s, the ordered 1-mm roughness (b), the random 3-mm roughness (c), and Forest's (2012) ordered 3-mm roughness (d) at 30 m/s.

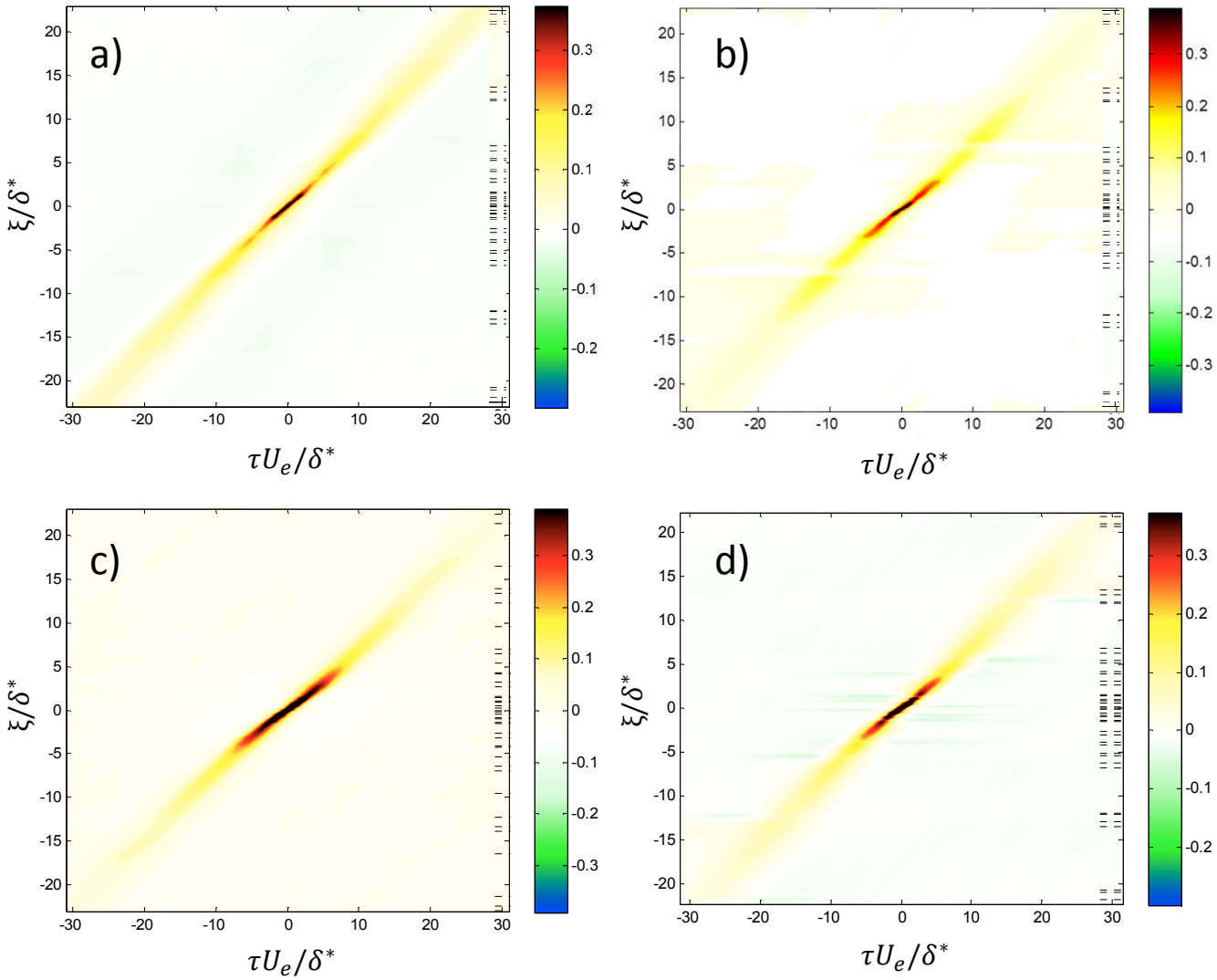

Figure 64: Mapped streamwise correlation for Forest's (2012) smooth wall (a) at 67.2 m/s, the ordered 1-mm roughness (b), the random 3-mm roughness (c), and Forest's (2012) ordered 3-mm roughness (d) at 60 m/s.

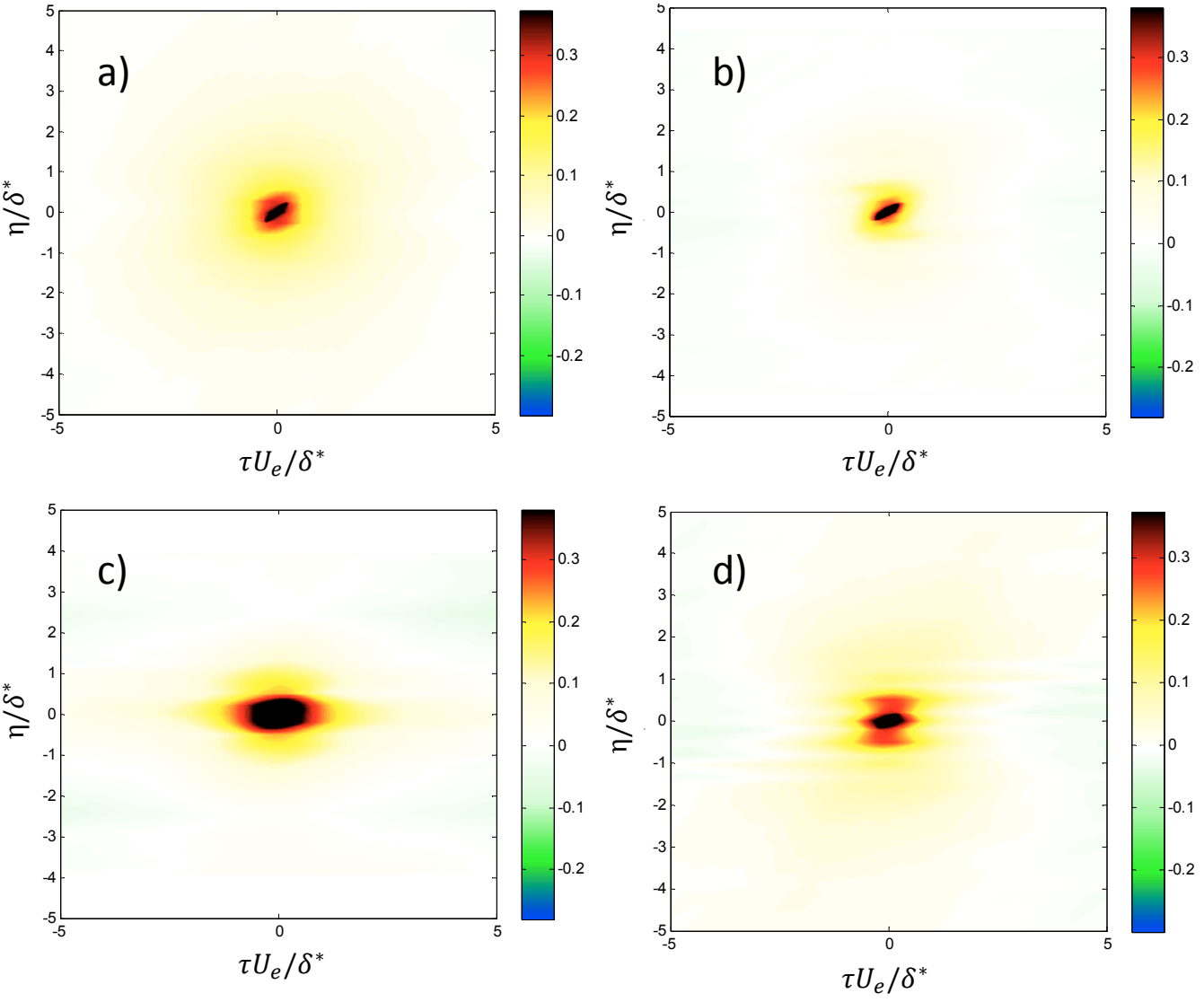

Figure 65: Mapped spanwise coherence for Forest's (2012) smooth wall (a) at 33.6 m/s, the ordered 1-mm roughness (b), the random 3-mm roughness (c), and Forest's (2012) ordered 3-mm roughness (d) at 30 m/s.

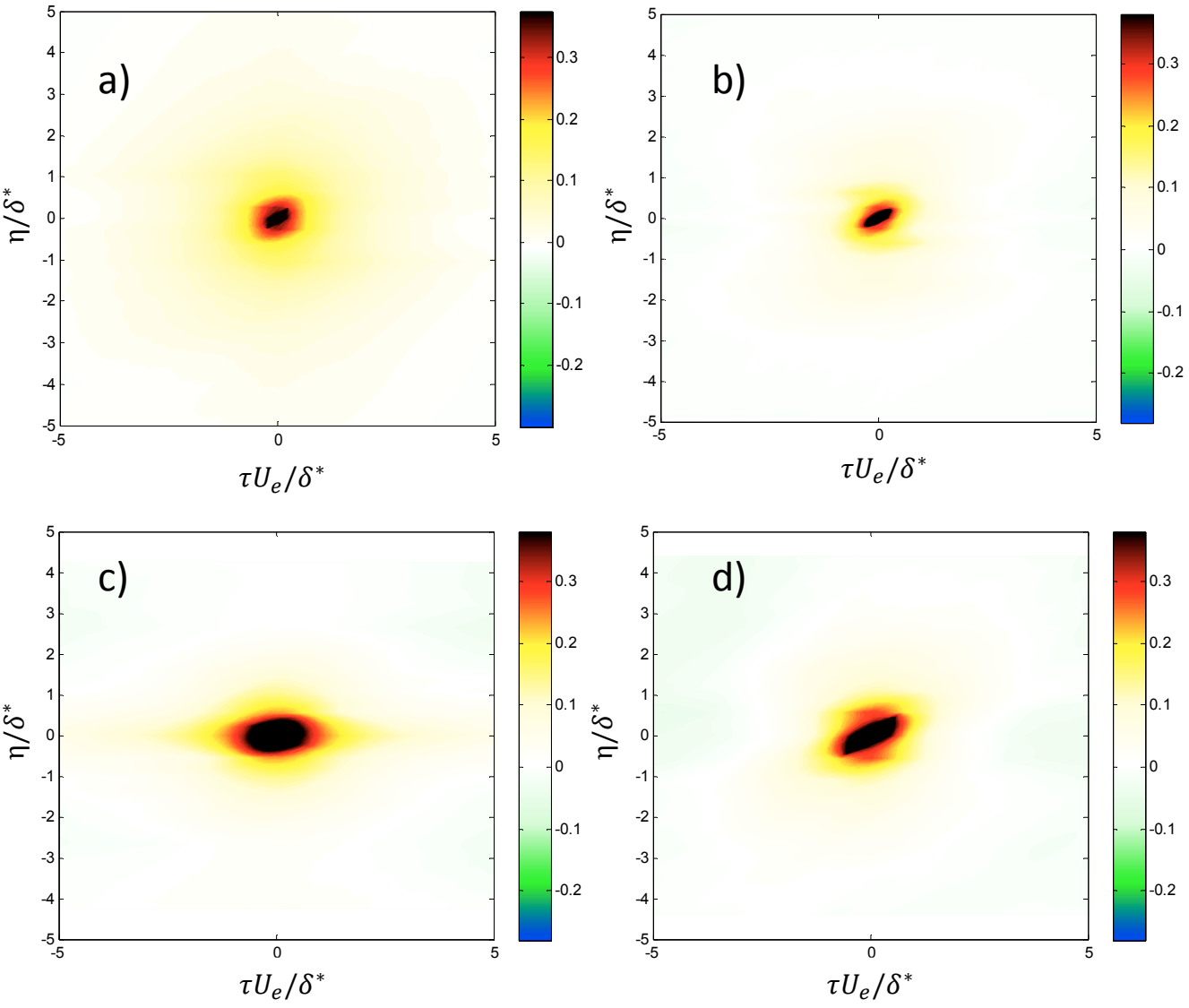

Figure 66: Mapped spanwise coherence for Forest's (2012) smooth wall (a) at 67.2 m/s, the ordered 1-mm roughness (b), the random 3-mm roughness (c), and Forest's (2012) ordered 3-mm roughness (d) at 60 m/s.

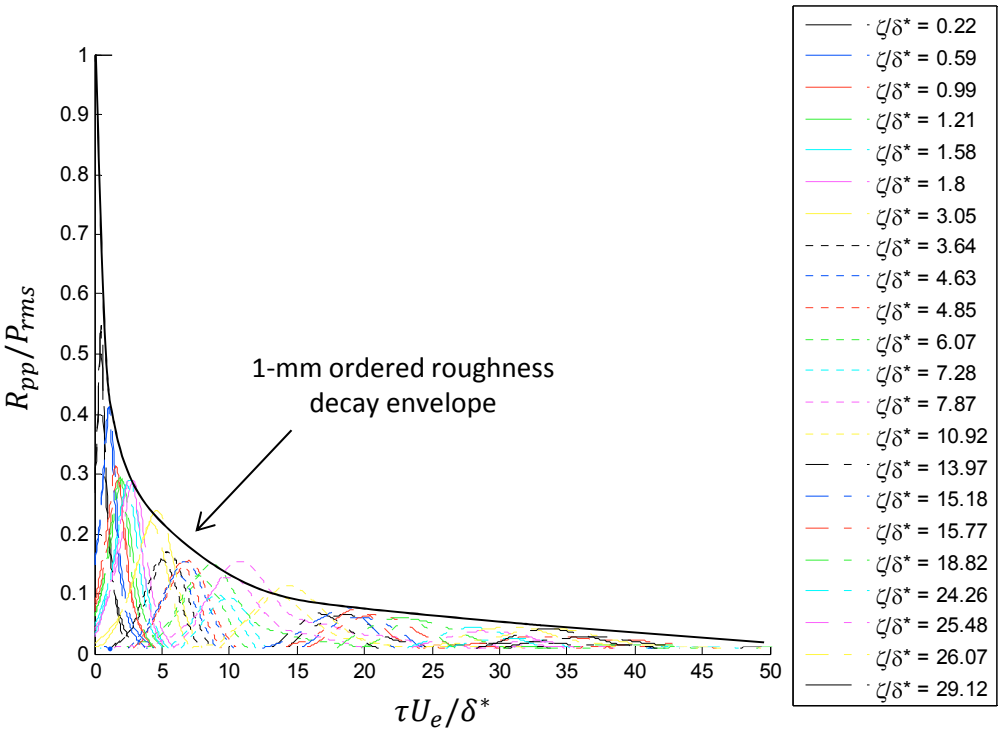

Figure 67: Rough wall pressure fluctuation streamwise correlation decay for the ordered 1-mm rough surface condition at 30 and 60 m/s.

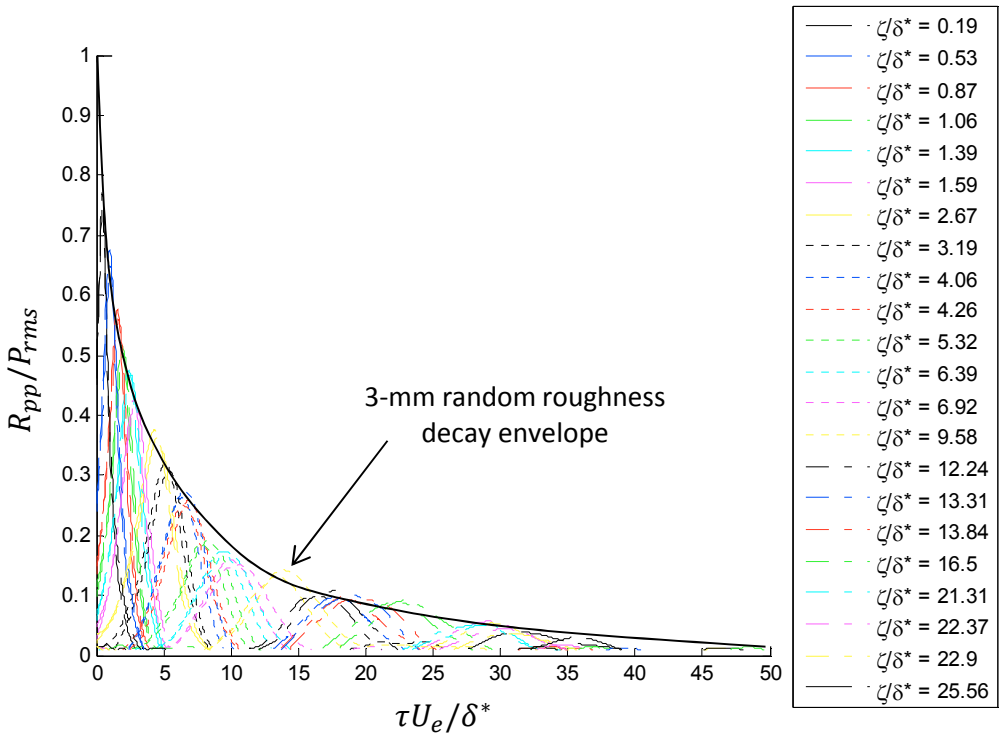

Figure 68: Rough wall pressure fluctuation streamwise correlation decay for the random 3-mm rough surface condition at 30 and 60 m/s.

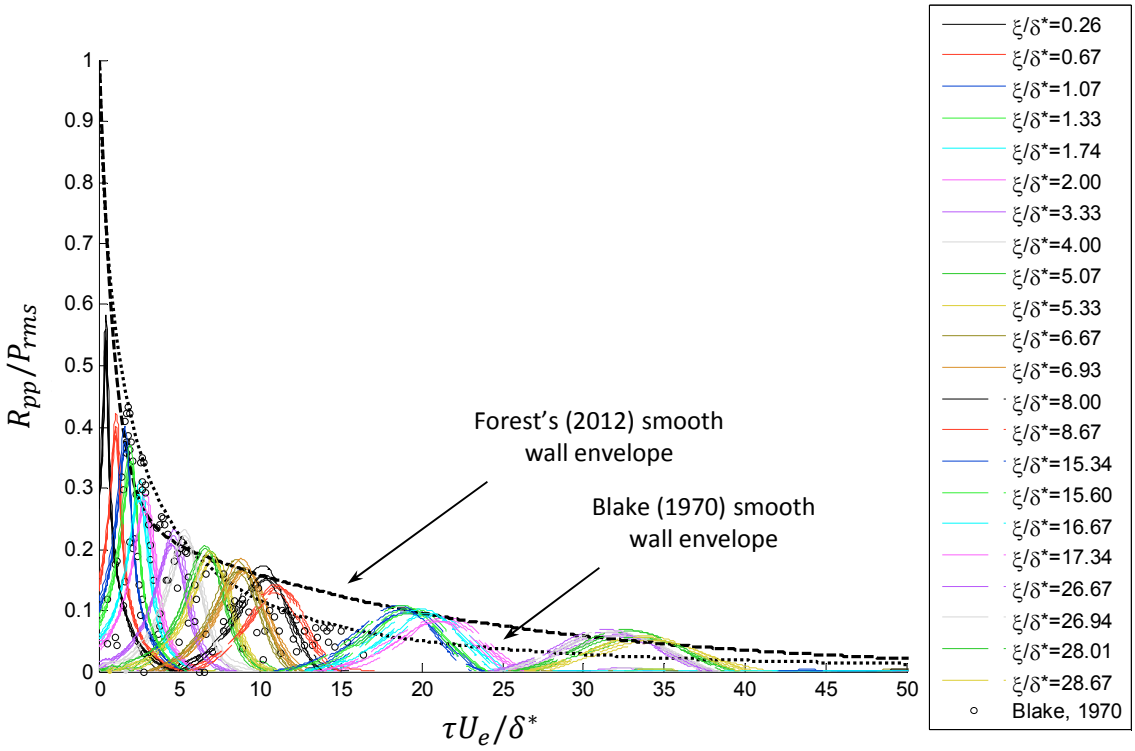

Figure 69: Forest's (2012) smooth wall surface pressure fluctuation streamwise correlation decay at 22.4, 33.6, 44.8, 56.0, 67.2 m/s for various separations.

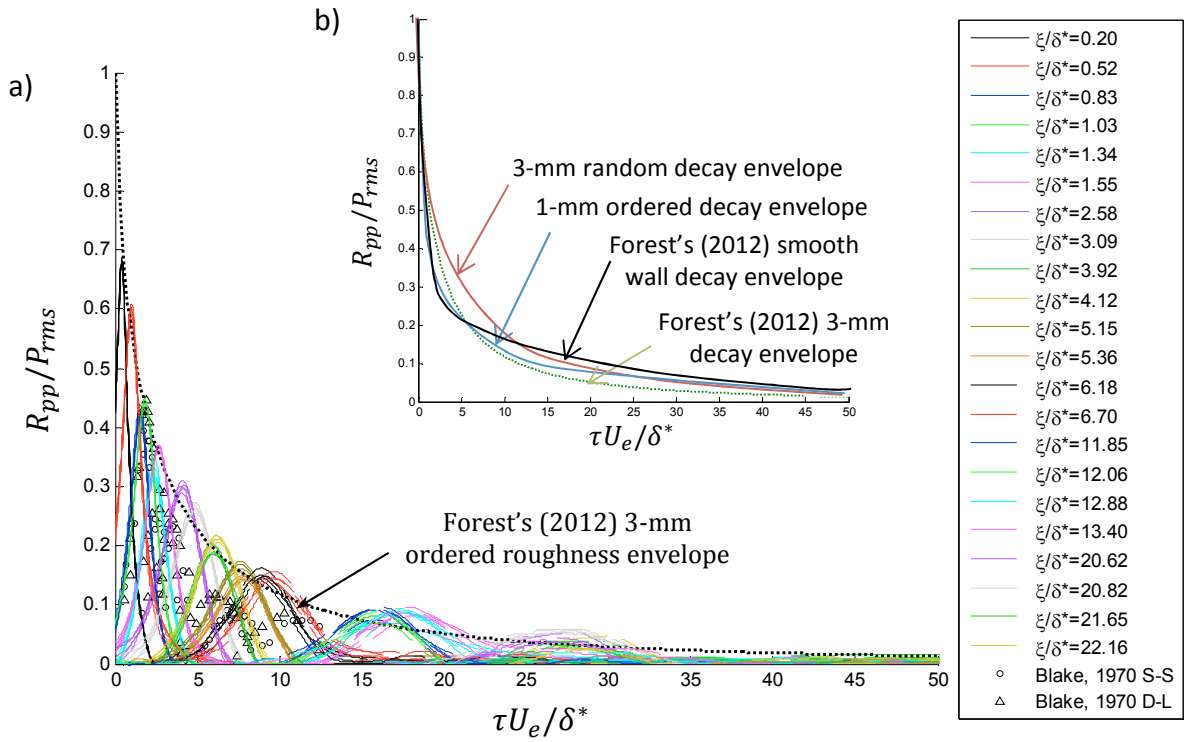

Figure 70: Forest's (2012) 3-mm ordered rough roughness wall pressure fluctuation streamwise correlation decay envelope at each test speed for the various separations a) and a comparison of the correlation decay envelopes for each surface condition b).

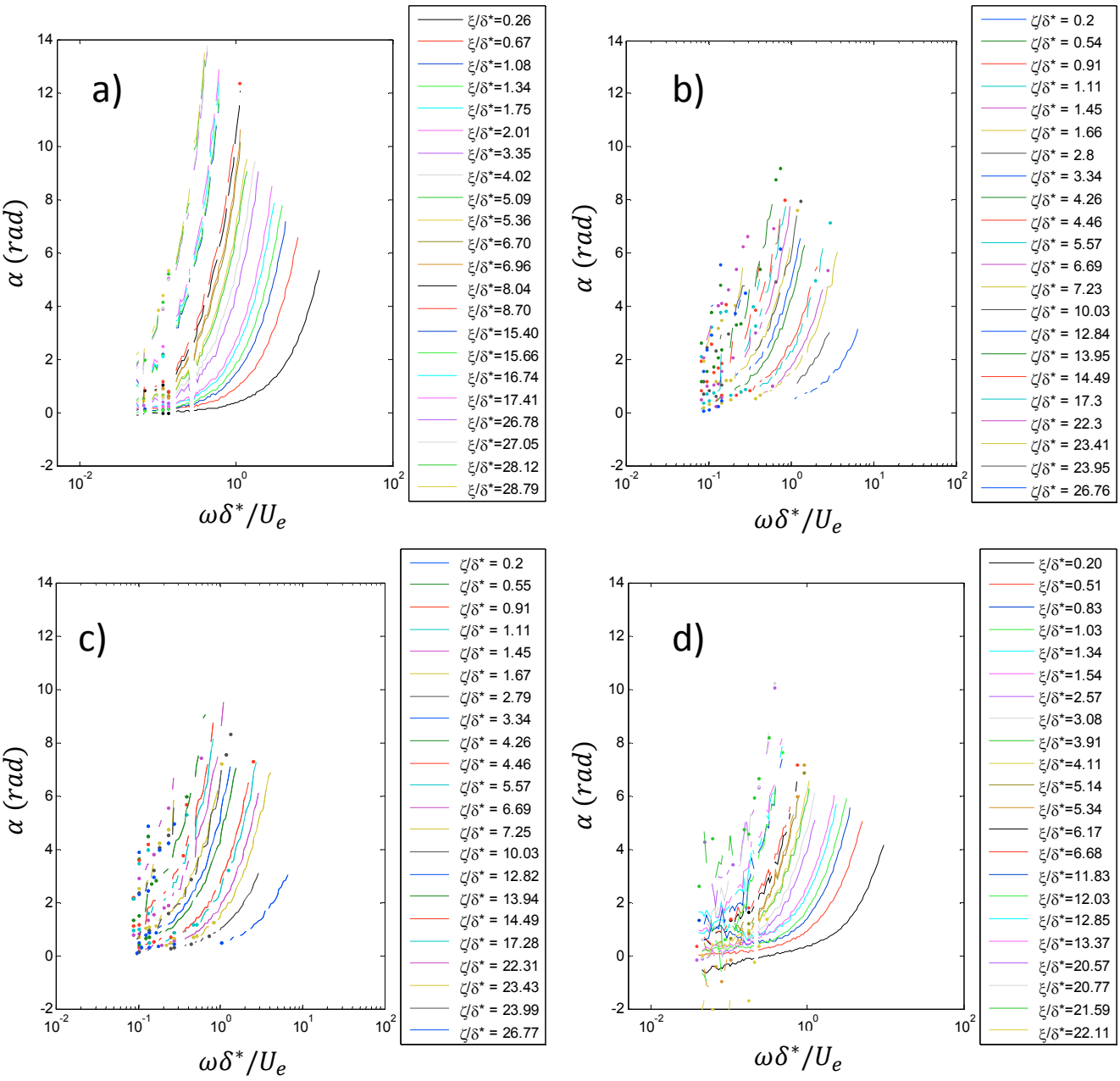

Figure 71: Streamwise phase angle for Forest's (2012) smooth wall (a) at 33.6 m/s, the ordered 1-mm roughness (b), the random 3-mm roughness (c), and Forest's (2012) ordered 3-mm roughness (d) at 30 m/s.

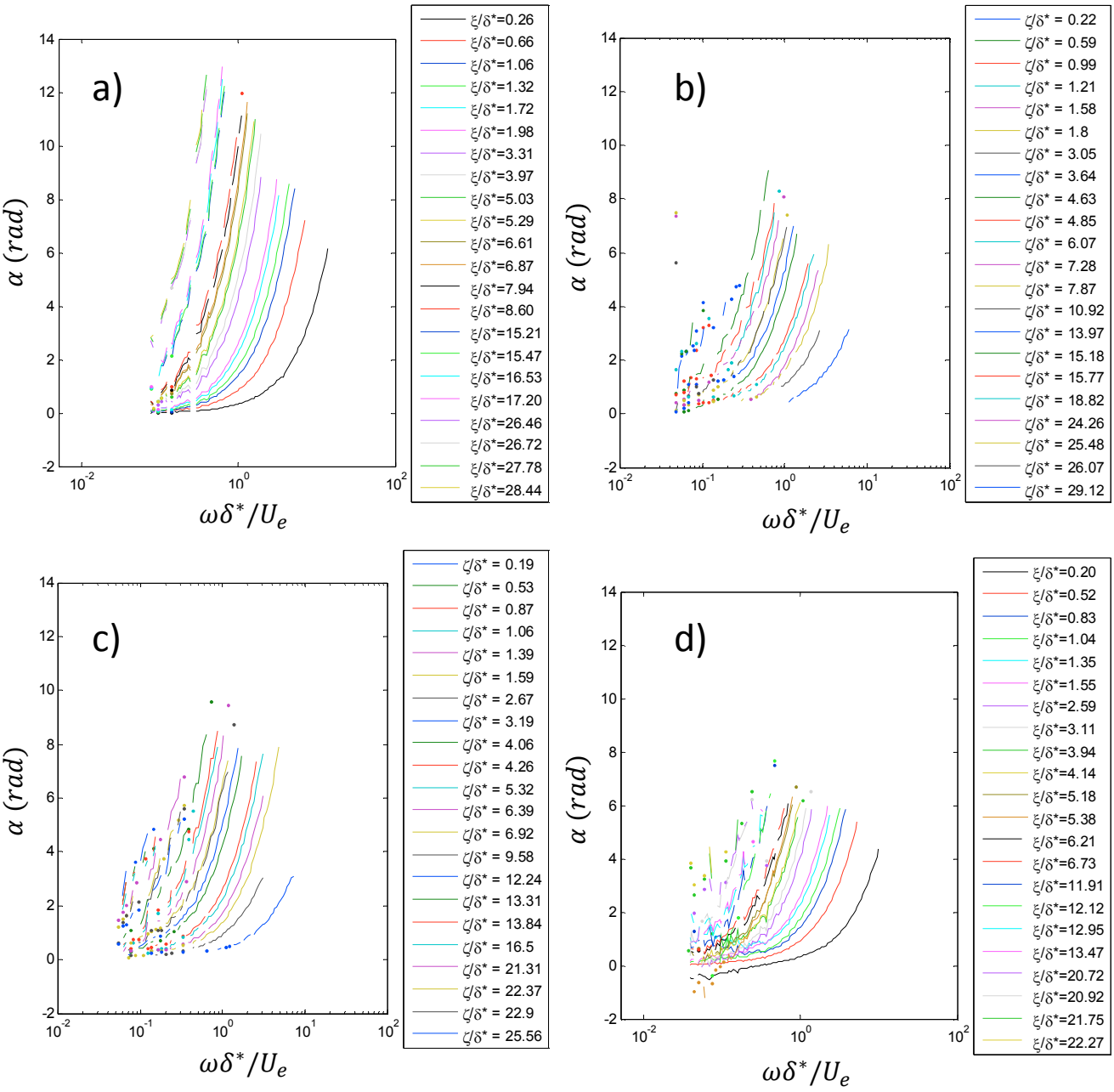

Figure 72: Streamwise phase angle for Forest's (2012) smooth wall (a) at 67.2 m/s, the ordered 1-mm roughness (b), the random 3-mm roughness (c), and Forest's (2012) ordered 3-mm roughness (d) at 60 m/s.

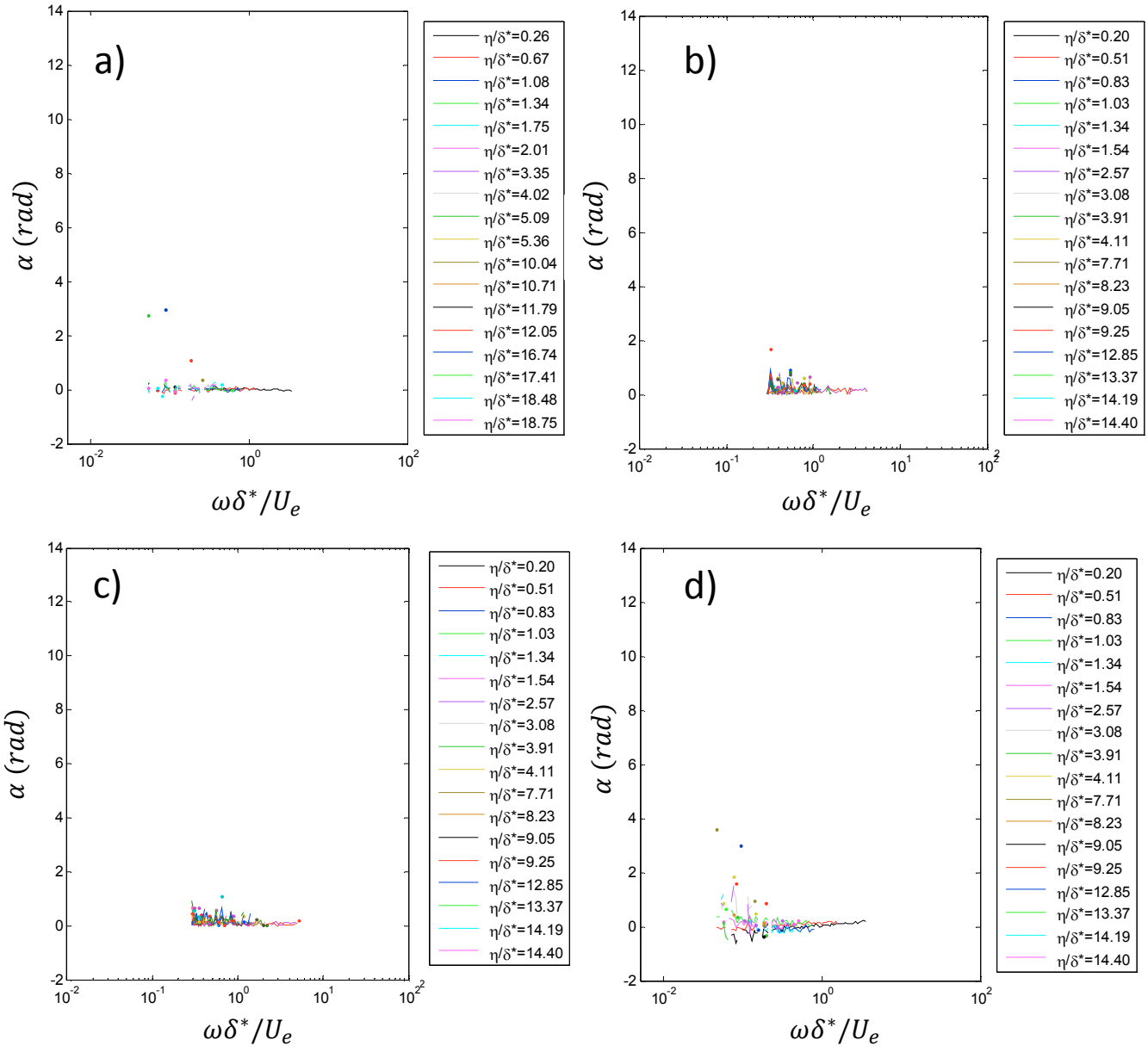

Figure 73: Spanwise phase angle for Forest's (2012) smooth wall (a) at 33.6 m/s, the ordered 1-mm roughness (b), the random 3-mm roughness (c), and Forest's (2012) ordered 3-mm roughness (d) at 30 m/s.

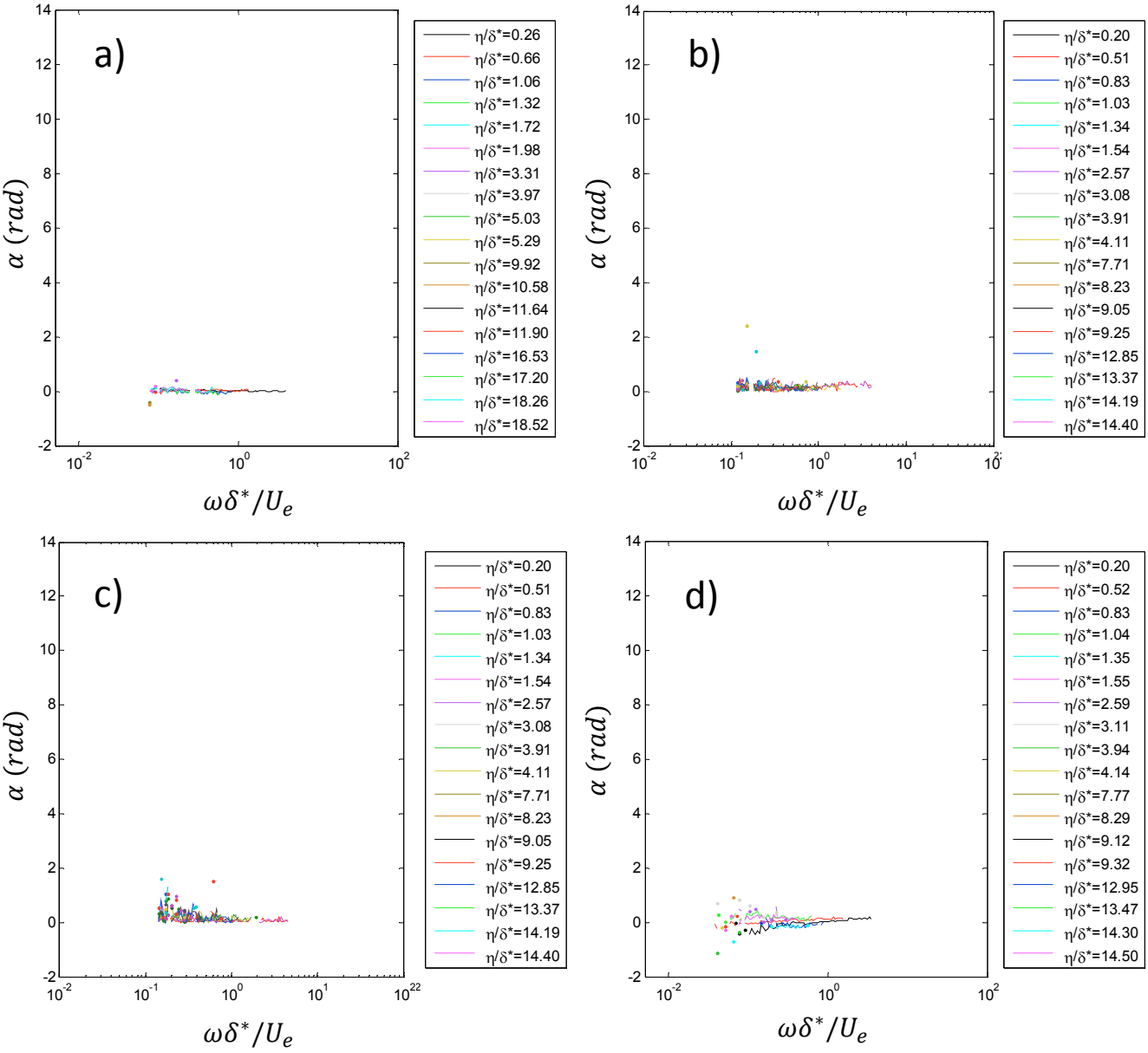

Figure 74: Spanwise phase angle for Forest's (2012) smooth wall (a) at 67.2 m/s, the ordered 1-mm roughness (b), the random 3-mm roughness (c), and Forest's (2012) ordered 3-mm roughness (d) at 60 m/s.

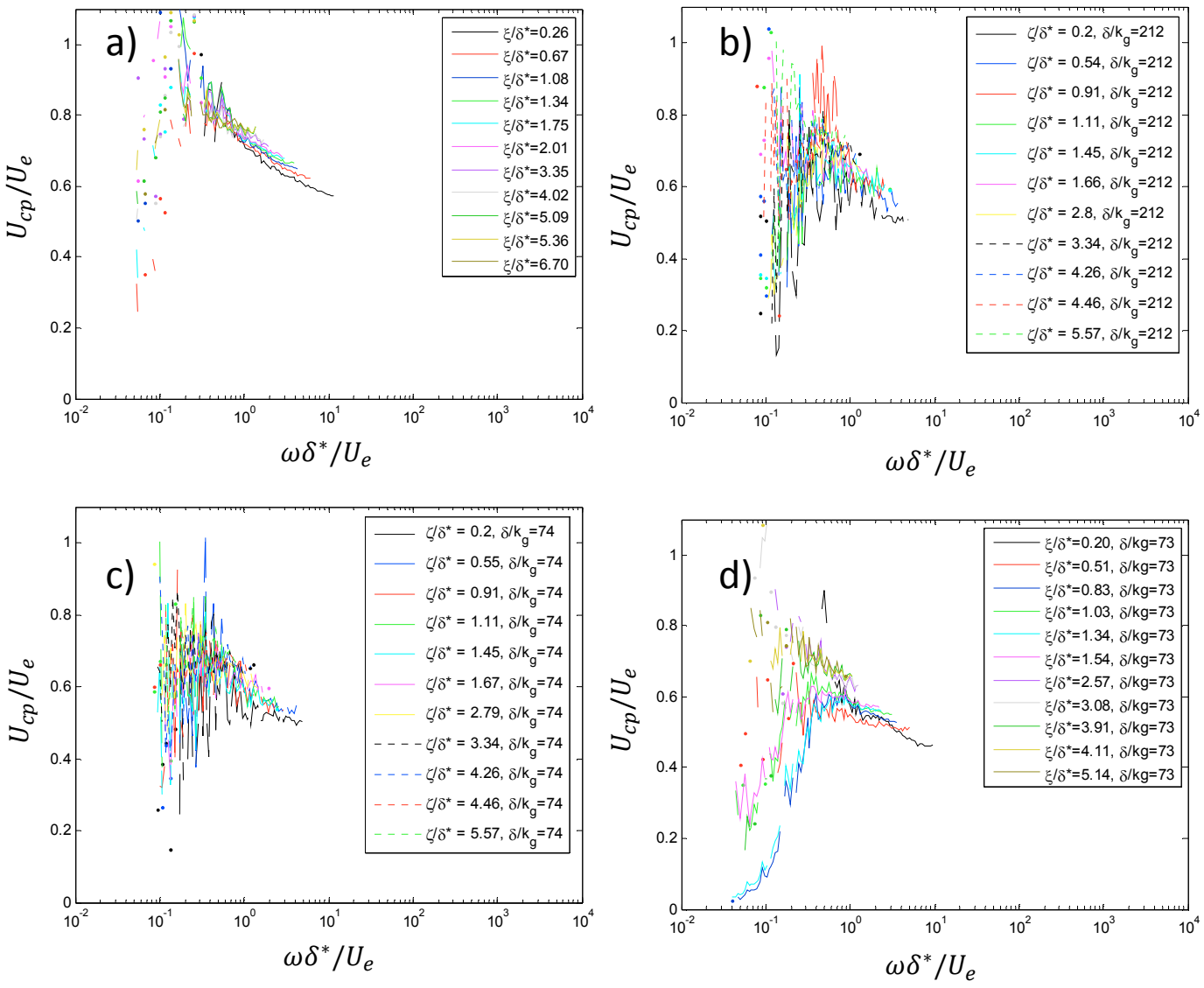

Figure 75: Phase convection velocities for Forest's (2012) smooth wall (a) at 33.6 m/s, the ordered 1-mm roughness (b), the random 3-mm roughness (c), and Forest's (2012) ordered 3-mm roughness (d) at 30 m/s.

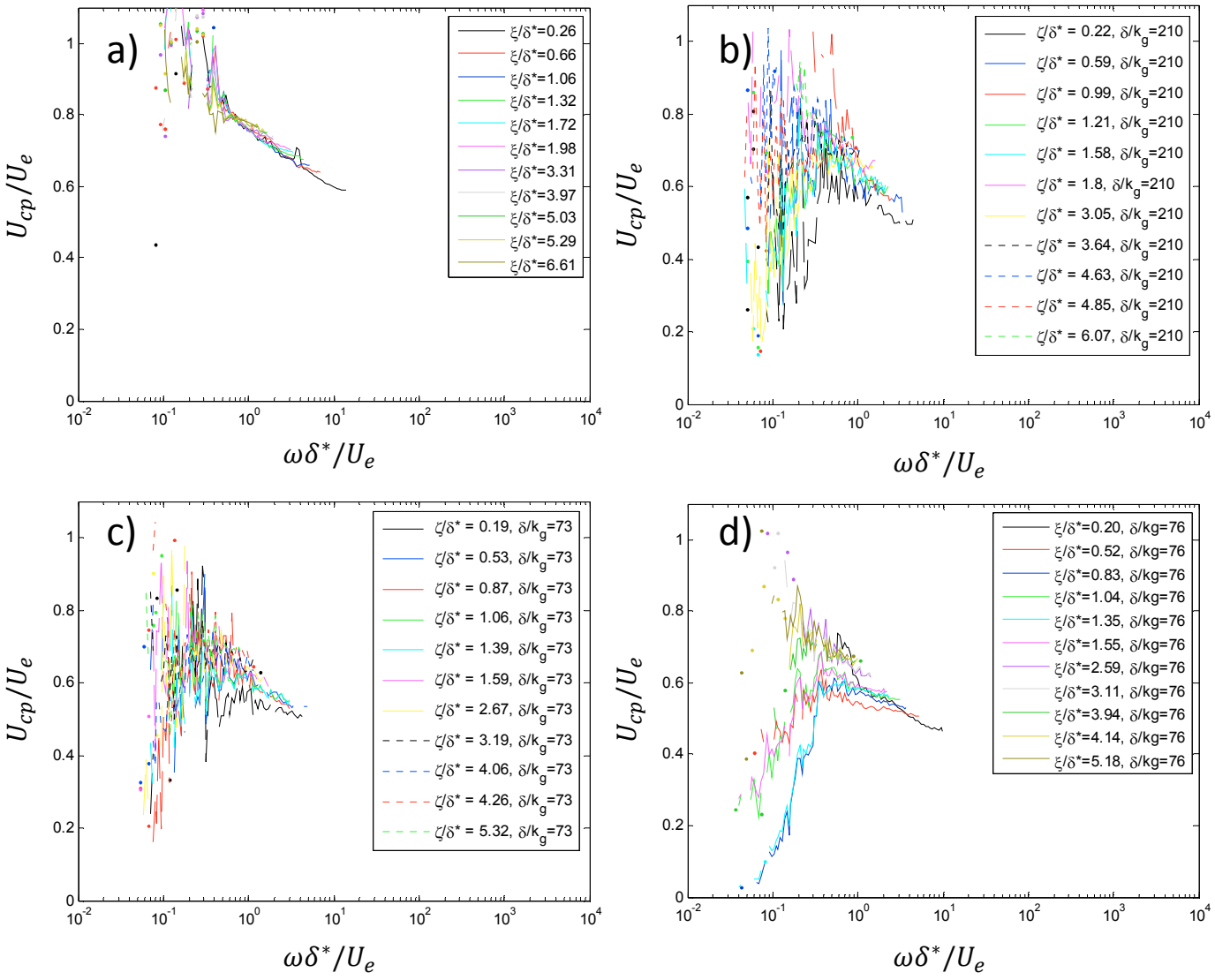

Figure 76: Phase convection velocities for Forest's (2012) smooth wall (a) at 67.2 m/s, the ordered 1-mm roughness (b), the random 3-mm roughness (c), and Forest's (2012) ordered 3-mm roughness (d) at 60 m/s.

Appendix A: Roughness Manufacturing Procedure

Detailed below is a step by step procedure for manufacturing the rough wall fetches. Note that the epoxy gets everywhere, and it will run over the sides of the HDPE mold. Make sure to wear the appropriate clothes and gloves. Also, make sure you have set up a collection system for the excess epoxy, so that it does not run onto the table and floor. I would recommend placing the HDPE mold on a plywood sheet and surrounding the edges with the Fibre Glast Breather and Bleeder to absorb the excess epoxy.

Step 1: Clean the HDPE mold an example of which can be seen in Figure A1. If any roughness elements remain stuck in the mold from a previous fetch, take a flat head screw driver and lightly tap around the edges of the element to loosen it. Once all of the elements have been removed, wipe down the mold with a damp sponge dipped in acetone. Some residual acetone will remain, however, it is very important to make sure that the acetone does not pool on the mold as it will cause damage. Finally use a keyboard type air duster or compressed air to remove any remaining loose particles. Note some larger HDPE molds are manufactured from smaller pieces. If any seems are present in the assembled HDPE mold, rub a wax bar over them to fill in the gap.

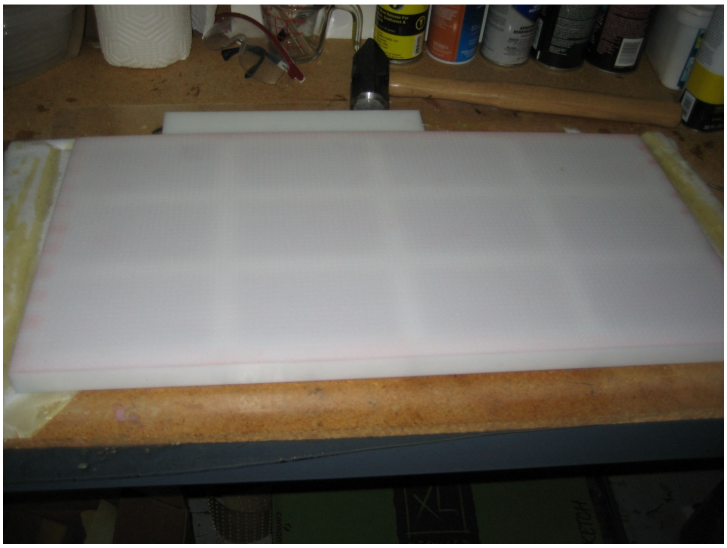

Figure A1: An example of a HDPE mold containing the negative of a 2x1 ft. 1-mm ordered hemispherical roughness fetch, where the elements are spaced 5.5 mm apart.

Step2: Size the fiberglass weave, Canson Sketch paper medium tooth 30% recycled 18x24 in., Fibre Glast Breather and Bleeder, and Fibre Glast Nylon Release Peel Ply to fit the mold. Make sure to leave about 1 to 2 inches of excess on the sides. It is sometimes easier to mark an outline of the material over the mold before it is cut to size as is seen in Figure A2.

Figure A2: Sizing of fiberglass weave (a) and sketch paper (b).

Step 3: In a well-ventilated area, take the Mann Ease Release 200 and spray the entire mold in a moderate back and forth horizontal motion. This process can be seen in Figure A3. Let the mold release settle for 5 minutes. Then apply another coating, but this time spray the entire mold in a moderate back and forth vertical motion. Again let the mold release agent settle for 5 minutes.

Figure A3: Applying the Mann Ease Release 200 to the HDPE mold.

Step 4: Mix a 3:1 ratio of Fibre Glast System 2000 Epoxy Resin to Fibre Glast 2060 Epoxy Hardener in a Tupperware container. Stir the ratio until it becomes a consistent color throughout as seen in Figure A4. There should be enough of the mixture to thinly cover the entire mold with a little extra. You can use a measuring cup or the pump that Fibre Glast sells to measure out this ratio.

Figure A4: 3:1 ratio of epoxy resin to epoxy hardener

Step 5: Pour ¾ of the mixture onto the mold and use a plastic spackling tool or something else wide and flat to evenly spread out the mixture as seen in Figure A5. Be extremely careful not to touch the spackling tool with the surface of HDPE mold. Any contact with the mold other than with the epoxy will remove the release agent, and will make it much more difficult to remove the fetch once the epoxy has dried. Always leave a thin film of epoxy between the spackling tool and the surface of the HDPE mold.

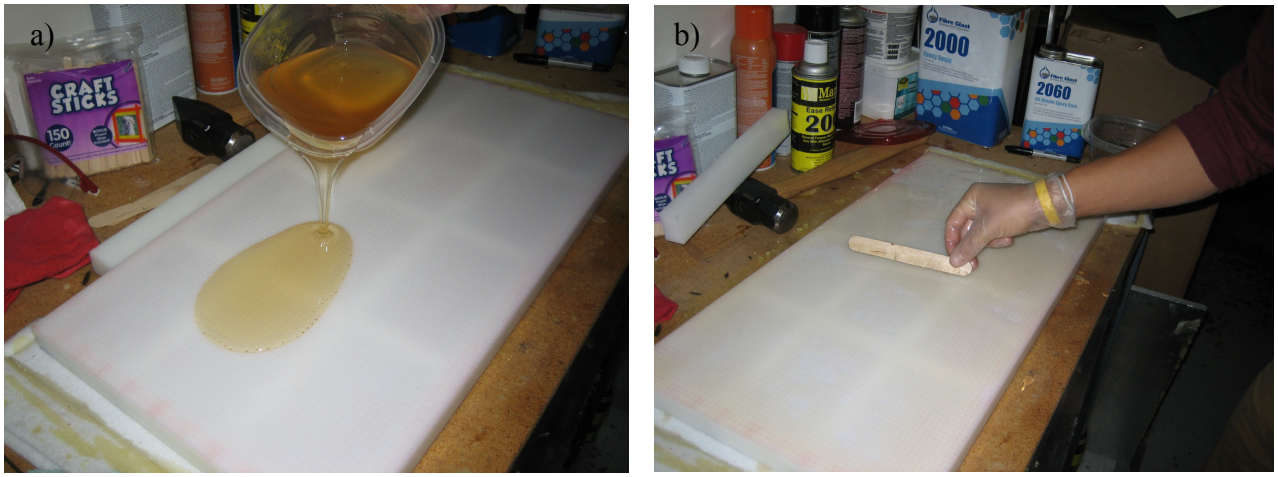

Figure A5: Pouring mixture (a) and spreading it over the mold (b)

Step 6: Lay a piece of the Canson Sketch paper medium tooth 30% recycled 18x24 in. over the mold starting from one edge. Each sheet of paper should lay perfectly adjacent to the other covering the entire mold without overlapping if the size of the mold requires more than one sheet. Take great care not to slide the sheets of paper around to much on the mold as this will disrupt the release agent. Next use the spackling tool or a roller to force out all of the excess epoxy under the paper without ripping it; the more epoxy you can remove between the paper and the surface of the HDPE the better. The sheets of paper may need to be adjusted slightly after this in order to remain adjacent to one another.

Figure A6: Placing the sketch paper over the mold

Step 7: Pour the rest of the epoxy mixture along with any collected excess on top of the paper. Evenly spread out the epoxy, and carefully place the fiberglass weave on top of it as shown in Figure A7. Use the spackling tool or roller to force out all of the excess epoxy. It is not as important as it was in Step 6 to remove all of the excess epoxy though a decent attempt should still be made. The fiberglass weave should be fully saturated with epoxy, and lay completely flat over the mold.

Figure A7: Placing the fiberglass weave over the mold

Step 8: Place the Fibre Glast Nylon Release Peel Ply over the fiberglass as seen in Figure A8. Next place the Fibre Glast Breather and Bleeder (cotton) on top of the nylon. The cotton soaks up any excess epoxy, while the nylon prevents the cotton or anything else from becoming stuck to the back of the fiberglass.

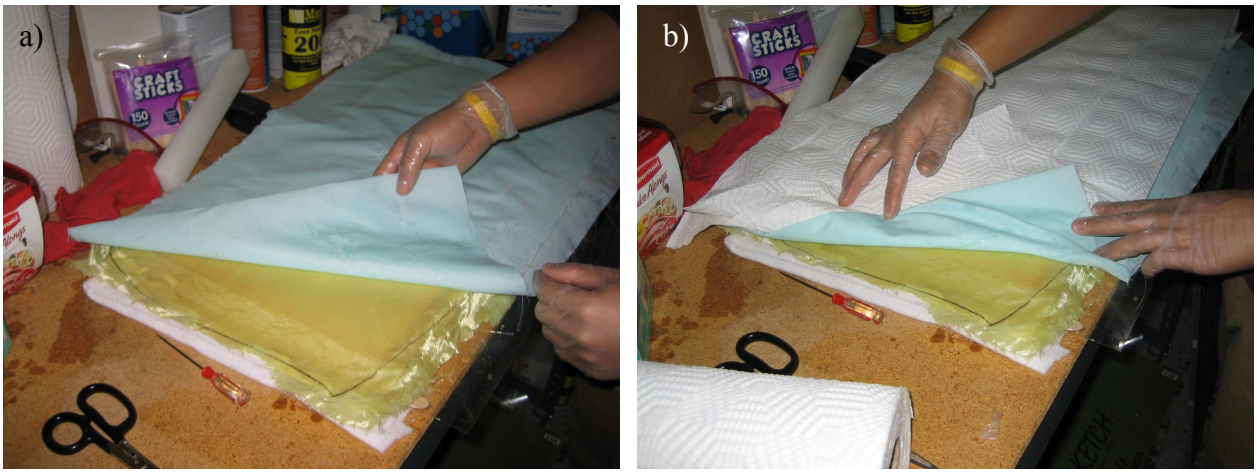

Figure A8: Placing nylon over the fiber glass (a) and cotton (paper towels shown here) (b) over the nylon.

Step 9: Place a plywood sheet or something flat on top of the cotton as seen in Figure A9, and evenly distribute sandbags on top of that. This will provide pressure, ensuring everything remains flat.

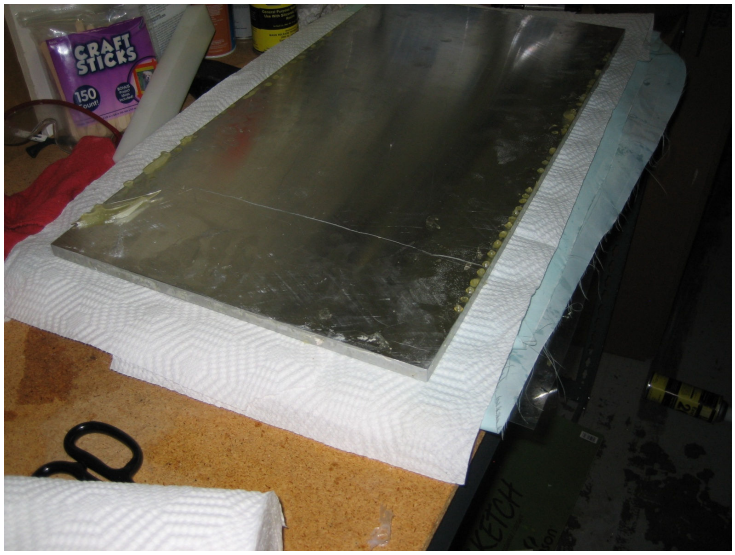

Figure A9: Heavy metal plate placed over the mold layers

Step 10: Let the epoxy cure for 24 hours before removing the fetch from the mold.

Removing Fetch from HDPE Mold

Removing the fetch from the mold takes a lot of patience. Loosen each corner of the fetch from the mold. Try and keep the fetch parallel to the mold when removing it. I found it easiest to place my hands flat, with my palms facing up, and slowly wiggle my fingers as I work my way into the center. Generally one corner will be much easier to remove than the others, so work from this one. Sometimes hitting an area that is stuck gently with a hammer will help loosen it.